REVISTA MILITAR de CIÊNCIA e TECNOLOGIA

Print version: ISSN 0102-3543

Volume XL - 2° Quarter 2023

ENGENHARIA MILITAR

Mobilidade, Contramobilidade e Proteção

REVISTA MILITAR DE CIÊNCIA E TECNOLOGIA
Comandante do Exército:
Gen Ex Tomás Miguel Ribeiro Paiva

Departamento de Ciência e Tecnologia:
Gen Ex Achilles Furlan Neto

Departamento de Educação e Cultura do Exército:
Gen Ex Francisco Carlos Machado Silva

Comandante do Instituto Militar de Engenharia:
Gen Div Juraci Ferreira Galdino

Diretor da BIBLIEx:
Cel Art Marcos Walfrido Ricarte Figueiredo

CORPO REDATORIAL:

Editor-chefe:
Prof. Dr. Fernando Manuel Araújo Moreira

Editor-chefe adjunto:
Prof. Dr. Álvaro José Boareto Mendes

Editores adjuntos:
Prof. Dr. Marcelo de Miranda Reis
Prof. Dr. Paulo Henrique Coelho Maranhão

Editores de área:
Engenharia Civil, Transportes e Ciências Ambientais: Prof. Dr. Filipe Almeida Corrêa do Nascimento • Engenharia Elétrica e áreas afins: Prof. Dr. Antônio Eduardo Carrilho da Cunha • Engenharia Mecânica e áreas afins: Prof. Dr. André Luiz Tenório Rezende • Engenharia Química e áreas afins: Prof. Dr. Julio Zukerman Schpector • Engenharia Cartográfica: Prof. Dr. Vagner Braga Nunes Coelho • Engenharia Nuclear: Profa. Dra. Inaya Correa Barbosa Lima • Ciência e Engenharia de Materiais: Prof. Dr. André Ben-Hur da Silva Figueiredo • Ciência e Engenharia da Computação: Prof. Dr. Paulo Cesar Salgado Vidal • Engenharia de Defesa: Prof. Dr. Giuseppe Miceli Junior • Outras áreas: Prof. Dr. Marcelo de Miranda Reis

Editores associados externos:
• Dr. André Fenili – Universidade Federal do ABC, Santo André, SP • Dr. Fernando Fachini Filho – Instituto Nacional de Pesquisas Espaciais, SP • Dr. José Carlos Costa da Silva Pinto – Universidade Federal do Rio de Janeiro, RJ • Dr. José Carlos Maldonado – Universidade de São Paulo, São Carlos, SP • Drª. Júlia Célia Mercedes Strauch – Escola Nacional de Ciências Estatísticas, RJ • Dr. Luiz Pereira Calôba – Universidade Federal do Rio de Janeiro, RJ • Dr. Otto Corrêa Rotunno Filho – COPPE/Universidade Federal do Rio de Janeiro, RJ • Dr. Richard Magdalena Stephan – COPPE/Universidade Federal do Rio de Janeiro, RJ • Dr. Webe João Mansur – COPPE/Universidade Federal do Rio de Janeiro, RJ • Dr. Carlos Alberto Nunes Consenza – COPPE/Universidade Federal do Rio de Janeiro, RJ

DIREÇÃO, IMPRESSÃO E DISTRIBUIÇÃO:

Diretor:
Cel Art Marcos Walfrido Ricarte Figueiredo

Editor executivo:
Cap R1 Antônio Carlos Manhães de Souza

ADMINISTRAÇÃO, REVISÃO, PROGRAMAÇÃO E DIAGRAMAÇÃO:
Coordenação: INSTITUTO MILITAR DE ENGENHARIA – IME

Redação, Diagramação e OJS:
Rubenildo Pithon de Barros
Marcela Fagundes Casotti
Luiz Tadeu Carqueija Mota

Revisão Tikinet:
Revisores: Cristina Saez; Guilherme Oliveira; Piero Kanaan • Diagramador: Ilário Junior

Impressão e distribuição:
BIBLIEx

Desde 1949
"A Gráfica do Exército" - Compromisso com a Qualidade

Impresso na Gráfica do Exército
Al. Mal. Rondon - Setor de Garagens - QGEx - SMU - CEP:70630-901 - Brasília - DF
Tel: 3415-4367 - Site: http://www.graficadoexercito.eb.mil.br
E-mail: divcmcl@graficadoexercito.eb.mil.br

PUBLICAÇÃO TRIMESTRAL

REVISTA MILITAR de CIÊNCIA e TECNOLOGIA

REVISTA MILITAR DE CIÊNCIA E TECNOLOGIA - Volume XL
2º Trimestre de 2023

INSTITUTO MILITAR DE ENGENHARIA - IME
Praça General Tibúrcio, 80 - Praia Vermelha -
Rio de Janeiro-RJ - CEP 22.290-270 -
Tel.: (21) 2546-7115
Website: https://ebrevistas.eb.mil.br/CT - Email: rmct@ime.eb.br

BIBLIOTECA DO EXÉRCITO
EDITORA (BIBLIEx)
Palácio Duque de Caxias - Praça D. de Caxias, 25
3º andar - Ala Marcílio Dias
Centro - Rio de Janeiro-RJ
CEP 20.221-260
Tel.: (21) 2519-5707

ACESSE NOSSA REVISTA DIGITAL

Nossa capa:
Homenagem ao Quadro de Engenheiros Militares

REVISTA MILITAR de CIÊNCIA e TECNOLOGIA
Versão impressa: ISSN 2316-4522

ENGENHARIA MILITAR
Mobilidade, Contramobilidade e Proteção

Localização estratégica de equipamentos de monitoramento eletrônico para interceptação de fluxo evasivo em malhas rodoviárias - Pág 5
Proposta de modelos de otimização para movimentações do pessoal militar do Exército Brasileiro - Pág 18
A influência do estado de maturação de componentes na sua aprovação em projetos de novos produtos na indústria de automóveis - Pág 26
Avaliação de variáveis agronômicas e imagens do satélite Sentinel-2 para estimativa de produtividade da cana-de-açúcar a partir do algoritmo Random Forest - Pág 35
Caracterização microestrutural de niobatos de sódio pelo processo sol-gel para uso na engenharia tecidual - Pág 42
Escória de aciaria como material precursor na geopolimerização - Pág 49
Influência da adição de carbeto de titânio na densificação e microestrutura de cerâmicas de alumina dopadas com nióbia e fluoreto de lítio - Pág 55
Proposta de metodologia para avaliação temporal de estações de redes de nivelamento empregando a Teoria dos Grafos - Pág 62
Avaliação dos principais modelos de admitância da sonda coaxial aberta para medidas de permissividade elétrica - Pág 70

EDITORIAL

REVISTA MILITAR de
CIÊNCIA e TECNOLOGIA

The twentieth and twenty-first centuries were profoundly shaped by armed conflicts that redefined borders, ideologies, and societies. World War I ushered in a new era of industrialized warfare, with millions killed and the collapse of empires such as the Austro-Hungarian and the Ottoman. Soon after, World War II became the largest conflict in history, involving almost the entire planet, resulting in the Holocaust, use of nuclear weapons and creation of the UN. During the so-called Cold War, conflicts such as the Korean War (1950-1953) and the Vietnam War (1955–1975) reflected the ideological dispute between the US and the USSR. In the Middle East, wars such as the Gulf War (1990–1991) and the ongoing conflicts involving Israel and Palestine have marked the geopolitical scene. In the 21st century, the Afghanistan War (2001–2021) and the Iraq War (2003–2011) were responses to 09/11, with lasting consequences. More recently, Russia's invasion of Ukraine in 2022 has reignited global tensions, reminding us that the echoes of war still resonate strongly in the contemporary world, but with a great differential: the use of new military doctrines and equipment never before imagined, such as drones. In other words, innovation, more than ever, is present in all theaters of operations of current conflicts. In a global scenario increasingly driven by data, accuracy and security, Brazil has been standing out on several fronts of applied research. The intersection of materials science, systems engineering, and artificial intelligence reveals a vibrant academic and technological ecosystem, committed to solutions ranging from the field of defense to oral health. This editorial proposes a reflection on seven studies that illustrate this multifaceted advance strongly based on innovation.

The study on *The Impact of the Weighting of Semantic Resources for the Identification of Suspected Crimes in Social Networks* points to a new era in public security. By employing algorithms capable of interpreting linguistic and contextual nuances, researchers expand the ability to detect suspicious behavior in digital environments. This approach not only reinforces crime prevention, but also raises ethical debates about privacy and surveillance.

The research on *alumina ceramics doped with niobia and silica*, processed with functional gradient technique, represents a leap in materials engineering. The controlled densification and morphology of these ceramics promise applications in extreme environments, such as aerospace shields and components, where thermal and mechanical resistance are crucial.

In the field of defense and navigation, *azimuth estimation from multiple fixed beamformings in antenna-array radar systems* offers significant advances. This technique allows greater accuracy in locating targets, even in scenarios of interference or low visibility, reinforcing national technological sovereignty.

The *review of materials for stand-alone ballistic plates*, according to the Joint Operational Requirements of the Ministry of Defense, shows the continuous effort to align scientific research with strategic demands. The search for resistant and economically viable lightweight materials is essential to ensure effective protection without compromising mobility.

Evaluation of the mechanical properties of AA 5052 and AA 5050C aluminum alloys in laminated sheets demonstrates the potential of these alloys for structural applications. With their combination of lightness and strength, these materials are ideal for industries such as transportation, construction, and defense.

The innovation also appears in the creation of *aramid tissue compounds infused with polyethylene glycol and hematite nanoparticles*. Along with ballistic resistance, these materials also demonstrate microwave absorption properties, indicating potential applications in stealth shielding and protection against electromagnetic radiation.

Finally, the *influence of surface treatment on the primary stability of bone-integrating dental implants*, quantified with strain gauge, shows how precision engineering can transform dentistry. Improved bone integration and durability of implants has a direct impact on patients' quality of life.

In conclusion, these studies, although diverse in scope, converge on a common point: the commitment to scientific excellence and practical applicability. They reflect a country that invests in knowledge to protect, innovate and care. In times of global uncertainty, this is a bet worth gold. It is in this context that the Military Institute of Engineering is located, a bicentennial corporate university whose primary objective is to meet the needs of the Brazilian Army, but without leaving aside dual applications that may contribute as much as possible to civil society. *Revista Militar de Ciência e Tecnologia* (RMCT, publication *Open Access*), which is one of the regular publications of the Brazilian Army, plays a crucial role in the field of military science and technology. Its significance in this area is considered paramount.

We wish you an excellent reading!

Dr. Eng. Fernando M. Araujo-Moreira
Editor-in-Chief of RMCT

SUMMARY

VOL.40 Nº2 2023
https://doi.org/10.22491/rmct.v40i2.9271.en

The Impact of Assigning Weights to Semantic Resources on the Identification of Criminal Suspects on Social Media

Érick S. Florentino[1], erick.florentino@ime.eb.br, Orcid 0000-0002-0828-4058
Ronaldo R. Goldschmidt[1], ronaldo.rgold@ime.eb.br, Orcid 0000-0003-1688-0586
Maria Cláudia Cavalcanti, yoko@ime.eb.br, Orcid 0000-0003-4965-9941
[1]Instituto Militar de Engenharia – IME

ABSTRACT: The identification of criminal suspects on social media has been a topic of great relevance in the analysis of this type of media. Most of the time, the methods that seek to identify these suspects use textual data made available by people on these networks (e.g. messages, comments, among others). To analyze the texts, these methods often use semantic resources such as controlled vocabularies or even simple sets composed of terms, according to the domain in question (e.g. terrorism, pedophilia, among others). The mention of one or more of these terms can raise suspicions about the people who have used them. However, some terms raise more suspicion than others. Therefore, this work seeks to investigate the impact of differentiating the level of dangerousness of the terms used by a method for identifying criminal suspects on social media and whether this can lead to better results in identifying suspects. The results obtained through experiments in the domain of pedophilia showed that differentiating the level of dangerousness of the terms provided better results in 82.5% of the experiments carried out.

KEYWORDS: Suspects. Social Media, Semantic Resources.

RESUMO: A identificação de pessoas suspeitas de crimes em redes sociais tem sido um tema de grande relevância na análise desse tipo de rede. Na maioria das vezes, os métodos que buscam identificar esses suspeitos utilizam dados textuais disponibilizados pelas pessoas nessas redes (e.g. mensagens, comentários, entre outros). Para analisar os textos, tais métodos costumam utilizar recursos semânticos como vocabulários controlados ou até mesmo simples conjuntos compostos por termos, de acordo com o domínio em questão (e.g. terrorismo, pedofilia, entre outros). A menção de um ou mais desses termos pode levantar suspeitas sobre as pessoas que os utilizaram. No entanto, há termos que levantam mais suspeitas do que outros. Assim sendo, este trabalho busca investigar o impacto da diferenciação do nível de periculosidade dos termos utilizados por um método de identificação de suspeitos de crimes em redes sociais e se isso pode levar a melhores resultados na identificação dos suspeitos. Os resultados obtidos por meio de experimentos no domínio da pedofilia mostraram que a diferenciação do nível de periculosidade dos termos proporcionou melhores resultados em 82.5% dos experimentos realizados.

PALAVRAS-CHAVE: Suspeitos. Redes Sociais, Recursos Semânticos.

1. introduction

Social media (e.g., X - formerly Twitter, YouTube, Instagram, Facebook, among others) are part of everyday life for the vast majority of society [1]. Every day, a large amount of data is made available in these networks through various functionalities, such as sharing videos and exchanging messages [2]. In addition, these networks allow for real-time interactions, without geographical space being a limitation [3]. Because of this, *Social Network Analysis*[1] has been of great interest to public and private institutions for a wide variety of purposes [5].

One of the Social Network Analysis tasks that has been of great relevance in recent years is the identification of individuals suspected of crimes on social media (e.g. pedophilia, bullying, terrorism) [6] [7] [8]. This is due to the growing number of people who have used the resources available on networks to carry out acts that can pose risks to other people, both externally and internally to these virtual environments [9] [10]. For example, such acts can have some kind of psychological and/or physical impact on people [4].

---

[1] Term given to any set of activities that seek to extract knowledge about individuals who use social networks [4].

In the literature, a significant part of the methods that seek to identify individuals who commit crimes on social networks are based on analyzing the textual content provided by people [11] [12] [7]. This analysis is often supported by a controlled vocabulary or a set of terms commonly used by suspicious people in the application domain [11] [13]. These vocabularies or sets of terms can contain expressions with different levels of "dangerousness[2]". There are methods that seek to differentiate these levels [14] [15] [16] and others that do not [12] [11] [17]. Given this scenario, the following research questions arise: *What is the impact of differentiating the dangerousness levels of suspicious terms in a vocabulary or set of terms? Can such differentiation lead to better results in identifying individuals suspected of crimes on social networks*?

In order to find evidence to answer the above questions, the study described in this article carried out experiments with the INSPECTION method[3] [14], considering five sets of data, in two ways. In the first, all the terms were assigned the same weight, i.e., without differentiating their level of dangerousness. In the second, the level of dangerousness of each group of terms was differentiated. Based on the experiments conducted, it was possible to observe that weighting the dangerousness levels of the controlled vocabulary terms led to better results in 82.5% of the experiments, thus positively addressing the research questions raised.

The rest of the paper is organized as follows. Section 2 presents some basic concepts related to social network analysis and unstructured data (texts). Section 3 presents some studies that seek to identify crime suspects through the use of controlled vocabularies or sets of terms according to the application domain. The INSPECTION method and its stages are briefly described in Section 4. Details of the experiments conducted and the results obtained are in Section 5. Finally, Section 6 highlights the contributions of this study and possible future research.

2. Basic concepts

In social network analysis, it is essential to gain a deeper understanding of an individual. To do this, three main pieces of information can be extracted from the network [18]: Topological, Temporal and Contextual.

Topological information, based on the structure of the graph that represents the network, makes it possible to identify how the different nodes (individuals or entities) are interconnected [19]. This reveals interaction patterns and the relative importance of each node in the network [20]. In some social networks, however, this topology is not so obvious and it is necessary to use tools to identify the interconnections between individuals. An example of this is Youtube. The TROY algorithm [21] [16] is a tool that reveals the interactions between YouTube users. By analyzing responses to comments, the algorithm identifies who "received" or to whom a given textual content was "sent", thus generating a multigraph of interactions.

On the other hand, temporal information, which involves analyzing data over time, focuses on the chronology of interactions [22]. Understanding when certain actions take place can provide valuable insights into the behavior of individuals and social dynamics [20].

Contextual information considers the social and cultural environment, as well as intentions in communications [14]. Although it is relevant, it often appears as unstructured data such as messages and comments, which are difficult to analyze [23] [24]. Techniques such as Text Mining and Semantic Annotation help transform these data into actionable

---

[2] Dangerousness is a term that refers to the quality of something that poses a risk or danger. In today's context, people and/or words that are suspicious according to a domain can be classified according to their level of danger.

[3] A method aimed at identifying people suspected of crimes on social media through textual content. To do this, it uses a controlled vocabulary made up of terms according to the application domain (e.g. pedophilia, etc.). In this method, these terms are weighted and normalized according to their level of dangerousness in the domain in question. Subsequently, people are weighted according to the use of terms belonging to this vocabulary in their texts.

knowledge, enabling a deeper analysis of social networks and human interactions [25] [14].

Text mining is a powerful technique that allows useful knowledge to be extracted from large volumes of textual data, using a variety of resources and approaches [26]. This extraction is carried out using computational tools and techniques that make it possible to identify patterns, trends and relevant information in texts [27]. Among the various methodologies used in text mining are Machine Learning techniques, which allow for the modeling and prediction of behavior from data; statistical analyses, which help to quantify and interpret information; and the Bag-of-Words model, which represents documents as sets of words, facilitating textual analysis in a simplified manner [28].

Semantic annotation of texts uses resources that go beyond simple textual analysis, incorporating semantic elements that enrich understanding of the content [29]. Among the resources available is the Controlled Vocabulary, also known as a Thesaurus, which is made up of a structured list of terms and expressions that describe a particular domain of knowledge and has the function of organizing and standardizing the terminology used, facilitating the search and retrieval of specific information [30].

In comparison, ontologies offer a richer and more complex approach, as they not only define terms, but also establish hierarchies and relationships between concepts, allowing for a dynamic and interconnected representation of knowledge, which makes it easier to understand the relationships between terms and promotes a more in-depth analysis of the data [31]. Both text mining and semantic annotation are essential in extracting and organizing knowledge from textual information, making a significant contribution to data analysis in various areas.

3. Related work

In this section, we will present some studies that use a controlled vocabulary or set of terms to enable contextual analysis of textual data from the network (e.g. messages, comments, among others), in order to identify different types of people suspected of crimes on social networks (e.g. pedophilia, harassment and cyberbullying).

Bretschneider et al. [12] developed a method that seeks to identify online harassment messages. This method uses a pre-defined set of words that can be classified as highly dangerous in the domain in question to help identify messages with suspicious content. From this set, messages that fit into textual patterns are checked. These patterns assess the connection between a person (e.g. personal pronouns, user names, etc.) and a suspicious (or profane) word belonging to the predefined set. In this way, messages that fit these standards are marked as harassing. On the other hand, Bretschneider and Peters [11] use the same method proposed by Bretschneider et al. [12] to find people who practice cyberbullying. However, Bretschneider and Peters [11] enrich the method with topological analysis by considering people's relational behavior. In this way, people are considered suspicious if they have sent a certain number of messages with suspicious content to the same person.

Elzinga et al. [17] developed a non-automated method that uses a temporal relational semantic system to analyze conversations with pedophilic content in chat rooms over time. To do this, Elzinga et al. [17] created 6 (six) categories into which a message can be classified: Where, When, Intimate Parts, Sexual Handlings, Cams and Pictures, Compliments. In this way, each message is manually analyzed and checked to see which category it falls into. Once this is done, given a person with their messages categorized and by means of the temporal relational semantic system, it is possible to visualize the categories in which a person moves through the network over time, as well as their suspicious behavior.

The studies presented consider a set of words in which all are classified as dangerous and do not differentiate the degree of dangerousness. However, in this set, there are terms that are commonly used by people who do not commit any kind of crime on social networks and there are also terms that are more unusual and may raise more suspicion. In Elzinga et al. [17], for example, which addresses the pedophilia domain, the group of words in the "Intimate Parts" category (e.g. penis, breasts, among others) can be considered more dangerous than the group in the "Where" category (e.g. beach, movie theater, among others).

4. The inspection method and its stages

This section presents a brief summary of the INSPECTION method, originally proposed and illustrated in [14]. This method requires as input a data set $N_{v_n} = [M, U]$, where M is a set of messages sent and/or received by people from a set U, and consists of 5 (five) stages: *Terms Preparation*, *Representation of the Network*, *Controlled Vocabulary Weighting*, Contextual *Analysis and Suspect Identification*. The following subsections summarize these steps.

4.1 Terms preparation

In this stage, text mining techniques are used with the aim of normalizing each term t_j on m_x for each message $m_x \in M$. To this end, this stage consists of 3 (three) sub-stages: *Normalization and Extraction of Textual Content, Stop Words Removal* and *Stemming*. In the *Normalization and Extraction of Textual Content* sub-stage, due to textual informality on social networks, the aim is to remove repeated letters, deal with abbreviations, among other things. The *Stop Words Removal* and *Stemming* sub-steps are responsible, respectively, for removing words $t_j \in m_x$ with little meaning and identifying the radical of terms. At the end, the set of treated messages M' is generated.

4.2 Network representation

In the Representation of the Network stage, two multigraphs are constructed from M' in order to represent the network in two ways. In the first, people and their messages are represented. For this, a directed homogeneous multigraph G_{PP} (V_{PP}, E_{PP}) is used, where each $v_{PP} \in V_{PP}$ represents a person and each $e_{PP} \in E_{PP}$ represents a message, which makes it possible to identify the person who sent and/or received that message. In addition, each e_{PP} has an attribute T, responsible for storing the textual content of a message $m_x \in M$. In the second way of representing the network, by means of a directed heterogeneous multigraph, G_{PT} $(V_P \cup V_T E_{PT} \cup E_{TP})$, the People and Terms used in messages are represented. In this case, vertices V_P and V_T, respectively, represent people and the terms used in messages $(t_j \in m_x)$. The directed edges E_{PT} and E_{TP} are responsible for informing, respectively, the person who sent and the person who received a certain term.

4.3 controlled vocabulary Weighting

This sub-stage uses a controlled vocabulary $O = [C, R]$ according to the domain of the application (e.g. Terrorism, Pedophilia, Bullying, among others). This vocabulary is constituted of a set of terms C and a set of relationships between terms R. The set of terms is divided into two disjoint subsets, i.e., $C = [C_r, C_s]$, where C_r contains more generic terms (called root classes) and C_s contains specific terms (called subclasses). Knowing that each class has a w attribute, responsible for storing the weight of the class, the vocabulary is weighted in two phases. In the first phase, a specialist in the domain in question is used to weight the root classes ($c_r \in C_r$).

Once the root classes have been weighted, the second phase seeks to weight the subclasses ($c_s \in C_s$). These subclasses go through the *Normalization and Extraction of Textual Content* and *Stemming* sub-steps of the *Data Preparation* stage in the same way as described above for the message terms. At the end of this phase, a set of processed subclasses is generated called. With the subclasses processed ($c'_s \in C'_s$), we check which of them are present in the network to be analyzed. To do this, a filter is applied using the following operation $A = C'_s \cap VT$. The global weight is then calculated (), of each $t'_j \in A$ (Eq. 1).

$$GW'_{t_j} = \log 2\left(\frac{|E_{pp}|}{|n'_{t_j}|}\right) \quad (1)$$

In equation 1, $|E_{PP}|$ and $|\mathrm{n}'_{\mathrm{t}_\mathrm{j}}|$ indicate, respectively, the total number of edges (or number of messages) in G_{PP} and the number of edges in E_{PP} that have the term t'_j in messages (i.e., $\mathrm{n}'_{\mathrm{t}_\mathrm{j}} = \{e_{ppi} | \mathrm{t}'_\mathrm{j} \in e_{ppi} .T\}$). In this way, the global weight $\mathrm{GW}_{\mathrm{t}_\mathrm{j}}'$ is responsible for expressing the rarity of each term.

Once the rarity of each term has been identified, it must be normalized according to the root class to which the respective term is linked. In this way, it is possible to differentiate the level of dangerousness of each term. To do this, HGW ($HGW = \log 2\left(\frac{\mathrm{E_{PP}}}{1}\right)$) is calculated, since the normalization is given according to the maximum global weight. Next, the representativeness in percentage terms of the term is checked using $\mathrm{GW}_{\mathrm{t}_\mathrm{j}}'$ (Eq. 2).

$$\mathrm{GW}_{\mathrm{t}'_\mathrm{j}}^{\%} = \frac{\mathrm{GW}_{\mathrm{t}'_\mathrm{j}}^{*1}}{\mathrm{HGW}} \qquad (2)$$

The values of this representativeness are used to calculate the weight of the normalized term. Once these values have been calculated, $\mathrm{GW}_{\mathrm{t}'_\mathrm{j}}^{\mathrm{N}}$ (Eq. 3) is used to obtain the final Global Weight for each term, within the range of its category.

$$\mathrm{GW}_{\mathrm{t}'_\mathrm{j}}^{\mathrm{N}} = \left(\left(\mathrm{Max}\left(\mathrm{C}_{\mathrm{r}_\mathrm{k}}\right) - \mathrm{Min}\left(\mathrm{C}_{\mathrm{r}_\mathrm{k}}\right)\right) \times \mathrm{GW}_{\mathrm{t}'_\mathrm{j}}^{\%}\right) + \mathrm{Min}\left(\mathrm{C}_{\mathrm{r}_\mathrm{k}}\right) \qquad (3)$$

This is done by calculating the interval for each c_r ($Max\ (\mathrm{C}_{\mathrm{r}_\mathrm{j}}) = \mathrm{C}_{\mathrm{r}_\mathrm{j}}.w$ e o $Min\ (\mathrm{C}_{\mathrm{r}_\mathrm{j}}) = Max\ (\{\mathrm{C}_{\mathrm{r}_\mathrm{i}}.w | \mathrm{C}_{\mathrm{r}_\mathrm{i}} \in C_r - \{\mathrm{C}_{\mathrm{r}_\mathrm{j}}\} \wedge \mathrm{C}_{\mathrm{r}_\mathrm{i}}.w < \mathrm{C}_{\mathrm{r}_\mathrm{j}}.w\} \cup \{0\}$. Once we have the value obtained from $\mathrm{GW}_{\mathrm{t}'_\mathrm{j}}^{\mathrm{N}}$ and we know that $\mathrm{t}'_\mathrm{j} = \mathrm{C}'_\mathrm{s}$, this value is assigned to the w attribute of the subclass of the corresponding term (ie., $\mathrm{c}'_\mathrm{s}.w = \mathrm{GW}_{\mathrm{t}'_\mathrm{j}}^{\mathrm{N}}$)

4.4 Contextual analysis

This stage seeks to identify a score for each person in the network, in order to represent their degree of suspicion in the context of the application domain. To do this, all the terms used by each person are retrieved ($C_{v_T} v_P$), where ($C_{v_T} v_P$) = $\{v_\mathrm{T} | \exists(v_\mathrm{P}, v_\mathrm{T}) \in E_{PT}\}$. However, in this retrieval, there may be terms that are not suspicious, i.e., they are not considered important in the domain of the application. To do this, a filter $C^{\cap}_{v_T}(v_P)$ is applied, where $(C^{\cap}_{v_T} v_P) = C_{v_T} \cap (v_P)\ \mathrm{C}'_\mathrm{s}$, in order to obtain only the suspicious terms used by the person v_P.

For each personwho has used suspicious terms (i.e. $|(C^{\cap}_{v_T} vP)| > 0$), the metrics M_{GW} and M_{FGW} are used. The metric M_{GW}, using Equation 4, is the sum of all the normalized global weights of the suspicious terms used by a person. Thus, this metric presents the sum of the rarity of each suspect term, normalized by the weight of a root class to which that term is linked.

$$\mathrm{M}_{\mathrm{GW}}\left(\upsilon_\mathrm{P}\right) = \sum_{\mathrm{C}_{\mathrm{s}_\mathrm{i}} \in \mathrm{C}^{\cap}_{\upsilon_\mathrm{T}}\left(\upsilon_\mathrm{P}\right)} \mathrm{C}_{\mathrm{s}_\mathrm{i}}.\mathrm{W} \qquad (4)$$

In the metric M_{GW}, the frequency of each suspect term used by a person is taken into account. This frequency is then multiplied by its respective normalized global weight, indicating the importance of this term for a person in relation to all the messages analyzed. The values obtained are then added together. To do this, Equation 5 is used.

$$\mathrm{M}_{\mathrm{FGW}}\left(\upsilon_\mathrm{P}\right) = \sum_{\mathrm{C}_{\mathrm{s}_\mathrm{i}} \in \mathrm{C}^{\cap}_{\upsilon_\mathrm{T}}\left(\upsilon_\mathrm{P}\right)} \mathrm{W}\left(\upsilon_\mathrm{P}, \mathrm{C}_{\mathrm{s}_\mathrm{i}}\right) \times \mathrm{C}_{\mathrm{s}_\mathrm{i}}.\mathrm{w} \qquad (5)$$

In this way, $W(v_P, \mathrm{C}_{\mathrm{s}_\mathrm{i}})$ retrieves the frequency of use of a given suspect term by a person. Formally, $W(v_P, \mathrm{C}_{\mathrm{s}_\mathrm{i}}) = |\{(o,t) \in E_{PT}/o = v_P$ e $t = \mathrm{C}_{\mathrm{s}_\mathrm{i}}\}|$. Once one of the metrics has been selected, the score obtained with it is applied to the person analyzed ($v_P.st = M_{GW}(v_P)$ ou $v_P.\mathrm{st} = M_{FGW}(v_P)$), expressing their suspicious behavior numerically.

4.5 Suspect Identification

At this last stage, the scores obtained with each of the above metrics are listed in a descending order, so that the most suspicious people are at the top of the list.

5. Experiments and results

This section presents the set of data used and reports on the experiments carried out with the aim of answering the research questions presented in Section 1. The topic of pedophilia was chosen because social networks have become a major attraction for children and teenagers, making this audience participate assiduously in these environments [32]. For this reason, it is common for pedophiles to use social media to identify potential victims [4].

The prototype of the INSPECTION method [14] was developed in Python 3.0. In the terms preparation stage, the NLTK [33] and Spacy [34] libraries, among others, were used. In addition, a dictionary of slang and abbreviations commonly used on social networks in Portuguese was created to deal with possible noise in the text. This dictionary was built by searching related websites [35] [36] [37]. The following sections present the details of the experiments.

In the next subsections, details of the data sets (subsection 5.1) and controlled vocabularies (subsection 5.2) used in the experiments will be presented.

5.1 Data sets

In the experiments carried out here, five data sets were applied to the INSPECTION method. These sets were constructed from comments and responses in Portuguese extracted from five YouTube videos, from a channel belonging to an underage singer. The videos and channel were chosen because they were more likely to contain suspicious textual content on the topic chosen for the experiments. Table 1 shows the statistical data for the five (5) videos.

Table 1 - Statistical data for each video vn used in the experiments.

Video	Duration	Views	Comments and Responses
v_1	2M:38S	2.551.258	6.897
v_2	3M:14S	57.083	348
v_3	2M:53S	13.041.367	13.080
v_4	2M:56S	18.157.216	18.548
v_5	4M:04S	89.593.403	71.387

As mentioned in Section 4, INSPECTION requires as input a data set $N_{v_n} = [M, U]$. Thus, each of the videos listed in Table 1 was submitted to the TROY algorithm, allowing the extraction of interactions between people; details of this algorithm can be seen in [21] and [16]. The resulting data was used in the experiments presented in this paper and is summarized in Table 2. The process of building these sets also included a data enrichment stage responsible for incorporating information on suspected pedophiles from the PAN-2012-BR dataset [39] [7]. PAN-2012-BR is a dataset containing the conversations of 39 (thirty-nine) pedophiles, which were made available by the São Paulo Federal Public Prosecutor's Office (MPF-SP). These suspects were integrated into the datasets in Table 2 using the link prediction task, as described in detail in [16].

Table 2 - Statistical data from the datasets generated from the videos in Table 1.

Video	N_{v_n}		Mean of Interactions	|U| Suspects	|M| Suspects
	|U|	|M|			
v_1	1.806	10.647	3	39	1.752
v_2	87	382	2	20	132
v_3	3.688	16.332	3	39	1.484
v_4	5.255	18.488	3	39	1.694
v_5	18.802	75.249	3	39	1.280

5.2 Controlled vocabulary

The controlled vocabulary was built based on six categories of words, inspired by [17]: “where”, “when”, “intimate parts”, “sexual handlings”, “cams and pictures” and “compliments”. Each category became a root class from which subclasses extracted from vocabularies found in the literature were added (see Table 3). These classes and their subclasses now form a single vocabulary called *O*. In addition to these root classes, the root class clothing was also considered. Thus, for the experiments with the INSPECTION method, 4 (four) variations of this vocabulary were adopted, as in [16]: O_1^{INT} (without the clothing root class and weighted with integers), O_2^{INT} (with the clothing root class and weighted with integers), O_1^{REAL} (without the clothing root class and weighted with real numbers) and O_2^{REAL} (with the clothing root class and weighted with real numbers).

It is important to note that in the vocabularies O_2^{INT} and O_2^{REAL}, the root class “clothing” is taken into account, as it is common for people suspected of pedophilia to ask about the clothing of their potential victims. This also allows to evaluate the performance of the method with the controlled vocabulary enriched by this class, both with and without weighting. It also makes it possible to compare the weighted method more rigorously (*INT*) and more flexibly (*FLOAT*) in relation to the unweighted vocabulary.

Table 3 shows the weightings of the most generic vocabulary classes. It is worth noting that, for the weighting of the controlled vocabulary, there was the support of a federal police officer from Aracaju/SE who has been working on the subject of pedophilia for 11 (eleven) years.

Table 3 - Weightings of the controlled vocabularies and origins of the subclasses.

c_r	O_1^{INT}	O_2^{INT}	O_1^{REAL}	O_2^{REAL}	C_s
	Weight (w)	Weight (w)	Weight (w)	Weight (w)	
When	1	1	1.5	1.5	[40]
Where	2	2	2.3	2.3	[41]
Compliments	3	3	4.0	4.0	[42]
Cams and Pictures	4	5	6.0	6.0	[43]
Intimate parts	5	6	5.7	5.7	[44]
Sexual Handlings	6	7	5.5	5.5	[45]
Clothing	-	4	-	5.0	[46]

For the INSPECTION experiments without weighting the controlled vocabulary, all the terms were given a weight of 1 (one) (ie, $C_s'.w = 1$). As a result, there was no differentiation in the level of dangerousness of the terms. In this way, a benchmark was created to allow comparison with the results generated with INSPECTION, based on differentiating the level of dangerousness of the terms according to the weighting of the controlled vocabulary.

5.3 Results

Considering the variations in data sets, vocabularies and their weightings, as well as contextual metrics, the INSPECTION method was run 60 (sixty) times in total. The results of these runs are summarized in Table 4. To assess the performance of the INSPECTION method, the measure used was AUC (Area under the Curve) [47]. This measure calculates the probability of a suspect having a higher score than a non-suspect, both chosen n times at random. In this study, n is equal to 100. It is worth noting that the INSPECTION method uses the label of people (suspect and non-suspect) only to evaluate the performance of the method.

In a general analysis of the INSPECTION method [14] with and without vocabulary weighting, it can be seen that all runs of the method led to results higher than the random predictor (AUC >0.5), which indicates that the method has a good ability to identify suspected pedophiles, regardless of whether or not weighting is used.

Table 4 - Results of the experiments.

Video	VC	INSPECTION WITH WEIGHTING		INSPECTION W/O WEIGHTING	
		M_{FGW}	M_{GW}	M_{FGW}	M_{GW}
v_1	O_1^{INT}	0.905	0.905	0.900	0.865
	O_2^{INT}	0.885	0.890		
	O_1^{REAL}	0.910	0.890	0.910	0.835
	O_2^{REAL}	0.915	0.865		
v_2	O_1^{INT}	0.795	0.845	0.600	0.545
	O_2^{INT}	0.810	0.920		
	O_1^{REAL}	0.835	0.835	0.535	0.525
	O_2^{REAL}	0.840	0.920		
v_3	O_1^{INT}	0.930	0.905	0.900	0.895
	O_2^{INT}	0.930	0.890		
	O_1^{REAL}	0.900	0.915	0.855	0.840
	O_2^{REAL}	0.930	0.925		
v_4	O_1^{INT}	0.940	0.930	0.910	0.885
	O_2^{INT}	0.950	0.965		
	O_1^{REAL}	0.945	0.950	0.945	0.915
	O_2^{REAL}	0.930	0.950		

Video	VC	INSPECTION WITH WEIGHTING		INSPECTION W/O WEIGHTING	
		M_{FGW}	M_{GW}	M_{FGW}	M_{GW}
v_5	O_1^{INT}	0.940	0.885	0.905	0.885
	O_2^{INT}	0.925	0.950		
	O_1^{REAL}	0.930	0.925	0.925	0.900
	O_2^{REAL}	0.920	0.915		

In a more detailed analysis, of the 40 (forty) performance comparisons between the INSPECTION method with and without vocabulary weighting, the weighted method won in 33 (thirty-three cases) (82.5%), tied in 3 (three) (7.5%, highlighted in bold and blue in Table 4) and lost in 4 (four) (10%, highlighted in red and italics in Table 4). These results suggest a positive response to the research question of this article, which investigates whether vocabulary weighting (relative to the level of dangerousness of the terms) can help improve the identification of suspected criminals on social networks, specifically in the context of pedophilia.

Further detailing the results of the INSPECTION method with vocabulary weighting, it can be seen that the best performances were achieved with the O_1^{INT} vocabulary, which was successful in all five (5) datasets, only tying in the dataset with the M_{GW} metric. This shows that enriching the vocabulary with new root classes must be done carefully. Furthermore, weighting the root classes more rigidly provided better results. As for the metrics, yielded better results (eighteen out of twenty comparisons - 90%). Therefore, the frequency with which a person used suspicious terms is not so relevant.

In short, from the results presented, it can be seen that weighting the controlled vocabulary gives better results when it comes to identifying people suspected of pedophile crimes. In other words, the impact of weighting the terms proved to be positive in the process.

6. Final considerations

Social media have been increasingly present in society's daily life, attracting the most different audiences with the most different particularities. In this way, they have become a favorable medium for people with bad intentions to commit illegal acts on the web. Therefore, in order to avoid risks to the physical and psychological integrity of individuals on social media, the identification of suspicious individuals has been a major focus.

In the literature, many methods that seek to identify people suspected of crimes on social media use a vocabulary or set of terms according to the application domain. In this way, it becomes possible to analyze the textual data provided by a person on social networks in order to check how suspicious they might be. However, within an application domain, there may be terms with different levels of dangerousness. In view of this, the following research questions were raised in this study: *What is the impact of differentiating the dangerousness levels of suspicious terms in a vocabulary or set of terms? Whether such differentiation can lead to better results in identifying people suspected of crimes on social media.*

In order to answer the above questions, experiments were conducted with the INSPECTION method on 5 (five) sets of data, without and with the weighting of the controlled vocabulary. The results obtained through the experiments in the pedophilia domain showed that the impact of weighting the controlled vocabulary is positive and consequently leads to better results (82.5% of the experiments carried out in this work). In this way, differentiating the levels of dangerousness of terms in semantic resources (e.g. controlled vocabularies, sets of terms, among others) for identifying people suspected of crimes on social networks is highly relevant.

Future work should include: weighting the controlled vocabulary without relying on the help of a specialist in the application domain and conducting experiments on other social networks and domains.

References

[1] SILVA, C. R. M.; TESSAROLO, F M. 2016. Influenciadores digitais e as redes sociais enquanto plataformas de mídia. *In*: Congresso Brasileiro de Ciências da Comunicação, 39., 2016, São Paulo. *Anais* […]. São Paulo: Intercom, 2016.

[2] BENEVENUTO, F.; ALMEIDA, J. M.; SILVA, A. S. *Explorando redes sociais online*: da coleta e análise de grandes bases de dados às aplicações. Porto Alegre: Sociedade Brasileira de Computação, 2011.

[3] TAKHTEYEV, Y.; GRUZD, A., WELLMAN, B. Geography of Twitter networks. *Social networks*, Amsterdam, n. 34, v. 1, 73-81, 2012.

[4] DAS, B.; SAHOO, J. S. Social networking sites – a critical analysis of its impact on personal and social life. *International Journal of Business and Social Science*, United States of America, v. 2, n. 14, p. 222-228, 2011.

[5] LÉVY, P.; FEROLDI, D. *Cybercultura*: gli usi sociali delle nuove tecnologie. ITÁLIA: Feltrinelli, 1999.

[6] Andressa Olivetti Costa. 2019. *Ciberterrorismo*. 2019. Trabalho de conclusão de curso (Bacharelado em Direito) – Centro Universitário Antônio Eufrásio de Toledo de Presidente Prudente, Presidente Prudente, 2019.

[7] SANTOS, L. F.; GUEDES, G. Identificação de predadores sexuais brasileiros em conversas textuais na internet por meio de aprendizagem de máquina. *iSys-Brazilian Journal of Information Systems*, Rio de Janeiro, v. 13, n. 4, p. 22-47, 2020.

[8] LEI, Y.; HUANG, B. Prediction of Criminal Suspect Characteristics with Application of Wavelet Neural Networks. *Applied Mathematics and Nonlinear Sciences*, Boston, 2023.

[9] MANN, B. L. Social networking websites–a concatenation of impersonation, denigration, sexual aggressive solicitation, cyber-bullying or happy slapping videos. *International Journal of Law and Information Technology*, Oxford, v. 17, v. 3, p. 252-267, 2009.

[10] SINGH, M.; SINGH, A. How Safe You Are on Social Networks? *Cybernetics and Systems*, Oxford, v. 54, n. 7, p. 1154-1171, 2023.

[11] BRETSCHNEIDER, U.; PETERS, R. Detecting cyberbullying in online communities. *In*: European Conference on Information Systems, 24., Istanbul, 2016. *Anais* […]. Istanbul, 2014.

[12] BRETSCHNEIDER, U.; WÖHNER, T.; PETERS, R. Detecting Online Harassment in Social Networks. *In*: International Conference on Information Systems, 35., Auckland, 2014. *Anais* […]. Auckland, 2014.

[13] FLORENTINO, E. S.; GOLDSCHMIDT, R. R.; CAVALCANTI, M. C. R. Exploring Interactions in YouTube to Support the Identification of Crime Suspects. *In*: Anais do Simpósio Brasileiro de Sistemas de Informação, 17., Uberlândia, 2021. *Anais* […[. Uberlândia: SBC, 2021.

[14] FLORENTINO, E. S.; GOLDSCHMIDT, R. R; CAVALCANTI, M. C. R. Identifying Suspects on Social Networks: An Approach based on Non-structured and Nonlabeled Data. *In*: Proceedings of the International Conference on Enterprise Information Systems, 23., 2021, Setúbal. *Anais* […]. Setúbal: ICEIS, 2021. Disponível em: https://www.scitepress.org/Link.aspx?doi=10.5220/0010440300510062. Acesso em: 22 abr. 2025.

[15] FLORENTINO, E. S.; GOLDSCHMIDT, R. R.; CAAVALCANTI, M. C. Identifying Criminal Suspects on Social Networks: A Vocabulary-Based Method. In: Proceedings of the Brazilian Symposium on Multimedia and the Web, 20., 2020, São Luís. *Anais* […]. São Luís: SIGWEB, 2020.

[16] FLORENTINO, E. S.; GOLDSCHMIDT, R. R.; CAVALCANTI, M. C. Identificando Suspeitos de Crimes por meio de Interações Implícitas no YouTube. *iSys - Revista Brasileira de Sistemas de Informação*, Rio de Janeiro, v. 15, n. 1, p. :36, 2022.

[17] ELZINGA, P.; WOLFF, K. E.; POELMANS, J. Analyzing chat conversations of pedophiles with temporal relational semantic systems. *European Intelligence and Security Informatics Conference*, [*s. l.*], 2012, p. 242-249.

[18] MUNIZ, C. P. M. T. *Investigando a utilização de atributos temporais no problema de predição de links*. 2016. Dissertação (Mestrado em Ciências em Sistemas e Computação) – Instituto Militar de Engenharia, Rio de Janeiro, 2016.

[19] CHEN, Y.; COSKUNUZER, B.; GEL, Y. Topological relational learning on graphs. *Advances in neural information processing systems*, Cambridge, v. 34, p. 27029-27042, 2021.

[20] MUNIZ, C. P.; GOLDSCHMIDT, R.; CHOREN, R. Combining contextual, temporal and topological information for unsupervised link prediction in social networks. *Knowledge-Based Systems*, Amsterdam, v. 156, p. 129-137, 2018.

[21] FLORENTINO, E.S.; GOLDSCHMIDT, R. R.; CAVALCANTI, M. C. R. Exploring Interactions in YouTube to Support the Identification of Crime Suspects. *In*: Anais do Simpósio Brasileiro de Sistemas de Informação, 17., Uberlândia, 2021. Anais […[. Uberlândia: SBC, 2021.

[22] FLORENTINO, E. S.; CAVALCANTE, A. A. B.; GOLDSCHMIDT, R. R. An edge creation history retrieval based method to predict links in social networks. *Knowledge-Based Systems*, Amsterdam, v. 205, p. 106268, 2020.

[23] BAARS, H.; KEMPER, H-G. Management support with structured and unstructured data—an integrated business intelligence framework. *Information Systems Management*, Abingdon, v. 25, n. 2, p. 132-148, 2008.

[24] BERRY, M. W. *Automatic discovery of similar words*. *Survey of Text Mining*: Clustering, Classification and Retrieval. New York: Springer Verlag, 2004.

[25] CARVALHO, R. C. *Aplicação de técnicas de mineração de texto na recuperação de informação clínica em prontuário eletrônico do paciente*. 2017. Dissertação (Mestrado em Ciência da Informação) – Universidade Estadual Paulista, Marília, 2017.

[26] SULOVA, S. Text mining approach for identifying research trends. *In*: International Conference on Computer Systems and Technologies, 21., 2021, Ruse. Anais […]. Ruse: University of Ruse, 2021.

[27] MORAIS, E. A. M.; AMBRÓSIO, A. P. L. *Mineração de textos*. Relatório Técnico–Instituto de Informática. Goiás: Instituto de Informática Universidade Federal de Goiás, 2007.

[28] TAN, A-H. et al. 1999. Text mining: The state of the art and the challenges. *Proceedings of the PAKDD*, 1999.

[29] OLIVEIRA, H. C.; CARVALHO, C. L. *Gestão e representação do conhecimento*. Goiás: UFG, 2008.

[30] SALES, R.; CAFÉ, L. Diferenças entre tesauros e ontologias. *Perspectivas em Ciência da Informação*, Belo Horizonte, v. 14, n. 1, p. 99-116, 2009.

[31] CHANDRASEKARAN, B.; JOSEPHSON, J. R.; BENJAMINS, V. R. What are ontologies, and why do we need them? *IEEE Intelligent Systems and their applications*, Piscataway, v. 14, n. 1, p. 20-26, 1999.

[32] FERNÁNDEZ, A. Clinical Report: The impact of social media on children, adolescents and families. *Archivos de Pediatría del Uruguay*, v. 82, n. 1, p. 31-32, 2011.

[33] BIRD, S.; KLEIN, E.; LOPER, E. Natural language processing with Python: analyzing text with the natural language toolkit. Sebastopol, na Califórnia. Sebastopol: O'Reilly Media, 2009.

[34] HONNIBAL, M. *et al. spaCy*: Industrial-strength Natural Language Processing in Python. Disponível em: https://zenodo.org/records/10009823. Acesso em: 22 abr. 2025.

[35] Por Da Redação. 2014. SQN, LOL? Entenda as principais expressões e hashtags das redes sociais. *Aconteceu no Vale*. [s. l.], 15 fev. 2014. Disponível em: https://aconteceunovale.com.br/portal/?p=21357#google_vignette. Acesso em: 19 maio 2025.

[36] thecoolcapybara List of internet slangs - gírias da internet. *Reddit*. 20 maio 2020. Disponível em: https://www.reddit.com/r/Portuguese/comments/gn8s1y/list_of_internet_slangs_g%C3%ADrias_da_internet/. Acesso em: 22 abr. 2025.

[37] VEJA lista de abreviações usadas pelos jovens em troca de mensagens na internet. *Gshow*. [*s. l.*], 30 jun. 2021. Disponível em: https://gshow.globo.com/programas/mais-voce/noticia/veja-lista-de-abreviacoes-usadas-pelos-jovens-em-troca-de-mensagens-na-internet.ghtml. Acesso em: 22 abr. 2025.

[38] Ligga Telecom. Gírias nos games e seus significados: quais as mais usadas. https://liggavc.com.br/blog/entretenimento/glossario-conheca-as-girias-mais-usadas-na-internet-e-nos-games/.

[39] ANDRIJAUSKAS, A.; SHIMABUKURO A; MAIA R. F. 2017. DESENVOLVIMENTO DE BASE DE DADOS EM LÍNGUA PORTUGUESA SOBRE CRIMES SEXUAIS. *In*: Simpósio de Iniciação Científica, Didática e Ações Sociais da FEI, 7., 2017. Anais […]. [s. l.], 2017.

[40] Scheider, Simon, and Peter Kiefer. "(Re-) localization of location-based games." *Geogames and geoplay: game-based approaches to the analysis of geo-information*. Cham: Springer International Publishing, 2017. 131-159. SCHEI-

DER, S.; KIEFER, P. (Re-) Localization of Location-Based Games. In: AHLQVIST, O.; SCHILIEDER, C. (Eds.). Geogames and Geoplay: Game-based Approaches to the Analysis of Geo-Information. Berlim: Springer. p. 131-159.

[41] Jerry R Hobbs and Feng Pan. Time ontology in OWL. *W3C working draft*, Arlington, 2006.

[42] NEVES, F. Elogios de A a Z. *Dicio Dicionário Online de Português*. [s. l.], [201-?]. Disponível em: https://www.dicio.com.br/elogios-de-a-a-z/. Acesso em: 22 abr. 2025.

[43] MUKHERJEE, S.; JOSHI, S. Sentiment aggregation using ConceptNet ontology. In: MITKOV, R.; PARK, J. C. (Eds.). *Proceedings of the Sixth International Joint Conference on Natural Language Processing*. Nagoya: Nagoya Editora. p. 570-578.

[44] ROSSE C.; MEJINO, J. L. V. The foundational model of anatomy ontology. In: BURGER, A.; DAVIDSON, D.; BALDOCK, R. *Anatomy Ontologies for Bioinformatics*. Heidelberg: Heidelberg Springer. p. 59-117.

[45] KRONK C.; TRAN, G. Q.; WU, D. T. Y. Creating a Queer Ontology: The Gender, Sex, and Sexual Orientation (GSSO) Ontology. *Studies in health technology and informatics*, Amsterdam, v. 264, p. 208-212, 2019.

[46] KUANG Z. et al. Integrating multi-level deep learning and concept ontology for large-scale visual recognition. *Pattern Recognition*, Amsterdam, v. 78, p. 198-214, 2018.

[47] LI S. et al. Similarity-based future common neighbors model for link prediction in complex networks. *Scientific reports*, London, v. 8, n. 1, 1-11, 2018.

VOL.40 Nº2 2023
https://doi.org/10.22491/rmct.v40i2.10970.en

A study of densification and morphology in functionally graded materials of alumina ceramics doped with niobium oxide and silicon dioxide.

Anderson Alves Mota[1], **anderson.alves@ime.eb.br**
Alaelson Vieira Gomes[1], **alaelson@ime.eb.br**
[1] **Instituto Militar de Engenharia, Rio de Janeiro, RJ**

ABSTRACT: *Advanced Ceramic have several applications, among them we could highlight ballistic protection. This usage is mostly due to its mechanical strength and low weight. Alumina (Al2O3), given its characteristics such as easy to obtain and low production cost, represents one of the most researched and used for this purpose of use. However, every material has its own limitation of use, such as low density and bad strength when used without doping. Therefore, solutions have been researched to increase alumina density and improve microstructural to promote better ballistic performance. Even if the homogeneous material get better results, still there is some room for improvement on trying something new. One type of material which has been showing good development is Functionally Graded Materials that could promote a change in characteristics in the same material or that causes a material to behave similar to a ballistic system of several distinct layers, but with the advantage of having no stress concentrators as composites. Thus, this work aims to study the densification of Functionally Graded materials in conventional sintering and to observe microstructure characteristic of the layers in a Scanning Electron Microscope (SEM).*

KEYWORDS: Advanced Ceramics; Alumina; Niobium Oxide; Silicon Dioxide; Functionally Graded Materials.

RESUMO: *As cerâmicas avançadas apresentam diversas aplicações, com destaque para a proteção balística. Elas são bastante utilizadas nesse campo em virtude de apresentarem elevada força mecânica e baixo peso. A alumina (Al2O3), devido a algumas características, como facilidade de obtenção e baixo custo, representa um dos materiais mais pesquisados e utilizados para essa finalidade de emprego. Entretanto, todo material tem limitações de utilização e nem sempre atende a todos os requisitos impostos pela necessidade de utilização. Diante disso, soluções têm sido pesquisadas no sentido de aumentar a densificação da alumina e melhorar características microestruturais para promover um melhor desempenho balístico. Ainda assim, temos oportunidades de melhoria na pesquisa de materiais como no caso de gradiente funcional, promovendo uma mudança de características gradual no mesmo corpo cerâmico, o que faz com que um mesmo material tenha um comportamento semelhante a um sistema balístico de várias camadas distintas de materiais, com a vantagem de não ter as concentrações de tensão desses materiais compósitos. Dessa forma, este trabalho objetiva estudar a densificação de materiais processados a partir da técnica de gradiente funcional e sinterização convencional e observar a característica da microestrutura das camadas e desse gradiente em Microscópio Eletrônico de Varredura (MEV).*

PALAVRAS-CHAVE: Cerâmicas Avançadas; Alumina; Nióbia; Sílica; Gradiente Funcional.

1. Introduction

Ceramic materials have been widely studied and used as ballistic protection mainly due to their characteristics (such as low density and cost and high hardness and durability) that offer them good resistance for a relatively lower density than that of other materials used for this purpose. [1-3]

The development of projectiles with different shapes and great energy has challenged the development of new ballistic materials. This has led to an evolution in advanced ballistic personal protection systems due to their greater demands for new damage-resistant systems that have relative flexibility, weight fit for their use, and an efficient energy absorption capacity. [4]

The evaluation of a ceramic for a given use involves several factors, such as its ability to dissipate energy, physical properties, type of production process, and microstructure. [5]

In general, although silicon and boron carbides have lower densities than alumina (Al_2O_3), this component has more often integrated ballistic vehicle protection materials due to its simpler processing, lower cost, and better cost/benefit ratio. [6]

Dimensioning a material will ideally enable it to support tensile, compressive, or rotational stresses. Thus, any material in isolation rarely guarantees an adequate response to all types of stimuli, especially during ballistic impacts. [7]

Doping configures an efficient method to minimize these limitations. These components help to control the grain size of alumina during sintering and physical properties such as densification and mechanical strength. [8]

This research developed its alumina-based ceramic system (Al_2O_3) with 4% by weight of niobium pentoxide (Nb_2O_5) at the Military Institute of Engineering ceramic materials laboratory. One of the biggest gains in using this doping material in alumina-based bodies stems from its possibility of reducing the sintering temperature of non-additive alumina from 1600 to 1450°C. This reduction occurs by preserving the mechanical properties of alumina and enabling this system to integrate a ceramic component of ballistic armor. [9-10]

Another method to minimize the limitations of ceramic materials in isolation refers to assembling a multilayer shielding system formed by a first layer of ceramic material and another of a more ductile material, such as fiber-reinforced composites. [11-12]

Such shielding system assembly should improve the behavior of the ceramic material. Japanese researchers proposed another method for the same improvement in the 1980s. They needed to develop a material that would form a thermal barrier as the outer part of the material would be subjected to a temperature of about 2000 K and its inner part would have to remain at 1000 K. Such class of material is now known as functionally gradient materials. [13]

Functionally gradient materials consist of multi-layer materials whose constituents show varying volumetric fractions that are intentionally planned to ensure a progressive change in the microstructure of the material along its length. [14]

An advantage of functionally gradient materials over composites is that the joints of composite materials tend to concentrate stress, at which point most cracks generate delamination. [15]

However, producing a material with a functional gradient by cold uniaxial pressing and conventional sintering can result in materials with laminations and other defects that prevent it from further sintering. [16]

The stress concentrations due to the varying thermal behaviors of the materials in the layers cause such delamination. [17]

The alumina system (Al_2O_3) with 4% of added niobium pentoxide per weight (Nb_2O_5) and the alumina blend (Al_2O_3) with 4% by weight of niobium pentoxide (Nb_2O_5) and 0.8% by weight of silica (SiO_2) show very similar densification properties but considerable hardness differences. [10]

Thus, the main premise of this study is that these mixtures of materials can compose a functionally gradient material for ballistic applications (in which the hardest layer would constitute the impact surface) with great chances of good sintering without cracks and laminations.

Thus, this study aimed to analyze the sintering of ceramic bodies with a functional gradient based on alumina with 4% of its weight of niobium pentoxide (Nb_2O_5), and varying amounts of silica in its compositions (0.04-0.8%) and their densification, emergence of cracks, delamination, and morphology.

2. Materials and Methodology

2.1. Starting Materials

The materials used to produce the samples were: Nb_2O_5, obtained from Companhia Brasileira de Metalurgia e Mineração (Brazil); SiO_2, from the Sibelco brand; and Al_2Or_3 APC 11 SG from the manufacturer Alcoa (Brazil). Moreover, the organic additive Polyethylene glycol (PEG 300) from the company Isofar (Brazil) was added to give consistency to the product.

Table 1 shows the densities of the elements used to make the ceramics:

Table 1 - Density of the constituent elements in the produced ceramics.

Material	Density (g/cm³)
Nb_2O_5	4.60
SiO_2	2.65
Al_2O_3	3.96
PEG	1.13

The density of the powder mixtures was calculated considering the rule of mixtures given by equation 1, which considered the densities of each material and their mass fractions.

$$\rho = \rho_{Al_2O_3} \cdot m_{Al_2O_3} + \rho_{SiO_2} \cdot m_{SiO_2} + \rho_{Nb_2O_5} \cdot m_{Nb_2O_5} + \rho_{PEG} \cdot m_{PEG} \qquad (1)$$

In this experiment, three types of powder mixtures were produced with varying percentages of silica mass (Table 2).

Table 2 - Mass composition of the samples.

	Al_2O_3	SiO_2	Nb_2O_5	PEG
Mixture 1	91.6%	0%	3.82%	5%
Mixture 2	90.69%	0.39%	3.8%	5%
Mixture 3	90.84%	0.77%	3.82%	5%

Then, the density of each powder mixture was calculated using Equation 1. The results are shown in Table 3.

Table 3 - Theoretical density of the powders obtained by the rule of mixtures.

Material	Density (g/cm3)
Mixture 1	3.538
Mixture 2	3.529
Mixture 3	3.526

2.2. Sample processing

The materials were added to an alumina-lined jar to homogenize each powder mixture. Deionized water in a mass ratio of 1:1 and alumina balls were added to this material.

This system was taken to a ball mill for eight hours and dried in an oven at 80° C for 48 hours.

After drying, these mixtures were deagglomerated using a pistil and porcelain grail. Then, a sieve shaker was used to obtain the desired grain dimensions. The sieve shaker was run for three-minute periods using a sieve with a 0.355-mm (42 mesh) aperture.

After the three powder mixtures were prepared, these combinations were organized so that they generated seven groups of samples (each with three samples) when pressed. In total, three of these groups were composed of homogeneous materials, one of each mixture of the powders, called “control groups.” The other four groups, called “treatment groups,” were composed of materials with a functional gradient, three with two layers (groups AB, AC, and BC) and one with three layers (group ABC), according to Figure 1.

Figure 1 - Distribution of samples in the working groups

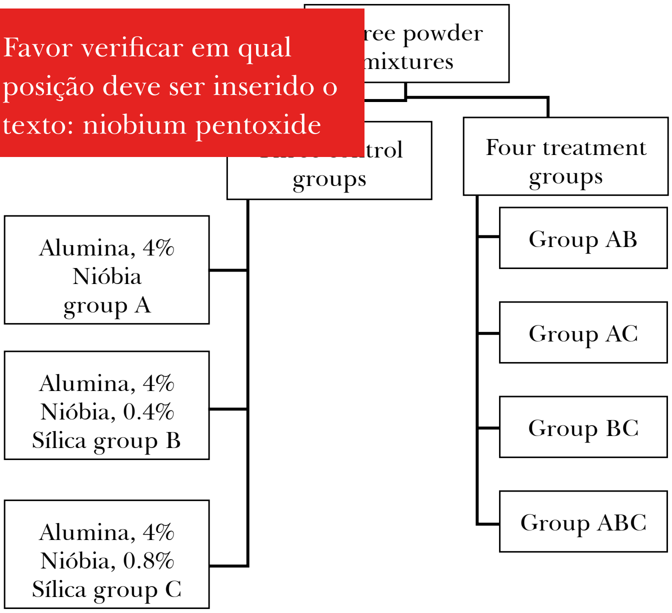

Favor verificar em qual posição deve ser inserido o texto: niobium pentoxide

The ceramic bodies were obtained by uniaxial cold pressing in a Skay press with a 30-ton capacity. The ceramic discs were prepared with 47-mm diameter dies using a 50-Mpa load. After pressing, the mass and thickness of each sample were measured.

Homogeneous group samples were pressed in two stages: first a preload was made to settle the material. Then, a main load of about 50 MPa was used to obtain the insert format for the mixture. In the groups whose samples consist of materials with a functional gradient, a preload was performed for each layer of the material; then, a main load of 50 MPa was made.

Sintering was carried out in two stages. In the first one, the binders were evaporated following Figure 2.

Figure 2 - Binder evaporation route

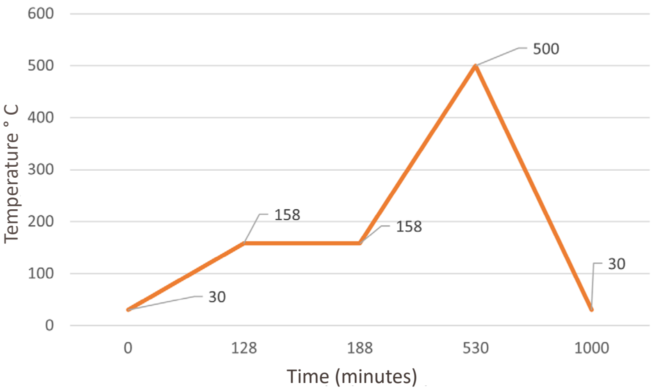

Then, the materials were placed in a Flyever INTI furnace with a FE50RPN controller to sinter the samples, according to Figure 3.

Figure 3 - Sintering route

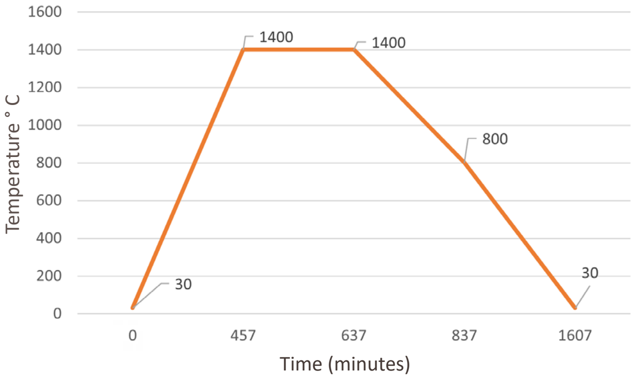

Then, after the sintered ceramic bodies were obtained, the characterization stages were carried out.

2.3. Characterization

2.3.1. Green density

From the theoretical densities in Table 3 and the masses and thicknesses measured after pressing, the green density and densification were calculated by Equation 2 and 3.

$$\rho_{green} = \frac{m_{sample}}{V_{sample}} \qquad (2)$$

$$Desinfication_{green} = \frac{\rho_{green}}{\rho_{theoretical}} \cdot 100\% \qquad (3)$$

2.3.2. Densification of Sintered Samples

Apparent and relative densities were calculated by the Archimedes method according to NBR 16667:2017 [18], using the measurements of immersed mass (m_i), wet mass (m_w), and dry matter (m_d), in which m_l represents the specific mass of the distilled water: 1 g/cm^3. With these parameters, the bulk and relative densities were evaluated by Equations 4 and 5 and the theoretical density of the body obtained by Table 3.

$$d_a(g/cm^3) = \frac{m_s}{m_u - m_i} \cdot m_l \qquad (4)$$

$$\rho_{relative} = \frac{d_a}{d_{theoretical}} \qquad (5)$$

2.3.3. X-ray Diffraction (XRD)

X-ray diffraction analysis was performed at IME using a Panalytical Xpert MRD diffractometer under Co-Kα radiation and a power of 40 kVe.

The starting powders and the sintered samples were thus analyzed: In the samples of groups 1, 2, and 3, this analysis was performed on only one side of the sample. In the samples of groups 4, 5, 6, and 7 (those with functional gradients), it was performed on both sides. A 30-mA current and a 5-to-80º scan were used as test parameters.

2.3.3. Scanning Electron Microscopy (SEM)

After the samples were fractured, the fracture surface was analyzed by SEM to obtain more information about the microstructure of the material and the interface of the layers of the functional gradient groups.

This analysis was performed in a QUANTA FEG 250 scanning electron microscope, in which a beam of 20 kVe and 5 μm in diameter was used. The increases were standardized at 1000, 5000, and 10,000 ×, except for cases in which the fractured surface was attempted to be observed as a whole, in which case 35 and 75 × were used.

3. Results and discussion

3.1 Green densification of Samples

Table 3 describes the green densification of the analyzed sample sets.

Table 4 - Green density of the samples.

Groups	Density (g/cm^3)	Green densification (%)
Group A	2.449 ± 0.043	68.57 ± 1.26
Group B	2.385 ± 0.018	67.32 ± 0.54
Group C	2.328 ± 0.055	65.73 ± 1.34
Group AB	2.384 ± 0.029	67.05 ± 0.81
Group AC	2.382 ± 0.033	66.85 ± 0.93
Group BC	2.374 ± 0.017	66.87 ± 0.40
Group ABC	2.374 ± 0.032	69.10 ± 0.90

The results show that adding silica decreased the densification of the ceramics by up to 2.84%, as in the literature [10]. The densification of the groups with functional gradient showed varying behavior in all cases. The ABC group stands out for having the highest densification, an expected result since each layer increasingly resist packaging and arrangement. Another important point is that all green densities averaged higher than 55%, the minimum level for good sintering.

3.2 Densification of sintered samples

Table 5 describes the results of relative density of the samples after sintering.

Table 5 - Relative densification of the sintered samples.

Groups	Relative humidity (%)
Group A	90.28 ± 0.75
Group B	88.26 ± 3.77
Group C	87.85 ± 5.42
Group AB	92.25 ± 3.75
Group AC	91.17 ± 3.30
Group BC	90.98 ± 1.55
Group ABC	93.23 ± 0.45

The results in Table 5 show a decrease in the densification of the material as silica was added, as in the literature [10,11].

Functional gradient samples averaged better densities than those with homogeneous material. The samples in the ABC group (three layers of material) again stand out for their densification. The greater number of layers increased sample densification, unlike the literature [16].

3.3 X-ray Diffraction (XRD)

Figures 4, 5, and 6 contain the diffractograms of each powder before pressing and sintering. Their mixtures show peaks corresponding to alumina, niobium pentoxide, and silica. This suggests no impurities in the starting materials, which could impair densification or cause reactions that would change the microstructure of the sintered material and the mechanical behavior of the final ceramic body.

Figure 4 - XRD of powder mixture A

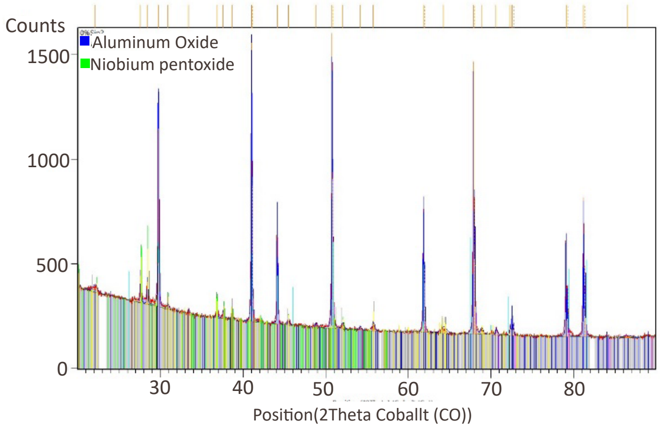

Figure 5 - XRD of powder mixture B Figure 4 – XRD of powder mixture A

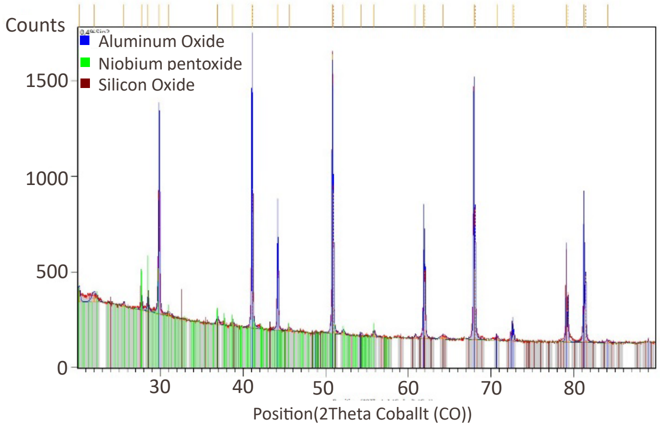

Figure 6 - XRD of powder mixture C Figure 4 – XRD of powder mixture A

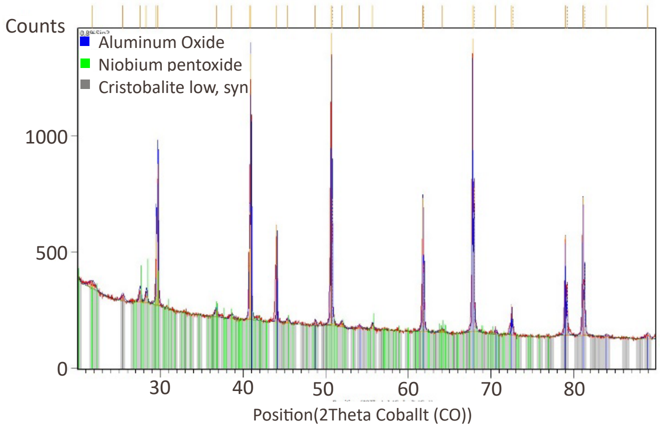

The diffractogram of the sintered samples indicated the presence of some phases in addition to those phases in the XRD of the powders.

A phase that plays a fundamental role in the greater densification of alumina by adding niobium pentoxide refers to aluminum niobate. This phase occurred in basically all sintered sample groups, as per Figure 7.

Figure 7 - XRD synthesized group A sample Figure 4 – XRD of powder mixture A

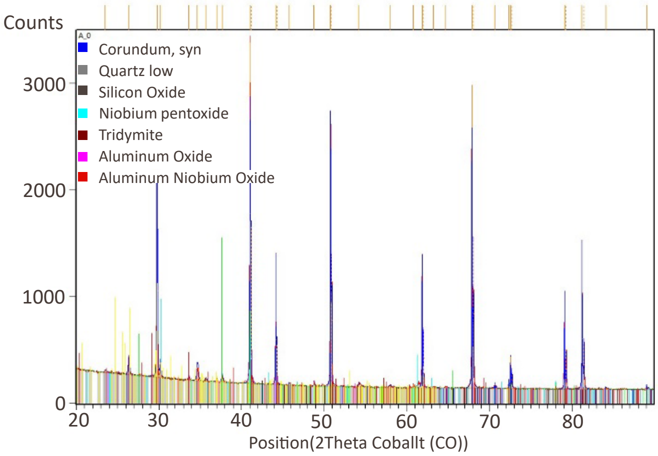

3.4 Scanning Electron Microscopy (SEM)

SEM at 1000-, 5000-, and 10000-× magnification obtained micrographs of the fractures in the materials. In the samples from the groups with functional gradient, analyses used a 35-× increase.

The image with a 35-× magnification shows satisfactory performed material compaction and sintering and no discontinuity in the transition between the material layers.

It also shows a predominantly intergranular fracture, which, in general, is inherent to materials with better impact energy absorption [10].

It also showed a greater porosity on the side of material C, which has 0.8% silica. This agrees with the densification of the material in this study.

Finally, an average grain size occurred on the side of material A, which shows that the silica influenced grain growth by mullite. [10]

Figure 8 - Image of the fracture of the ABC group material on the A-side of the material

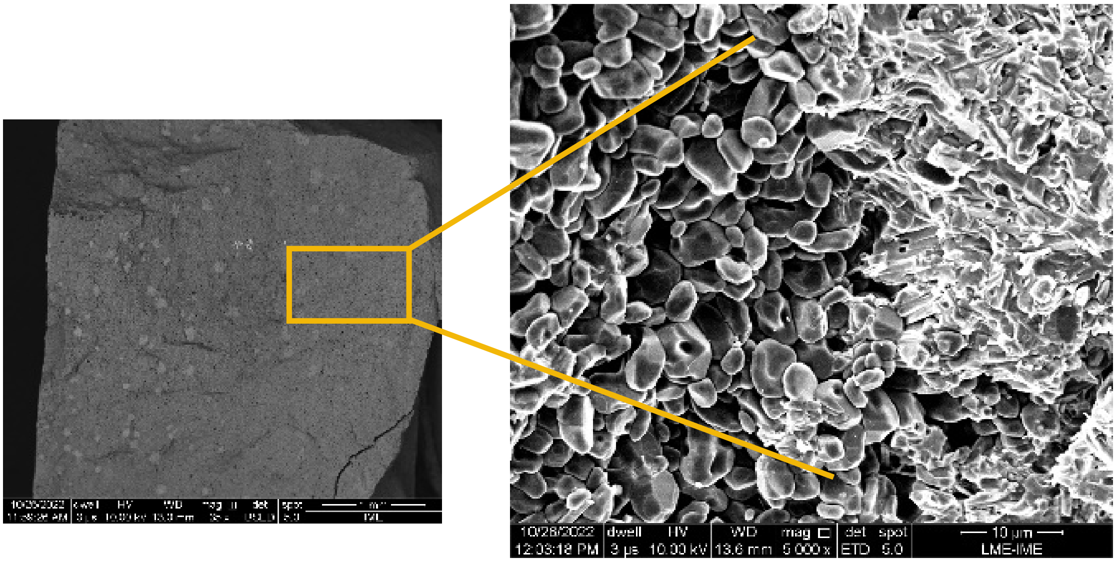

Figure 9 - Image of the fracture of the ABC group material on the C side of the material

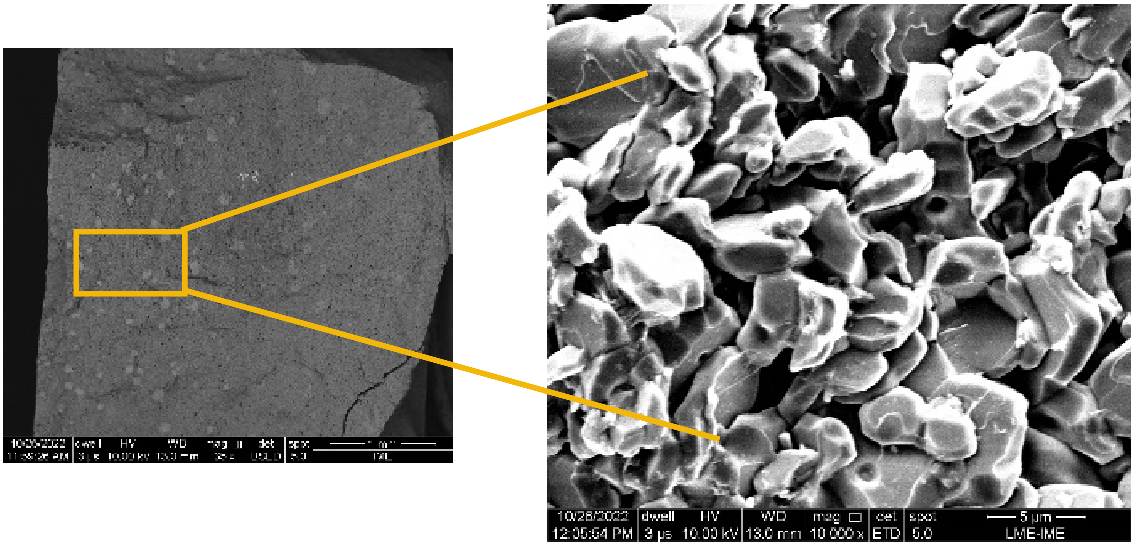

4. Conclusions

This study produced advanced ceramics from three mixtures of alumina powders in which 4% of their mass comprised niobium pentoxide and a variable composition of silica (0, 0.4, and 0.8%). These powder mixtures resulted in seven groups of ceramic bodies, each with three samples. The increase in layers may have influenced the increase in material densification. The materials with a higher presence of silica had a lower densification. Finally, cold uniaxial pressing with sintering in a conventional furnace showed success since the sintered samples showed no delamination and the transition of the material layers had no discontinuity in the SEM.

References

[1] APPLEBY-THOMAS, G. J. et al. Fitzmaurice, On the effects of powder morphology on the post-comminution ballistic strength of ceramics. International Journal of Impact Engineering, Amsterdam, v..100, p. 46-55, 2017.

[2] KOBAYASHI, A. Characteristics of high hardness alumina coatings formed by gas tunnel plasma spraying. Journal of Thermal Spray Technology, Berlin, v. 5, n. 3, p. 298-302, 1996.

[3] BAUDÍN, C.; TRICOTEAUX, A.; JOIRE, A. Improved resistance of alumina to mild wear by aluminium titanate additions. Journal of the European Ceramic Society, Amsterdam, v. 34, p. 69-80, 2014.

[4] YADAV, R. et al. Body armour materials: from steel to contemporary biomimetic systems. RSC Advances, London, n. 116, p. 115145-115174, 2016.

[5] MEDVEDOVSKI, E. Ballistic performance of armour ceramics: influence of design and structure. Part 1. Ceramics International, v. 36, n. 7, p. 2103-2115, 2010.

[6] CARTON, E..et al. Inertia as Main Working Mechanism for Ceramic Based Armour. Journal Contribution, [s. l.], 2019.

[7] SILVA, M. V. et al. Blindagens Cerâmicas para Aplicações Balísticas: uma revisão. Cerâmica, São Paulo, v. 60, n. 355, p. 323-331, 2014

[8] MILAK, P. et al. The influence of dopants in the grain size of alumina – A review. Materials Science Forum, Bäch, v. 820, p. 280-284, 2015.

[9] GOMES, A. V. Comportamento balístico da alumina com adição de nióbia e variação da geometria do alvo. Tese (Doutorado em Ciências dos Materiais) –,Instituto Militar de Engenharia, Rio de Janeiro, 2004.

[10] GOMES, A. V. Comportamento Balístico de alumina com adições de nióbia, sílica e magnésia. Dissertação (Mestrado em Ciências dos Materiais) – Instituto Militar de Engenharia, Rio de Janeiro, 1999.

[11] BÜRGER, D. et al. Ballistic impact simulation of an armour-piercing projectile on hybrid ceramic/fiber reinforced composite armours. International Journal of Impact Engineering, Amsterdam, v. 43, p. 63-77, 2012.

[12] NASCIMENTO, L. F. C. Caracterização do compósito de epóxi/fibra de malva para emprego em blindagem balística multicamada. Tese (Tese de Doutorado) – Instituto Militar de Engenharia, Rio de Janeiro, 2017.

[13] MAHAMOOD, R. M. et al. Functionally graded material: an overview. International Association of Engineers (IAENG), 2012.

[14] Shanmugavel, P et al. An overview of fracture analysis in functionally graded materials. European Journal of Scientific Research, [s. l.], v. 68, n. 3, p. 412-439, 2012.

[15] WANG, S. S. Fracture mechanics for delamination problems in composite materials. Journal of Composite Materials, Thousand Oaks, v. 17, n. 3, p. 210-223, 1983.

[16] JESUS, P. R. R. Processamento e caracterização de um material cerâmico à base de alumina com gradiente funcional para aplicações balísticas. Tese (Doutorado em Ciências dos Materiais) – Instituto Militar de Engenharia, Rio de Janeiro, 2021.

[17] LEUSHAKE, U. et al. General aspects of fgm fabrication by powder stacking. In: TRANS TECH PUBL. Materials science forum. [S.l.], 1999. v. 308.

[18] ABNT – Associação Brasileira de Normas Técnicas. ABNT NBR 16661:2017: Material refratário denso conformado – determinação de volume aparente, volume aparente da parte solida, densidade da massa aparente, densidade aparente da parte solida, porosidade aparente e absorção. Rio de Janeiro: ABNT,.2017.

VOL.40 Nº2 2023
https://doi.org/10.22491/rmct.v40i2.11051.en

Estimation of target azimuth based on multiple beamforming processes in a phased array radar system

Vitor Augusto Ferreira Santa Rita*1, Alberto Gaspar Guimarães2, Ernesto Leite Pinto3
1Military Institute of Engineering (IME), Rio de Janeiro (RJ), Brazil, vitoraugusto.rita@ime.eb.br
2Universidade Federal Fluminense (UFF), Niterói (RJ), Brazil, agaspar@id.uff.br
3Military Institute of Engineering (IME), Rio de Janeiro (RJ), Brazil, ernesto@ime.eb.br

---

Abstract: *This study investigates the combination of maximum likelihood (ML) with a reduced number of fixed beam steering to estimate target azimuth in a surveillance radar-based system equipped with sensor array. This study describes simulation-based performance results of the estimator using only two fixed beams. It found the great advantage of the ML solution when compared to a usual monopulse estimator, which employs the same number of beams. Additional results show that the investigated ML approach using only one additional beam can obtain greater performance gains.*

Keywords: *Radar. Azimuth Estimation. Antenna Array. Beamforming. Maximum Likelihood.*

Resumo: Investiga-se neste trabalho o emprego de uma abordagem de máxima verossimilhança (ML, de “maximum likelihood”) combinada com um número reduzido de conformações de feixe fixas para realizar a estimação do azimute de um alvo num sistema radar de vigilância munido de arranjo de sensores. São apresentados resultados de simulação para avaliação de desempenho do estimador com base em apenas duas conformações. É possível verificar que há grande vantagem do estimador ML em comparação com um estimador monopulso amplamente utilizado que se vale da mesma quantidade de conformações. Resultados adicionais mostram que ganhos maiores de desempenho podem ser obtidos com a abordagem ML aqui investigada utilizando apenas uma conformação de feixe a mais.

Palavras-chave: Radar. Estimação de Azimute. Arranjo de Antenas. Conformação de Feixe. Máxima Verossimilhança.

1. Introduction

The use of antenna array and digital signal processing in radar systems configures an important current resource use that can spatially filter signals, among other operations [1-2]. An important issue in this context refers to estimating the azimuth of a target in relation to radar reference. The literature has several proposals with such aim [3-4].

This study focuses on azimuth estimation in search and surveillance radars [5] that use a linear array of antennas.

Search and surveillance radars generally follow a processing routine in a large volume of space in which:

- the reference direction of the antenna is moved to the center of a sector at each time interval to detect the target and, in case of detection, estimate its position;
- Then, the reference direction to direct the antenna is moved to the center of a neighboring sector to progressively cover the entire region of interest.

Both primary and secondary radars follow this basic routine. The difference for the problem this study addresses refers to the origin of the received signal [5]. In the first case, the signal results from an echo produced by the target in the reference direction in response to a previous transmission from the primary radar. In the second case, the signal is received from a transmission made by a cooperative transmitter (transponder).

In both applications, it is of great interest that the azimuth estimator has great accuracy in the widest possible angular range around the radar reference direction [6-7], which can reduce the total coverage time of the region of interest and thus increase the update rate of the position information of target [8]. This study will refer to the ability to satisfactorily estimate azimuths around reference directions as the *coverage* of the azimuth estimator.

Another desirable requirement for an azimuth estimator in search and surveillance radars refers to a reduced computational complexity due to the need to repeat its operation at short intervals of time.

A well-known example of a low computational complexity azimuth estimator refers to monopulse techniques [5], originally implemented using two receiving antennas with distinct angular responses. These techniques estimate the azimuth by a linear approximation of the ratio between the difference and the sum of the signals coming from the above-mentioned antennas, called monopulse ratio.

In the case of an azimuth estimator based on a linear array of antennas, an alternative to reduce its complexity refers to using a limited number of fixed beam conformations obtained by appropriate linear combinations of the signals received in the array. The literature on signal processing offers other uses of fixed beam conformations, such as in [9-12].

Overall, two-fixed beam formations can implement a monopulse-type estimator with a linear antenna array, producing very low-complexity solutions. However, monopulse techniques only obtain satisfactory estimations if the target is in a small region close to the antenna reference direction [5,7,13]. In other words, these techniques have small coverage.

Note that, despite the low possibility of detecting a target outside this region, it must still be considered. In such cases, a monopulse technique generates high estimation errors [14], which can be corrected in other processing steps of a radar receiver, but the search for alternatives to avoid or reduce them remains of interest [13].

This study aims to develop and evaluate a more comprehensive estimator using the maximum likelihood technique (ML [15]) using a reduced number of fixed beam formations.

This research first deduces an ML estimator based on multiple beam conformations that address two other unknown parameters in addition to the azimuth. Then, it focuses on azimuth estimation under conditions equal to or close to those usually admitted for the use of monopulse techniques.

The implementation of ML estimators in this research requires a numerical optimization to find the value of the argument that maximizes the objective function. We opted for particle swarm optimization (PSO) [16-18] for this.

This study shows, by simulation results, that the ML approach in a small set of fixed beam conformations can significantly increase the estimation range when compared to a typical monopulse technique.

This study is organized into six sections. Section II describes the model of the adopted system. Section III offers the investigated estimation strategy, section IV shows the equation of the monopulse technique used as reference, and section V describes the results of performance evaluation. Finally, section VI offers the main conclusions of this study.

2. System Model

This study uses an arrangement composed of N_a omnidirectional antenna elements spaced from each other by a fixed distance d along a linear structure. Figure 1 illustrates this type of arrangement.

Fig. 1 - Antenna array model.

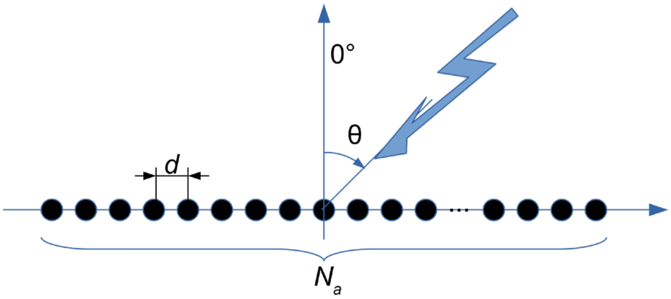

The arrangement enables passive reflection by the target of the signal sent by a primary radar or transmission by a cooperative transmitter with reception of the signal by a secondary radar. Both situations consider that the wavefront from the target falls on the radar at an angle θ with the direction normal to the linear arrangement (Fig. 1).

Considering a scenario with primary radar, the complex envelope of the transmitted signal is given by

$$\tilde{s}_t(t)=\alpha_t(\theta)\rho(t), \qquad t\in\left[0,N_pT\right], \tag{1}$$

in which

$$\rho(t)=\sum_{m=0}^{N_p-1}p(t-mT), \tag{2}$$

in which *Np* refers to the number of sequential pulses; *T*, the time interval between pulses; $p(t)$ the basic transmitted pulse shape; and $\alpha_t(\theta)$ a complex amplitude the modulus of which is related to the transmission power in the direction *θ*.

The baseband equivalent of the signal received by the *k*-th sensor array can be expressed as [11]

$$x_k(t)=\alpha_r(\theta)\rho\left(t-\tau-\frac{kd}{c}sen\theta\right)e^{-j2\pi\left(f\ \tau+k\frac{}{\lambda}sen\theta\right)} \\ +z_k(t), \tag{3}$$

with $k\in\{0,\cdots,N_a-1\}$. The terms f_c and λ denote, respectively, the frequency and wavelength of the carrier, *c* is the speed of light and τ is the delay in relation to the moment of transmission.

The breadth of $\alpha_t(\theta)$ depends on the strength from the target (by self-transmission or reflection, depending on the type of radar) and the gain of the reception diagram in *θ*. This study takes $\alpha_t(\theta)$ as unknown, but not random in nature.

In turn, $z_k(t)$ represents the thermal noise from the *k*-th sensor, which is modeled as a complex Gaussian process with a zero mean and constant power spectral density in a much larger frequency range than that occupied by the signal of interest. Equation (3) ignores a possible Doppler shift of the signal frequency — although this assumption is reasonable for many applications [19].

This study assumes[1] that $N_ad/c\ll\tau$, redefining the complex amplitude by incorporating lag factors that are independent of the position of the sensor. Thus, expression (3) is rewritten as

$$x_k(t)\approx\alpha\rho(t-\tau)e^{-j2\pi\left(k-\frac{N_a-1}{2}\right)\frac{d}{\lambda}sen\theta}+z_k(t), \tag{4}$$

in which: $\alpha=\alpha_r(\theta)e^{-j\pi\left(2f_c\tau+(N_a-1)\frac{d}{\lambda}sen\theta\right)}$.

It is important to note that α depends on *θ* and . However, the problem defined here will disregard dependence, as in [19,20].

Rewriting (4) in vector notation, we have

$$x(t)=\alpha\rho(t-\tau)a(\psi)+z(t), \tag{5}$$

in which $\boldsymbol{x}(t)=\left[x_k(t)\right]_{k=0}^{N_a-1}$ and $\boldsymbol{z}(t)=\left[z_k(t)\right]_{k=0}^{N_a-1}$ configure dimension column vectors $N_a\,\mathrm{x}1$ and $\boldsymbol{a}(\psi)$, the *vector director*, given by

$$\boldsymbol{a}(\psi)=\left[e^{j\left(\frac{N_a-1}{2}\right)\psi}\cdots e^{-j\left(\frac{N_a-1}{2}\right)\psi}\right]^{\mathrm{T}}, \tag{6}$$

in which

$$\psi=2\pi\frac{d}{\lambda}sen\theta \tag{7}$$

with, $\theta\in[-\pi/2,\pi/2]$

The signals generated at the output of the sensors ar applied as a set of N_c fixed bundle forming, as shown in Figure 2, which illustrates the sequence of the main operations performed on the receiver.

The signals generated by the conformations are given by

$$y(t)=W^Hx(t)\,y(t)=W^Hx(t) \tag{8}$$

$$=\alpha\rho(t-\tau)g(\psi)+v(t), \tag{9}$$

---

[1] A valid assumption since the distance from the radar to the target is usually much greater than N_ad.

in which

$$g(\psi)=W^{\mathrm{H}}a(\psi), \qquad (10)$$

$$v(t)=W^{\mathrm{H}}z(t) \qquad (11)$$

and W is the fixed forming matrix with $N_a \mathrm{x} N_c$. dimensions. Each column of this matrix corresponds to the normalized beamforming vector in a given direction $\theta_c \in [-\pi/2, \pi/2]$, defined as

$$w_{\psi_c} \underline{\underline{def}} \frac{1}{\sqrt{N_a}} a(\psi_c), \qquad (12)$$

with $c \in \{1, \cdots, N_c\}$, $a(.)$ defined in Equation (6) and $\psi_c = 2\pi \frac{d}{\lambda} sen\theta_c$.

Fig. 2 - Receiver block diagram.

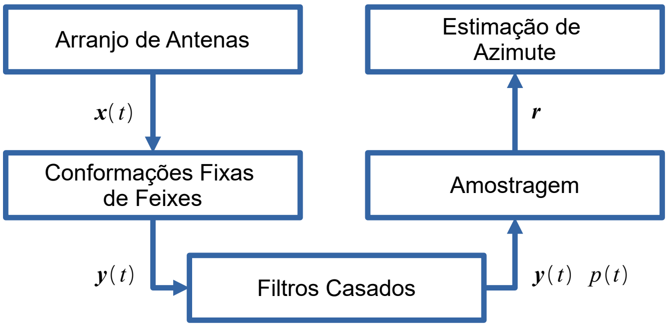

Note that if W unitary, i.e., $WW^{\mathrm{H}}=I$, the noise vector $v(t)$ has the covariance matrix $E\left[v(t)v^{\mathrm{H}}(t)\right]=\sigma^2 I$. [15] has shown that this condition is achieved if $\theta_{c_i}-\theta_{c_j}=2k\pi/N_a$, $\forall c_i, c_j \in \{0, \ldots, N_c-1\}$ and $k \in Z$.

As Figure 2 shows, the signals resulting from the beam conformations pass through matched filters and are sampled, giving rise to the input of the azimuth estimator. The sampling times given by

$$t_{l,m}=t_0+(l-1)T_a+(m-1)T, \qquad (13)$$

toward $m \in \{1, \ldots, N_p\}$ and $l \in \{1, \ldots, L\}$ in which L is the number of successive samples per pulse and T_a, the time interval between samples.

This study takes that the pulse at the outlet of the matched filter has significant energy in the range of T_p seconds and that the initial instant T_0 is such that

$$t_0 \in \left[\tau - T_p/2; \tau + T_p/2\right]. \qquad (14)$$

Figure 3 shows an example in which the pulse at the outlet of the matched filter is triangular.

Figure 3 - Example of sampling instants.

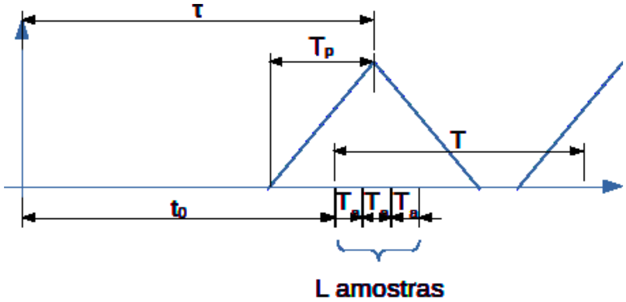

The N_pL samples obtained for each beam conformation are assembled in the vector r dimension $(N_cLN_p)\mathrm{x}1$ given by

$$r=\alpha n(\psi,\tau)+, \qquad (15)$$

in which

$$\boldsymbol{\varsigma}(\psi,\tau)=\begin{bmatrix} g_1(\psi)\div_\tau \\ g_2(\psi)\div_\tau \\ \vdots \\ g_{N_c}(\psi)\div_\tau \end{bmatrix}, \qquad (16)$$

in which $g_c(\psi)$ is the c-th element of the vector $g(\psi)$ in Equation (10) and χ_τ is a vector with a $(LN_p)\mathrm{x}1$ dimension with samples from the square wave resulting from the filtering of $\rho(t-\tau)$ obtained at moments $t_{l,m}$.

Still in expression (15), the noise vector n it is Gaussian with a null mean, which can be expressed as

$$n=\begin{bmatrix} n_1 & \cdots & n_{N_c} \end{bmatrix}^T, \qquad (17)$$

In which n_c is the column vector that gathers the samples of the filtered noise associated with the *c*-th conformation.

Therefore, from (15), the vector of observations *r* Gaussian with the following vector mean

$$\mu = E\left[r\right] = \alpha\eta\left(\psi,\tau\right) \qquad (18)$$

and the following covariance matrix

$$\Sigma = E\left[\left(r-\mu\right)\left(r-\mu\right)^{\mathrm{H}}\right] = E\left[nn^{\mathrm{H}}\right], \qquad (19)$$

which can be expressed in blocks such as

$$\Sigma = \begin{bmatrix} \Sigma_{c_1c_1} & \cdots & \Sigma_{c_1c_{N_c}} \\ \vdots & \ddots & \vdots \\ \Sigma_{c_{N_c}c_1} & \cdots & \Sigma_{c_{N_c}c_{N_c}} \end{bmatrix}, \qquad (20)$$

in which $\Sigma_{c_ic_j} = \mathrm{E}\left[n_{c_i}n_{c_j}^{\mathrm{H}}\right]$with $c_i, c_j \in \{1,\cdots,N_c\}$.

3. ML Estimation

The vector of observations *r* in Equation (15) is Gaussian, with only the mean vector dependent on the parameters $\left(\alpha,\tau,\psi\right)$. Therefore, the logarithmic likelihood function [15] can be expressed as

$$l\left(\left(\alpha,\tau,\psi\right);r\right) =$$

$$\frac{-1}{2}\left(r-\alpha\eta\left(\psi,\tau\right)\right)^{H}\Sigma^{-1}\left(r-\alpha\eta\left(\psi,\tau\right)\right)+\xi, \qquad (21)$$

in which ξ is a scalar constant that dispenses with the parameters α,τ and ψ. The maximum likelihood estimate [15] of these parameters is the argument that maximizes $l(.)$ or, equivalently,

$$\left(\hat{\alpha}_{ML}\left(r\right),\hat{\tau}_{ML}\left(r\right),\hat{\psi}_{ML}\left(r\right)\right) = \underset{(\aleph,\ ,\ )}{argmin}\ \nu\left(\alpha,\tau,\psi;r\right), \qquad (22)$$

in which

$$\nu\left(\alpha,\tau,\psi;r\right) = \left(r-\alpha\eta\left(\psi,\tau\right)\right)^{\mathrm{H}}\Sigma^{-1}\left(r-\alpha\eta\left(\psi,\tau\right)\right). \qquad (23)$$

The estimate $\hat{\alpha}_{ML}\left(r\right)$ can be obtained from the equation below, which establishes a necessary condition for minimizing $\nu(.)$, depending on the parameter α:

$$\left.\frac{\partial\nu}{\partial\alpha}\right|_{\alpha=\hat{\alpha}_{ML}} = 0. \qquad (24)$$

After some algebraic manipulations, considering that Σ dispenses with α, we arrive at

$$\hat{\alpha}_{ML}\left(r\right) = \frac{\boldsymbol{ç}^{H}\left(\psi,\tau\right)\boldsymbol{Ó}^{-1}\boldsymbol{r}}{\boldsymbol{ç}^{H}\left(\psi,\tau\right)\boldsymbol{Ó}^{-1}\boldsymbol{ç}\left(\psi,\tau\right)}. \qquad (25)$$

With the above result, the strategy adopted to determine the ML estimate of $\left(\tau,\psi\right)$ refers to replacing Equation (25) in Equation (23), obtaining, after a few steps, the following solution:

$$\left(\hat{\tau}_{ML}\left(r\right),\hat{\psi}_{ML}\left(r\right)\right) = \underset{(\tau,\psi)}{argmax}\frac{\left|\boldsymbol{ç}^{H}\left(\psi,\tau\right)\boldsymbol{Ó}^{-1}\boldsymbol{r}\right|^{2}}{\boldsymbol{ç}^{H}\left(\psi,\tau\right)\boldsymbol{Ó}^{-1}\boldsymbol{ç}\left(\psi,\tau\right)}, \qquad (26)$$

which requires the implementation of numerical optimization.

Once the estimates of $\left(\hat{\tau}_{ML}\left(r\right),\hat{\psi}_{ML}\left(r\right)\right)$, we return to Equation (25) to obtain $\hat{\alpha}_{ML}\left(r\right)$.

3.1 Unit conformation matrix

If the matrix *W* of conformation is unitary, it is easy to find that $\Sigma_{c_ic_j} = 0$ (null array) to $i \neq j$. This shows, based on the expression in Equation (20), that Σ configures a diagonal block matrix.

Thus, the ML estimates of the parameters of interest are given by

$$\left(\hat{\tau}_{ML}\left(r\right),\hat{\psi}_{ML}\left(r\right)\right) = \underset{(\tau,\psi)}{argmax}\frac{\left|\sum_{c=1}^{N_c}g_c\left(\psi\right)\chi_{\tau}^{\mathrm{H}}\Sigma_{cc}^{-1}r_c\right|^{2}}{\sum_{c=1}^{N_c}\left|g_c\left(\psi\right)\right|^{2}\chi_{\tau}^{H}\Sigma_{cc}^{-1}\chi_{\tau}} \qquad (27)$$

and

$$\hat{\alpha}_{ML}\left(r\right) = \left.\frac{\sum_{c=1}^{N_c}g_c\left(\psi\right)\chi^{\mathrm{H}}\Sigma_{cc}^{-1}r_c}{\sum_{c=1}^{N_c}\left|g_c\left(\psi\right)\right|^{2}\chi_{\tau}^{\mathrm{H}}\Sigma_{cc}^{-1}\chi_{\tau}}\right|_{\substack{\tau=\hat{\tau}_{ML}\left(r\right)\\ \psi=\hat{\psi}_{ML}\left(r\right)}}, \qquad (28)$$

in which r_c the vector of observations obtained for the *c*-conformation.

Note that the vectors and matrices in Equation (27) have dimensions N_c times smaller than in Equation (26), making the optimization procedure computationally much simpler.

3.2 Numerical optimization

We chose to use the PSO technique to numerically obtain the azimuth and delay estimates in equations (26) and (27).

The original PSO algorithm was described in [17]. It uses a swarm formed by a set of particles that evolves over iterations to perform a very flexible scan of the search space for the optimal value of the objective function. Use cases of the PSO algorithm in ML parameter estimation have been described, for example, in [16,18,21]. This study chose the version of this algorithm called Accelerated Particle Swarm Optimization (APSO), which shows rapid convergence [22].

4. Monopulse technique

Monopulse-type techniques [5] based on a linear array of sensors simultaneously generate two values resulting from beam conformations (Figure 4). Calculating the ratio between the difference and the sum of these values obtains the monopulse ratio, which is used to achieve the azimuth estimate.

Fig. 4 - Azimuth estimation by monopulse radar with sensor array.

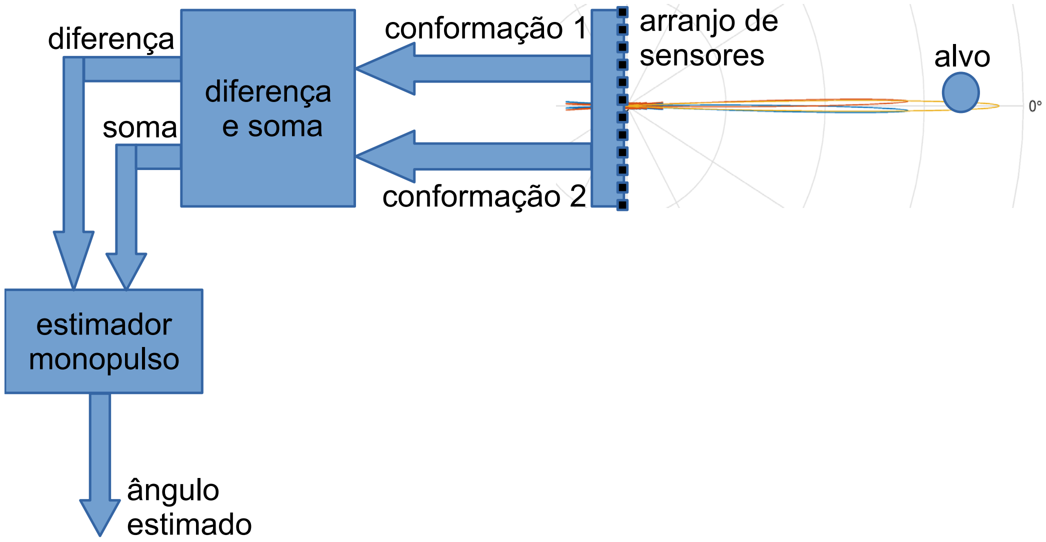

4.1 Monopulse amplitude

The specific case of the monopulse amplitude technique define the two beam formations with symmetrical inclinations in relation to the direction normal to the linear arrangement. $w_{\psi_{+\grave{o}}}$ and $w_{\psi_{-\grave{o}}}$ refer to the used conformation vectors, corresponding respectively, to the $\psi_{+\grave{o}}$ and $\psi_{-\grave{o}}$ slopes, which are expressed according to equation (12).

Moreover, after filtration, the signals from these conformations are sampled at instant $t = t_0 = \tau$, obtaining, based on equations (15) and (16), the vector given by

$$r = \begin{bmatrix} \alpha\chi_1 w^{\mathrm{H}}_{\psi_{+\grave{o}}} a(\psi) + n_{\psi_{+\grave{o}}} \\ \alpha\chi_1 w^{\mathrm{H}}_{\psi_{-\grave{o}}} a(\psi) + n_{\psi_{-\grave{o}}} \end{bmatrix} \cdot , \qquad (29)$$

In which $n_{\psi_{+\grave{o}}}$ and $n_{\psi_{-\grave{o}}}$ are noise samples associated with the respective conformations.

The monopulse ratio consists of

$$\beta \overset{def}{=\!=} \frac{r_1 - r_2}{r_1 + r_2} \,, \qquad (30)$$

in which r_1 and r_2 are the first and second elements of r in the Equation (29) , respectively.

The idealized monopulse ratio disregards the noise portions in Equation (30), given by

$$\beta_{id}(\psi) \overset{def}{=\!=} \frac{\left(\boldsymbol{w}^{\mathrm{H}}_{\psi_{+\grave{o}}} - \boldsymbol{w}^{\mathrm{H}}_{\psi_{-\grave{o}}}\right)\boldsymbol{a}(\psi)}{\left(\boldsymbol{w}^{\mathrm{H}}_{\psi_{+\grave{o}}} + \boldsymbol{w}^{\mathrm{H}}_{\psi_{-\grave{o}}}\right)\boldsymbol{a}(\psi)} \,. \qquad (31)$$

Substituting equations (12) and (6) into the previous equation and assuming an odd N_a2 obtains, after some algebraic manipulations,

$$\beta_{id}(\psi) = \frac{\sum_{k=1}^{(N_a-1)(N_a-1)/2} sen(k\psi)\, sen(k\psi_{\grave{o}})}{1/2 + \sum_{k=1}^{(N_a-1)(N_a-1)/2} cos(k\psi)\, cos(k\psi_{\grave{o}})} \,. \qquad (32)$$

The linear approximation of $\beta_{id}(\psi)$ around $\psi = 0$ is given by

$$\beta_{id}(\psi) \approx \beta'_{id}(0)\psi \,, \qquad (33)$$

in which $\beta'_{id}(0)$ is the derivative of $\beta_{id}(\psi)$ in $\psi = 0$, which can be calculated by the expression

$$\beta'_{id}(0) = \frac{\sum_{k=1}^{(N_a-1)(N_a-1)/2} ksen(k\psi_{\grave{o}})}{1/2 + \sum_{k=1}^{(N_a-1)(N_a-1)/2} cos(k\psi_{\grave{o}})} \,. \qquad (34)$$

Assuming that the real part of the measured monopulse ratio in Equation (30) can be approximated by $\beta_{id}(\psi)$ and that this can be approximated by (33), we finally arrive at the following expression for the estimate of ψ. Using this monopulse amplitude technique:

Fig. 5 - Illustration of the evolution of four swarm particles in the implementation of the ML(2) estimator with SNR = 20 dB and target azimuth at 0 rad.

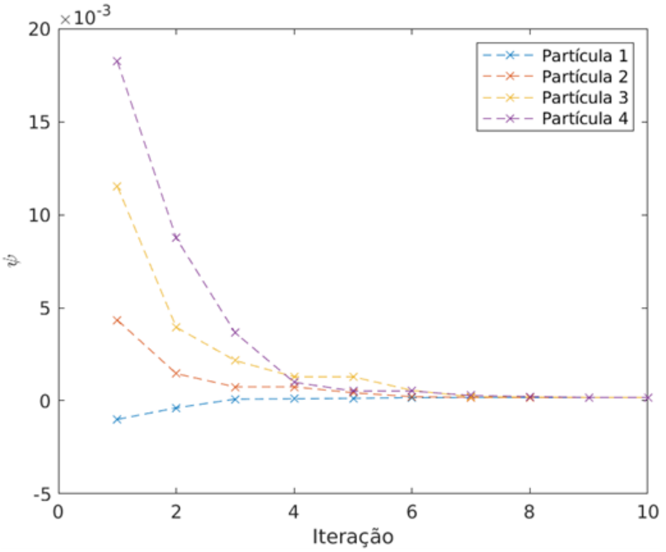

$$\hat{\psi}_{mp} = \frac{\Re e[\beta]}{\beta'_{id}(0)} \,, \qquad (35)$$

In which $\Re e[.]$ denotes the actual part of the argument and $\beta'_{id}(0)$, a constant calculated using equation (34).

5. Performance Assessment

This study carried out simulations of a radar receiver with a radar array, with $N_a = \ddot{u}$ elements spaced $d = \lambda / 2$ apart and a signal with a basic rectangular pulse.

The considered signal-to-noise ratio (SNR) is given by dividing the average power of the signal of interest at the input of the array by the average noise power in the frequency range occupied by this signal. For this, the bandwidth was considered the inverse of the duration of the basic pulse.

The comparison with amplitude monopulse only considered two conformations ($N_c = 2$) in the use of the ML technique.

In the following text, ML(N_c) denotes the ML estimation technique with N_c conformations and MA, the monopulse amplitude estimator above.

---

[2] The development considering N_a pair is quite similar.

This comparison assumes the delay parameter (τ) is known, which is usually done in studies addressing monopulse techniques [5,6,7,14].

In more specific terms, ML estimates were obtained as a solution to the optimization problem in ψ with the objective function given by equation (26), assuming the known value of τ . It is worth remembering that ψ has a one-to-one relation with the physical angle of arrival of the signal at the input of the array in Equation (7).

Regarding the APSO algorithm, the number of used particles totaled 30 and the number of iterations until the stop was empirically adjusted and totaled 15.

Figure 5 illustrates the evolution over iterations of the four-particle azimuth estimate cluster by the APSO algorithm, which was obtained with SNR = 20 dB and target azimuth at 0 rad.

In Figure 5 shows that, from the eighth iteration onward, a significant concentration of estimates occur around the real value of the target angle.

On the other hand, Figure 6 shows three examples of the evolution of estimation error obtained with a swarm of 30 particles and 30-, 20-, and 10-dB SNRs.

A rapid stabilization of the error and coherence between SSR and error occur, in the sense that the increase in the former is associated with the reduction of the latter. Other tests of this type have observed similar behaviors.

Figure 6 - Estimation error with the ML(2) technique and different RSR values.

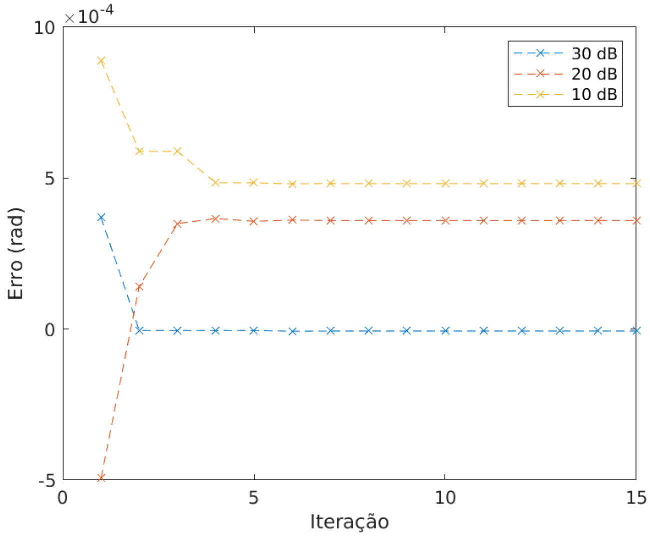

This study now describes the results of empirical evaluation of polarization, variance, and mean square error (MSE) of different estimators, obtained based on 2,000 independent achievements.

A first performance comparison between the ML(2) and MA techniques was performed with slopes $\psi_{\pm\delta} = \pm 0,028$ Rad. Figure 7 shows the results obtained with a 10-dB of SNR.

This figure evinces that the performance of the MA estimator is practically identical to that of the ML(2) estimator for low values of target azimuth, with very significant differences for higher values, especially the growth of the polarization of the monopulse estimator above 0.04 rad. It is also noticed that the performance degradation of this estimator increases to higher azimuth values, so the MSE increases rapidly.

These performance characteristics of the MA estimator can, to a large extent, be seen as a direct consequence of the inaccuracy in the linear approximation of the monopulse ratio, which increases with greater azimuth values. Figure 8 illustrates this effect for the idealized monopulse ratio corresponding to the conditions in Figure 7.

Figure 7 - Performance of ML(2) and MA estimators as a function of target azimuth with a 10-dB SNR.

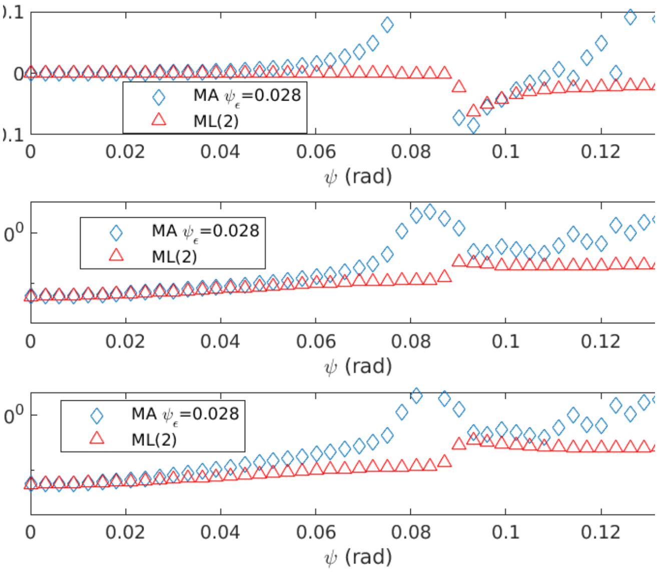

VOL.40 Nº2 2023
https://doi.org/10.22491/rmct.v40i2.11051.en

Figure 8 shows that, in fact, the linear approximation is satisfactory for azimuth values slightly below 0.04 rad and becomes generally inadequate with azimuths above this value.

Figure 8 - Idealized MA ratio and its linear approximation as a function of the target azimuth.

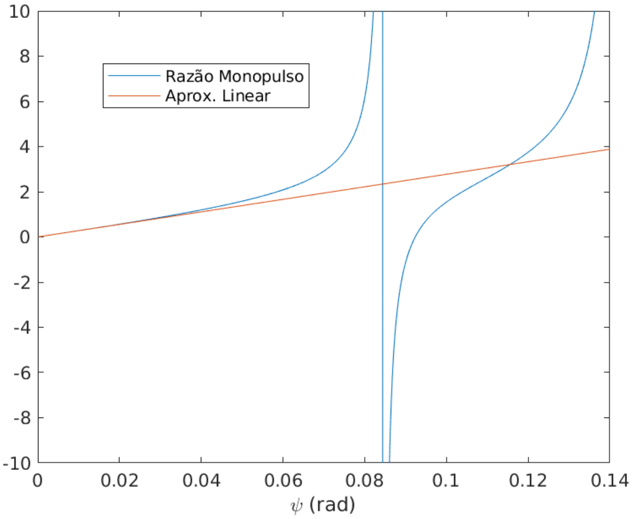

Regarding the ML(2) estimator, Figure 7 shows it has practically negligible polarization for azimuth values up to about 0.09 rad.

The results of this figure show, as a whole, that the ML(2) estimator has a significantly higher overall performance than the MA estimator for azimuth values from 0.04 to 0.09 rad, significantly increasing *coverage*.

Figure 9 results were obtained with an SNR of 20 dB and the same slopes $\psi_{\pm\grave{o}} = \pm 0{,}028$ Rad. These results confirm the increase in *coverage* from the ML(2) estimator when compared to MA. In particular, results are practically identical to those of Figure 7 regarding polarization comparison.

This research performed a more detailed analysis of the objective function of the ML(2) estimator was performed and found that the increase in the azimuth of the target can lead to the frequent occurrence of two local minima of this function, as illustrated in the example in Figure 10.

In this figure, the objective function the ML(2) estimator used shows two very close minimum values, associated with values that quite differ from its argument, one of which corresponds to the correct azimuth of the target. Situations similar to this can lead to high estimation errors and consequent increase in the MSE.

Figure 9 - Performance of ML(2) and MA estimators as a function of target azimuth with a 20-dB SNR.

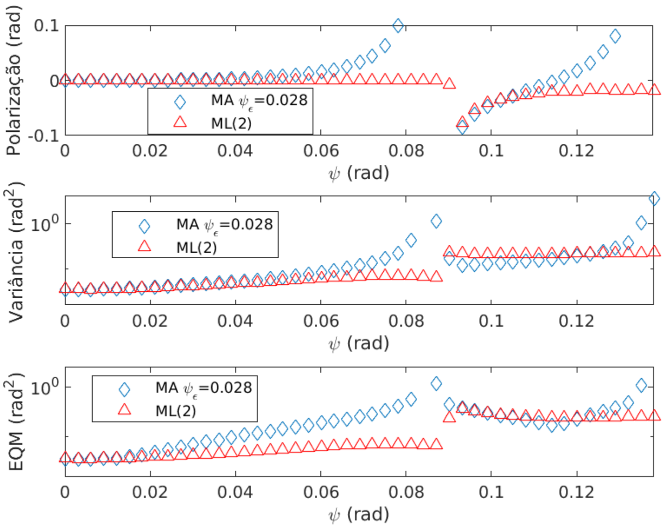

However, this study found that the increase in the number of used conformations reduces the intensity of this problem. The results below illustrate this finding.

Fig. 10 - Example of an objective function used by the ML(2) estimator, obtained with a 0.10-rad target azimuth and a 20-dB SNR.

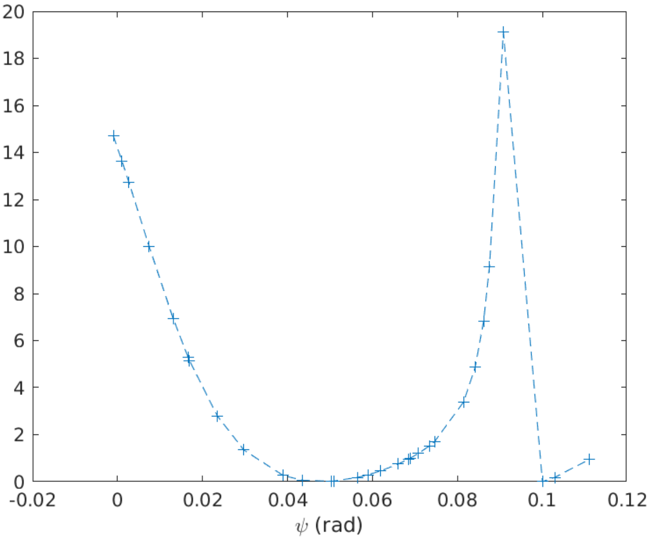

5.2 Increase in the number of formations

To implement the ML(3) estimator, a conformation with a $\psi_{\hat{o}} = 0$ rad slope and two conformations with $\psi_{\pm\hat{o}} = \pm 0,056$ Rad slopes were used. The used conformations with the ML(2) were the same as those above.

The Figure 11 shows the performance results obtained with these estimators for an SNR of 10 dB.

Fig. 11 - Performance of the ML(2) and ML(3) estimators as a function of the target azimuth with a 10-dB SNR.

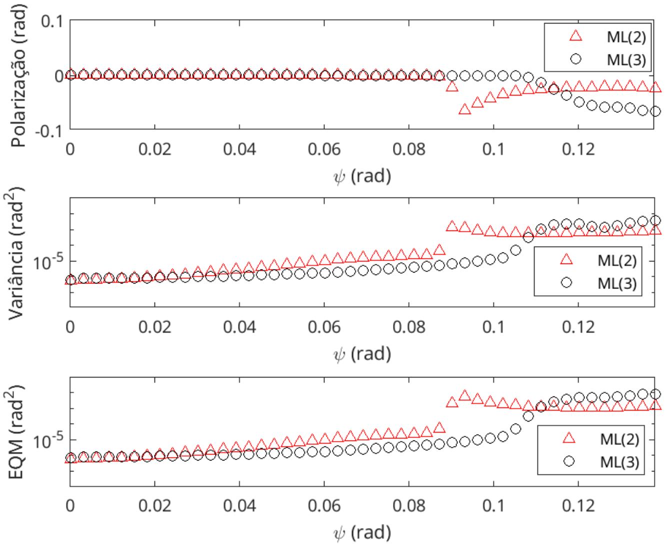

The use of three conformations can improve estimation *coverage*, providing an MSE that remains fundamentally stable up to azimuth values of the order of 0.105 rad, which represents an increase of about 20% over the *coverage* of the ML estimator(2).

Figure 12 shows the performance results of the same estimators obtained with a 20-dB SNR. This figure shows an improvement due to the increase in the SNR and that the ML(3) estimator increases coverage by around 20%.

Other simulations show ML estimations can obtain even greater gains of *coverage* if combined with the use of more than three conformations.

Fig. 12 - Performance of the ML(2) and ML(3) estimators as a function of the target azimuth with a 20-dB SNR.

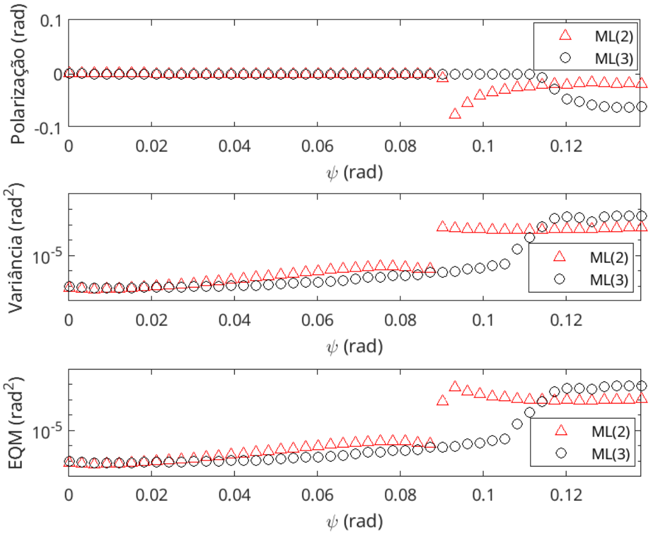

5.3 Computational complexity

The investigated ML estimators performed better than the MA estimator but have higher complexity, mainly due to the need to implement numerical optimization.

However, it should be noted that there remains room for research for algorithms for this implementation with reduced computational cost. This study implemented with APSO [22] but other alternatives exist and may be tried in future researches, for example, combining techniques — as suggested in [14] — or using approximate objective functions (in relation to the original objective function), reducing the computational costs of optimization.

Conclusions

This study investigated the use of maximum likelihood (ML) to estimate the azimuth of a target in radar systems with sensor array. The considered receiver model subjects the set of signals at the output of the array to fixed beam conformations, followed by filtering and sampling steps, to generate the vector of observations to estimate angles.

This study first evaluated an ML estimator that can produce delay parameters and obtain complex amplitude of the received signal. Then, it investigated the performance of a simplified version of this estimator, aimed only at obtaining the azimuth, using two beam conformations. Compared to the alternative, which uses the monopulse technique, the evaluated ML azimuth estimator provides accurate estimates at longer intervals but has a higher computational cost as it requires numerical optimization to obtain its estimates.

This research also evaluated the effect of a small increase in the number of input conformations in the ML to estimate the azimuth and found that an additional conformation improves the initially verified performance advantages.

Directions for the continuation of this investigation in future works were pointed out, especially aiming at reducing the computational complexity of ML estimators. Still in the perspective of continuing this research, it should be noted that, assuming the use of a two-dimensional array of sensors, the ML solution considered here can easily be extended to encompass the target elevation angle. The investigation of the performance of the position estimator thus obtained also offers an alternative for future studies.

References

[1] MAILLOUX, R. J. *Phased array antenna handbook*. [S. l.]: Artech House, 2017.

[2] RICHARDS, M.; SCHEER, J.; HOML, W. *Principles of Modern Radar: Basic Principles.* London: Institution of Engineering and Technology, 2010.

[3] XU, J.; WANG, W. Q.; GUI, R. Computational Efficient DOA, DOD, and Doppler Estimation Algorithm for MIMO Radar. *IEEE Signal Processing Letters*, [*s. l.*], v. 26, n. 1, p. 44-48, 2019.

[4] CHAHROUR, H.; DANSEREAU, R.; RAJAN, S.; BALAJI, B. Direction of Arrival Estimation using Riemannian Mean and Distance. *IEEE Radar Conference*, Boston, p. *1-5, 2019*1-5, 2019.

[5] SHERMAN, S.; BARTON, D. *Monopulse Radar Theory and Practice*. [S. l.]: Artech House, 2011.

[6] JAIN, V.; EHRMAN, L. M.; BLAIR, W. D. Estimating the DOA mean and variance of off-boresight targets using monopulse radar. *IEEE Proceeding of the Thirty-Eighth Southeastern Symposium on System Theory*, [*s. l.*], p. 85-88, 2006.

[7] SHARENSON, S. Angle estimation accuracy with a monopulse radar in the search mode. *IRE Transactions on Aerospace and Navigational Electronics*, [*s. l.*], n. 3, p. 175-179, 1962.

[8] GROSSI, E.; LOPS, M.; VENTURINO, L. A search-and-revisit scanning policy to improve the detection rate in agile-beam radars. *IEEE Workshop on Statistical Signal Processing (SSP)*, [*s. l.*], p. 452-455, 2014.

[9] GORWARA, A.; MOLCHANOV, P. Multibeam monopulse radar for airborne sense and avoid system. *SPIE Unmanned/Unattended Sensors and Sensor Networks XII*, [*s. l.*], v. 9986, p. 9-22, 2016.

[10] DAI, H.; HAN, H.; WANG, J.; XU, X.; QIAO, H. An improved high angular resolution method by using four--channel jointed monopulse radar. *In*: IEEE Progress Electromagnetics Research Symposium-Spring (PIERS), [*s. l.*], p. 3056-3061, 2017.

[11] TREES, H. V. *Optimum Array Processing*: Part IV of Detection, Estimation, and Modulation Theory. London: Wiley, 2004.

[12] CHANG, D.; ZHENG, B. Adaptive generalized sidelobe canceler beamforming with time-varying direction-of--arrival estimation for arrayed sensors. *IEEE Sensors Journal*, [*s. l.*], v. 20, n. 8, p. 4403-4412, 2019.

[13] DAVIS, R.; FANTE, R. A maximum-likelihood beamspace processor for improved search and track. *IEEE Transactions on Antennas and Propagation*, [*s. l.*], v. 49, n. 7, p. 1043-1053, 2001.

[14] Nickel, U. Overview of generalized monopulse estimation. *IEEE Aerospace and Electronic Systems Magazine*, [*s. l.*], v. 21, n. 6, p. 27-56, 2006.

[15] Trees, H. V. *Detection, estimation, and modulation theory, part I*: detection, estimation, and linear modulation theory. London: Wiley, 2004.

[16] ÖZSOY, V. S.; ÖRKCÜ, H. H.; BAL, H. Particle swarm optimization applied to parameter estimation of the four-parameter Burr III distribution. *Iranian Journal of Science and Technology, Transactions A: Science*, [*s. l.*], v. 42, n. 2, p. 895-909, 2018.

[17] POLI, R.; KENNEDY, J.; BLACKWELL, T. Particle swarm optimization. *Swarm Intelligence*, [*s. l.*], v. 1, n. 1, p. 33-57, 2007.

[18] NAJJARZADEH, M.; SADJEDI, H. *Implementation of particle swarm optimization algorithm for estimating the innovative parameters of a spike sequence from noisy samples via maximum likelihood method*. Digital Signal Processing. Amsterdam: Elsevier, 2020.

[19] GLASS, J. D.; BLAIR, W. Range estimation using adjacent matched filter samples. *IEEE Aerospace Conference*, [*s. l.*], p. 1-7, 2014.

[20] WANG, J.; WANG, T.; WU, J. Improved target direction-of-arrival estimation using multiple adjacent beams for airborne phased array scanning radar. *IET Radar, Sonar & Navigation*, [*s. l.*], v. 12, n. 2, p. 239-243, 2018.

[21] SCHWAAB, M.; BISCAIA JR, E. C.; MONTEIRO, J. L.; PINTO, J. C. Nonlinear parameter estimation through particle swarm optimization. *Chemical Engineering Science*, [*s. l.*], v. 63, n. 6, p. 1542-1552, 2008.

[22] YANG, X. S. *Particle swarm optimization*. Nature-Inspired Optimization Algorithms. [S. l.]: Academic Press, 2021.

[23] CLERC, M. *Beyond standard particle swarm optimization*. Innovations and Developments of Swarm Intelligence Applications. [*S. l.*]: IGI Global, 201

VOL.40 Nº2 2023
https://doi.org/10.22491/rmct.v40i2.11238.en

A review of materials to be used in stand alone ballistic plates as per the Joint Operational Requirements of the Ministry of Defense

Jeremias Fortini*[1], Frederico Dal Berto[2], Altair Soria Pereira[2], Eduardo Sousa Lima[1]
[1] Military Institute of Engineering (IME). Praça General Tibúrcio, 80, 22290-270. Paia Vermelha, Rio de Janeiro, RJ, Brasil.
[2] Institute of Physics and School of Engineering, Federal University of Rio Grande do Sul (UFRGS). Avenida Bento Gonçalves, 9500, 91501-970, Agronomia, Porto Alegre, RS, Brasil.
***fortini@ime.eb.br**

ABSTRACT: The development of ballistic materials resistant to new threats is a topic of great concern on the global stage. In 2018, the Ministry of Defense established the Joint Operational Requirements (JOR) for the Armed Forces' ballistic protection materials. Until now, the Defense Industrial Base has not presented a ballistic solution for some of the calibers surveyed. In this scenario, equipment has been chosen that allow greater mobility for the user combined with protection against calibers with greater kinetic energy. Thus, this article aims to present a review of materials to compose a Multilayered Armor System (MAS) for stand alone plates for assault vests, in addition to presenting the standards and conditions for evaluating ballistic materials adopted in the domestic and international context.

KEYWORDS: Ballistic plate. Stand alone. MAS. Joint Operational Requirements (JOR).

RESUMO: O desenvolvimento de materiais balísticos resistentes a novas ameaças é um tema de grande preocupação no cenário global. Em 2018, o Ministério da Defesa estabeleceu os Requisitos Operacionais Conjuntos (ROC) para os materiais de proteção balística das Forças Armadas. A Base Industrial de Defesa não apresentou, até o momento, solução balística para alguns dos calibres levantados. Neste cenário, tem-se optado por equipamentos que permitam uma maior mobilidade ao usuário, aliada à proteção contra calibres de maior energia cinética. Assim, o presente artigo tem por finalidade apresentar uma revisão sobre materiais para comporem um Sistema de Blindagem de Multicamadas (SBM) para placas do tipo stand alone para coletes de assalto, além de apresentar as normas e condições para avaliação de materiais balísticos adotadas em âmbito interno e internacionalmente.

PALAVRAS-CHAVE: Placa balística. Stand alone. SBM. Requisitos Operacionais Conjuntos (ROC).

1. Introduction

The evolution of humanity can be described through the battles fought by its various civilizations, in which scientific and technological advances played a fundamental role in determining the winners. The Persians were the first people to be concerned with personal protection, and began to use straw vests [1]. Over the centuries, there has been great evolution in these devices, which are currently represented as ballistic protection vests and helmets, known as personal ballistic protective clothing [2]. Those pieces of equipment can be made from various types of raw materials, such as metals, polymers, ceramics, composite materials, including those formed by natural fibers, which, through their combinations, generate products that can be represented in four main assessment parameters: protection level, useful life, weight, and cost [3].

Metallic materials were the precursors in personal armor, and copper alloys were replaced by ferrous materials, but the high specific weight of these materials ended up being an obstacle to keeping on being applied in personal armor. Currently, metallic materials are used in solutions where weight is not a determining factor in their use. An example to mention is their application in combat vehicles, armored vehicles, ships and military aircraft, where there is impact resistance, tensile strength, ductility, and hardness [4-5].

Polymeric materials revolutionized personal ballistic protective equipment through the development of Kevlar® in the 1970s, a synthetic para-aramid fiber with a complex molecular structure that has low density and specific resistance, higher than steel [6]. Ultra-high molecular weight polyethylene (UHMWPE)

Ceramics are extremely hard and resistant to compression and wear. When used in ballistic materials, they are applied to the outermost protection layer, as their high hardness allows projectile erosion and shattering, increasing the impacted area between projectiles and armor and dissipating the impact load. Furthermore, the broken ceramic causes mutual erosion with the projectiles, producing lateral forces that impact the flow and prevent greater penetration [7]. The most used ceramic materials in personal ballistic armor are alumina (Al_2O_3), boron carbide (B_4C), silicon carbide (SiC), and silicon nitride (Si_3N_4), which have a wide variation in their properties and processing costs [8-9]. Ceramic materials can be applied in conjunction with materials with greater ductility, such as aramid fiber sheets (Kevlar, for instance) or UHMWPE sheets[10], forming a Multilayered Armor System (MAS). Fibers and polymers have greater toughness, specific strength, specific modulus, fatigue resistance, wear resistance and shock absorption compared to ceramics, and when used as material on the back of ceramic plates, they act together, slowing down the ceramic material traction, serving as a support for the shrapnel and allowing greater kinetic energy loss [11].

Many countries have their own standards for classification of ballistic protection levels and performance of ballistic tests. The standards that are most recognized in this scenario are from the USA National Institute of Justice (NIJ). These standards, however, are directed at ballistic materials to be used by Public and Private Security Agencies, and do not cover possible threats in which the Armed Forces can be used in various theater of operations, and the different USA Armed Forces have their own specific standards [12]. Until 2018, the Brazilian Armed Forces used only NIJ standards to define the protection levels to be adopted. Nevertheless, through Normative Ordinance No. 14/MD, of March 23, 2018, the Joint Operational Requirements (ROC) [13] were defined for the ballistic materials to be adopted by the three forces (Army, Navy and Air Force) [14].

Considering the new requirements and the new strategic demands – Joint Operational Requirements (ROC) – established by the Ministry of Defense, which provide for the adoption of ballistic vests resistant to calibers 5.56 x 45 mm (M855/SS109) and 7.62 x 39 mm MSC (mild steel core) (M43) [13], with defined dimensions and weight, this review aims to present potential materials for application in an MAS ballistic solution, so that such materials can be used as stand alone plates in assault vests. Stand alone plates are integral pieces of 250 x 300 mm that, without the combination of any other type of protection, offer ballistic protection at the desired level. An MAS solution for composing these plates consists of the first layer of ceramic material and the second layer based on polymeric material. Within this scope of materials, several candidate materials for this composition will be presented.

2. Personal ballistic protection

2.1 Evolution

Over the centuries, wars have been decisive for the expansion or extinction of countless nations, and they are directly responsible for the evolution of humanity in various fields, especially in scientific discoveries [15].

With the evolution of battle scenarios, humankind felt the need to increasingly improve its protection. The Persians then developed straw vests, which served as protection against arrows and impact. These devices were improved by the Greeks and Romans, who used copper and bronze, as seen in **Figure 1** [16].

Fig. 1 - Roman armor.

Source: [16].

The first version of ballistic protection equipment, which resembles current models and provides mobility to the user, dates back to the 18th century in Korea, where a garment was developed using layers of cotton in sufficient quantity to protect against firearms of the time, as seen in **Figure 2** [17]. In Japan, garments were produced with thirty layers of silk that provided protection against projectiles fired by weapons that used black powder as a propellant [1]. In the 19th century, vests made from metal materials were developed, but they were still very heavy, hindering the user's mobility [18-19].

In 1902, in Chicago, United States of America, a garment was developed consisting of a mixture of 1.6 mm metal sheets between four layers of silk. This device weighed less than one kilogram and provided protection for .44 caliber [18]. This product became a success for the time; however, the heat and high cost, due to the amount of silk applied, caused the US Army to disapprove such equipment for use by its troops [19].

Fig - 18th century Korean ballistic protection.

Source: [17].

In 1902, in Chicago, United States of America, a garment was developed consisting of a mixture of 1.6 mm metal sheets between four layers of silk. This device weighed less than one kilogram and provided protection for .44 caliber [18]. This product became a success for the time; however, the heat and high cost, due to the amount of silk applied, caused the US Army to disapprove such equipment for use by its troops [19].

In the First World War, the Americans equipped their soldiers with a combined piece that covered the torso and head, the Brewster Body Shield. It was a piece of equipment built on the basis of a metal alloy of chromium and nickel, which provided protection against rifle shots, but weighed about twenty kilograms [19].

In 1918, the first piece of news of the application of ceramic materials for ballistic purposes was released, different from all the models developed to date, which were composed of metals or natural fibers as fabrics. English major Neville Monroe Hopkins discovered that applying a thin layer of enamel to the surface of rolled steel increased the ballistic plates resistance to penetration [20].

During World War II, bomber crews wore a vest that protected the entire torso and seat of the soldiers (Figure 3) [21].

Fig. 3 - Model of ballistic vest and helmet used by bomber crews.

Source: [21].

American soldiers who were sent to the Korean and Vietnam wars used flak jackets, which were padded jackets made of fiberglass sheets, nylon and aluminum, and intended to protect soldiers from grenade shrapnel. Nonetheless, their low effectiveness and heavy weight made this equipment inviable to be used after the creation of lighter and more efficient materials, such as Kevlar [1, 22].

The Americans were the pioneers in the use of ballistic protection for police forces. The increase in cases of homicides of security agents in the 1960s motivated the United States government, through the NIJ, to develop a ballistic protection vest for police use. The NIJ has since become the world reference body for classification of ballistic protection levels, as well as testing and normative instructions on ballistic vests and personal armor [1, 22].

In the 1960s, artificial aramid fibers for ballistic applications emerged, which were responsible for the revolution in protective equipment. At that time, DuPont®, the North American company, developed Nomex® to replace metal in racing car tires and then Kevlar®, which came onto the market in 1970, which is the most widely used synthetic fiber in ballistic protection to this day [23]. Aramid combines strength, low specific mass and flexibility, which enabled unprecedented advances in the production of modern ballistic vests [24].

In the 1970s, ceramic materials were developed for ballistic protection with the aim of reducing the weight of personal and aircraft armor (**Figure 4**) [25]. At that time, ballistic plates based on Al_2O_3, and B_4C were developed, obtained by hot pressing and liquid phase sintering [26].

Fig. 4 - Ballistic vests with ceramic material inserts used by the Americans in the Vietnam War.

Source: [25].

In the 1980s, larger ceramic plates were developed for use in vehicle protection. In this decade, the Personnel Armor System for Ground Troops (PASGT) was developed by the US Army, which was an important ballistic protection system used by the Americans in the 1980s and 1990s [27] (Figure 5) [28].

Fig. 5 - PASGT ballistic vest.

Source: [28].

Current vest models, through improvements in their raw materials, adapt to the mission for which the soldier will be deployed, and can offer a larger or smaller coverage area and higher or lower protection levels, always in contrast with the mobility required in combat, since the larger the area covered and the protection level, the lower the soldier mobility. In this sense, the materials used by bomb disposal agents protect the entire body (**Figure 6**) [30], while special forces operators adopt assault vests, which only have high-level inserts for frontal and dorsal ballistic protection [29].

Fig. 6 - Bomb suit.

Source: [30].

In this context, the US Army uses the concept of a modular vest called Improved Outer Tactical Vest (IOTV), and accessories can be added to or removed from which depending on the type of operation (**Figure 7**) [27, 31]. For missions that require maximum mobility, the Soldier Plate Carrier System (SPCS) is used (**Figure 8**) [32], which was designed to reduce the weight carried by soldiers on specific missions [27].

Fig. 7 - American modular IPTV vest.

Source: [31].

Fig. 8 - American assault SPCS vest.

Source: [32].

2.2 National ballistic vest

The ballistic vest model adopted since 2004 by the Brazilian Army (EB) and other Brazilian Armed Forces is the Outer Tactical Vest (OTV), which is the model prior to the IOTV adopted by North American troops, which was developed in the 2000s by the Americans to replace the PASGT [33].

The vest adopted by the EB has a front opening system, as shown in **Figure 9**, and is composed of a cover, a left front ballistic panel, a right front ballistic panel, a dorsal ballistic panel, a frontal ballistic plate, and a dorsal ballistic plate. The vest may also include accessories, neck protector (or collar), pelvic protector, glute protector, and shoulder protectors.

Fig. 9 - Front (e) and dorsal (d) image of the vest adopted by the EB.

3. Standards for classification and performance of ballistic tests

The protection specified for the EB vest is NIJ 0101.04 level III [34], obtained through the joint action of the ballistic panels and plates, while the ballistic panels alone provide level III-A protection, and using ballistic plates with no use of the panels is not allowed. The ballistic panels (flexible) are inserted into internal pockets of the cover, while the plates (rigid) are inserted into the external pockets of the vest cover.

The stand alone plates (**Figure 10**) [36] can be used in assault vests (**Figure 8**), which are equipment in which the ratio between coverage area and mobility is reduced, but, on the other hand, higher protection levels are sought for the covered region. This type of vest is called a Plate Carrier [35]. This format is widely used by troops who are deployed in actions involving imminent confrontation with the enemy, such as Special Forces troops on assault and rescue missions.

Fig. 10 - Stand alone ballistic plate.

Source: [36].

The definition of the characteristics of the equipment adopted by the EB personnel must follow the requirements established by the General Management Bodies (ODG) in consultation and coordination with the Sector Management Bodies (ODS) and the Operational Management Body (ODOp).

The ballistic vest is considered a Military Employment Material (MEM), and thus it must comply with the provisions of the Life Cycle of Military Employment Systems and Materials (SMEM), regulated by the Ordinance of the Army Commander No. 233, of March 15, 2016, which approved the General Instructions for the Management of the Life Cycle of Military Employment Systems and Materials (EB10-IG-01.018), 1st Edition, 2016. The process of developing a new material focuses on the first and second phases of the four phases provided for in the MEM Life Cycle, which are [37]:

- 1st phase: conceptual formulation;
- 2nd phase: acquisition;
- 3rd phase: production, use and maintenance;
- 4th phase: deactivation.

Table 1 summarizes the main documents provided for in EB10-IG-01.018 for the first phase of the SMEM Life Cycle [37].

Tab. 1 - Documents prepared in the conceptual formulation phase

Phase	Document	Purpose	Body in charge
Conceptual formulation	Understanding of Operations (COMOP)	Document containing information necessary to guide the integrated SMEM design, such as: mission, operational environment, types of operations, functionalities to be performed, and intentions (expected performance).	Army General Staff (EME)
	Doctrinal and Operational Conditions (CONDOP)	Document containing the parameters that define the use and expected performance of a given MEM, considering the Land Military Doctrine. This document constitutes the basis for the preparation of the Operational Requirements (RO)	Army Doctrine Center (C Dout Ex/ COTER)

Phase	Document	Purpose	Body in charge
Conceptual formulation	Operational Requirements (RO)	Document that follows the doctrinal and operational conditions in the process of obtaining a MEM, which embodies its characteristics restricted to operational aspects.	4th deputy chief office of the EME
	Technical, Logistical and Industrial Requirements (RTLI)	Document based on the RO and that consists of establishing the technical, logistical, and industrial characteristics that the system or material must have to meet the operational requirements.	Department of Science and Technology (DCT) and Logistics Command (COLOG)
	Technology Mapping (MAPATEC)	Document that indicates the technologies necessary to obtain a system or material through R&D&I, as well as the flow to obtain them, in chronological order.	DCT

Source: [37].

After preparing all the documentation mentioned in **Table 1**, the EME summons the ODS to hold the First Decision-Making Meeting (1st RD) that will determine whether or not to continue the life cycle for the acquisition phase, which will begin with the order issued at the 1st RD, so that the SMEM can be acquired, through Research, Development and Innovation (R&D&I) and/or acquisition projects, after their inclusion in the EB's project portfolio [37].

In the case of acquisition through R&D&I, the aim is to obtain a prototype and, subsequently, the pilot batch of the system or material with the desired technical and operational characteristics, through the following steps:

a. acquisition of the prototype;
b. evaluation of the prototype;
c. production of the pilot batch; and
d. evaluation of the pilot batch.

The SMEM can be acquired on the domestic or foreign market to meet the needs identified, with a specific assessment being planned, in which there is verification of the conformity of the system or material to be acquired with the standards and technical, operational, and logistical requirements established by the EB during the 1st RD.

Once the acquisition phase is completed, whether by R&D&I and/or acquisition project, and the conformity of the assessed system or material is confirmed, the Second Decision-Making Meeting (2nd RD) is held, which concludes this phase, determining whether or not to carry out the doctrinal experimentation for the system or material, as well as its adoption and continuation to the production, use, and maintenance phase [37].

In short, for the development of a new product, several Army bodies are mobilized, jointly generating the documents listed in **Table 1**. Among the listed documents, the RO stands out, as it is in this document that the general product characteristics will be defined, such as in the case of ballistic vests – model, shape, size, weight, protection levels, among other items –, so that, basically, the RTLI can determine the conditions for evaluating the requirements established [37].

For the ballistic protection vest, the following documents were prepared as provided for in EB10-IG-01.018 [37]:

a. COMOP No. 03/2018, of the Brazilian Combatant System (COBRA), published by Ordinance No. 156-EME, of August 13, 2018;
b. CONDOP No. 017/2018, of the Brazilian Combatant System (COBRA), published by Ordinance No. 090, of August 20, 2018;
c. RO No. 32/2019 – tactical ballistic vest, published by Ordinance No. 054-EME, of March 13, 2019;
d. RTLI of the tactical ballistic vest, published by Ordinance No. 088-EME, of March 27, 2019;
e. MAPATEC of the tactical ballistic vest, a DCT's internal document.

In addition to the documents listed above, when a product is common to the three Armed Forces, the Ministry of Defense may issue documentation for standardization of requirements, the Joint Operational Requirements (ROC). By means of Normative Ordinance No. 14/MD, of March 23, 2018, the ROC were defined for, among other materials, bulletproof vests and stand alone ballistic plates. Therefore, the RO published in 2019 have practically the same parameters raised by the 2018 ROC, with the exception that, for the stand alone plate, there is only the ROC to date [13].

The requirements established for the bulletproof vest and plate in the RO and/or ROC are divided into Absolute Requirements, which are those that a given MEM must have, and Desirable Requirements, which are those that may or may not be requested from manufacturers, according to the demander's request at the time of acquisition. The Absolute Requirements for stand alone vests and plates include the following calibers for ballistic protection [13]:

a. .44 Magnum SJSP;
b. 9 x 19 mm Luger;
c. 5.56 x 45mm (M193) (lead core);
d. 7.62 x 39mm (M193) (lead core);
e. 7.62 x 51mm FMJ (M80).

These calibers correspond to NIJ 0101.06 level III [38] or NIJ 0123.00 RF1 [39], as will be seen in section 3.

The calibers requested in the Desirable Requirements for vests and plates, which correspond to NIJ 0123.00 RF2 are as follows [13]:

a. 7.62 x 39 mm MSC (M43);
b. 5.56 x 45mm (M855/ SS109);
c. 7.62 x 51 mm AP.

These calibers correspond, respectively, to the special levels of NIJ 0101.06, known in the market as "III+" and "III++," the latter being equivalent to NIJ 0101.06 level IV [38].

Therefore, as a result of the demand by the Ministry of Defense and corroborated by the EB, according to the ROC and RO, respectively, it is important to delve into studies that present the possibility of a ballistic manufacturing solution that meets the requirements established.

It is therefore worth noting that there is no nationally manufactured product that meets such desirable requirements. These calibers are considered important threats in the theater of operations where the EB is used. The 7.62 x 39 mm MSC (M43) cartridge is used by the AK47 assault rifle, and the 5.56 x 45 mm SS109 can be used by the EB's own weapon, the 5.56 IA2 Assault Rifle, which was adopted in 2013 by Ordinance No. 211-EME, of October 23, 2013 [40].

This follows the Controlled Products Regulation, approved by Decree No. 10,030, of September 30, 2019 [41] and by Ordinance No. 18 – D LOG, of December 19, 2006, which approves the Regulatory Standards for the technical assessment, manufacture, acquisition, imports, and destruction of ballistic materials [43]. According to these documents, the protection levels adopted in Brazil follow those described in NIJ 0101.04 [34], shown in **Table 2**, in which levels I to III-A can be sold for general use, while levels III and IV can only be sold to the Armed Forces and other Public Security Agencies duly authorized by the Army Command, and are considered restricted (RTO).

In Article 8 of Ordinance 18 [43], it is determined that ballistic vests developed in Brazil must be assessed at the Army Evaluation Center (CAEx) based on the NIJ 0101.04 [34] standard. Article 12, in turn, establishes that ballistic plates, designed to provide the desired protection level, may be tested and sold if they meet the minimum dimensions provided for in NIJ 0101.04 [34].

For protection against level I to III-A calibers, there is no need to use ballistic plates, as correctly sized ballistic panels offer ballistic protection to the user. On the other hand, for protection against level III and IV calibers, it is necessary to use ballistic plates acting alone or in conjunction with ballistic panels.

Tab. 2 - Protection levels established in NIJ 0101.04

Level	Ammunition	Velocity (m/s)	Projectile mass	Degree of restriction
I	.22 caliber LR LRN	329	2.6 g 40 gr	ALLOWED
	.380 ACP FMJ RN	322	6.2 g 95 gr	
II-A	9mm FMJ RN	341	8 g 124 gr	
	40 S&W FMJ	322	11.7 g 180 gr	
II	9mm FMJ RN	367	8 g 124 gr	
	.357 Magnum JSP	436	10.2 g 158 gr	
III-A	9mm FMJ RN	436	8.2 g 124 gr	
	.44 Magnum SWC Lead	436	15.6 g 240 gr	
III	7.62x51mm – NATO FMJ	847	9.6 g 148 gr	RTO
IV	.30 Caliber M2 AP	878	10.8 g 166 gr	

Source: [34]

The assessment of ballistic levels performed in accordance with NIJ 0101.04 consists of impacting the ballistic material to be tested using ammunition of the intended level, loaded with a quantity of gunpowder that meets the velocity specified in the standard. The projectile mass is presented in grams, a unit of the International System (IS), and in grains (gr), which is the unit usually used in reloading scales, with the projectiles generally measured in increments of 1 gr, and the gunpowder charges measured in increments of 0.1 gr [34].

The ammunition used is not found on the market in the test configuration, since in this case the specific tips (projectiles) are used, according to the caliber, with manual (Figure 11) or automated loading of the case with the quantity of gunpowder necessary to reach the test velocity.

Before the ballistic test starts, it is necessary to correctly calibrate the amount of gunpowder to be used in the test, so that those impacts in which the velocity is outside the velocity tolerance are invalidated. The velocity is measured by means of two optical sensors installed along the trajectory and separated from each other by distance C, as shown in **Figure 12**.

The vest component to be tested will be fixed vertically by elastic bands on the support material (BMF - Backing Material Fixture), which has density similar to that of the human body, and aims to simulate the impact that the human body would suffer if it were shot under the test conditions.

Fig. 11 - Manual loading equipment.

The support material specified by NIJ 0101.04 is modelling clay, called plastilina. NIJ determines that ROMA® plastilina No. 1 should be used. Its density is rigorously tested before, during, and after the tests [34].

After the ammunition is fired by the test weapon and the projectile impact, the ballistic vest is analyzed and results classified as *complete penetration*, in which the projectile passes through the tested material, making it possible to verify the presence of ammunition fragments in the support material, or as *partial penetration*, in which the projectile only deforms the tested material, without passing through it [34].

For results classified as partial penetration, the deformation caused by the ballistic impact is measured by means of the plastilina indent (trauma). For approval, NIJ 0101.04 establishes 44 mm of trauma as the maximum deformation in the material [34]. In **Figure 13**, it is possible to observe the indent on the support material [34].

Fig. 12 - Ballistic test setup as per the NIJ.

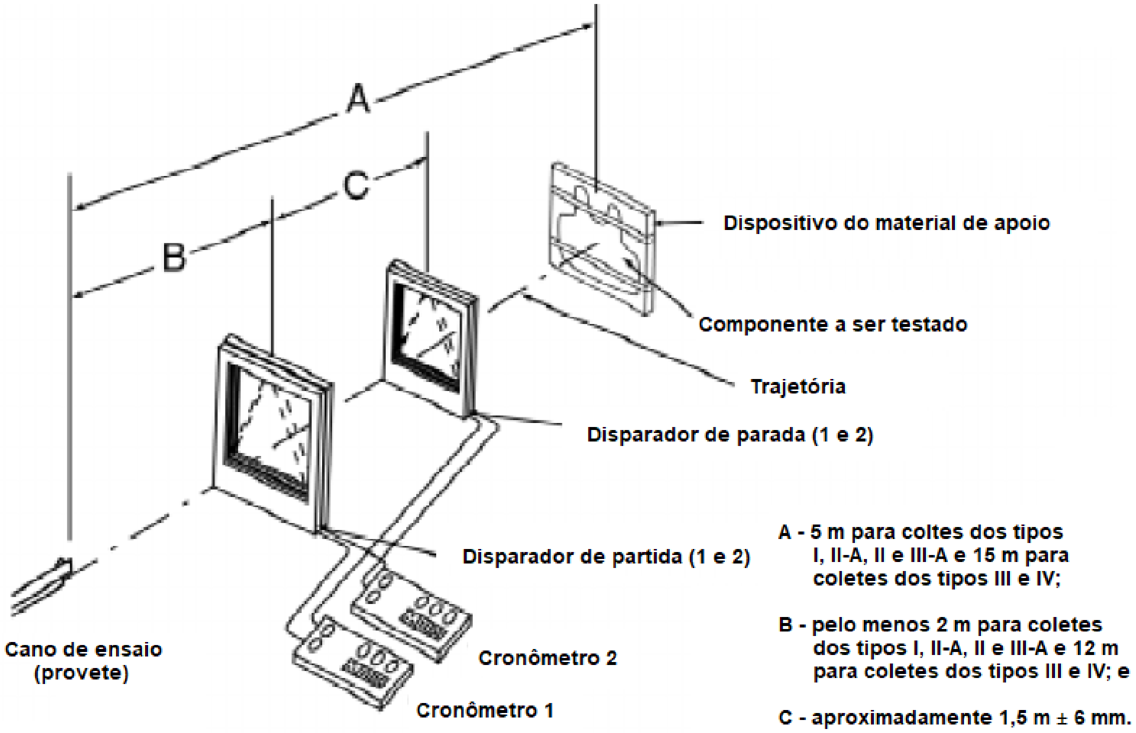

Source: [34].

Fig. 13 - Verification of ballistic performance by measuring trauma on the support material (plastilina).

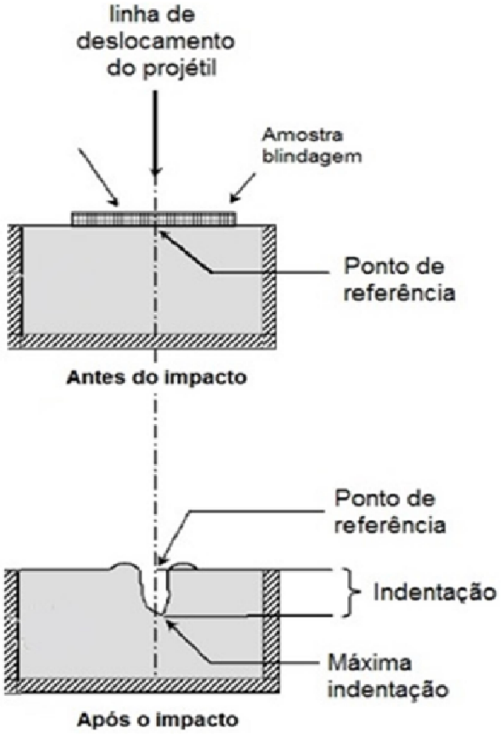

Source: [34].

It is worth noting that, although NIJ 0101.04 is still in force, several countries use the most recent version to assess the ballistic resistance of bulletproof vests, which is NIJ 0101.06, in force since June 2008 [38].

Both the protection levels and the assessment mechanisms of NIJ 0101.04 [34] and NIJ 0101.06 [38] are similar. As for the protection levels, in NIJ 0101.06 [38] level I was discarded. The other levels remained with the same calibers, but the test velocity for some of them was changed in order to ensure greater safety for the user (Table 3).

An important addition to NIJ 0101.06 [38] was the provision for testing with calibers other than those specified in the standard, determining them as “special level.” With the modernization of weapons used in recent years, there was a need to test ballistic materials for new threats. As example, it is possible to mention the calibers that are the subject of this article, classified as NIJ 0101.06 levels “III+” (7.62 × 39 mm MSC) and “III++” (5.56 × 45 M855/SS109) [38] or NIJ 0123.00 RF2 [39].

Tab. 3 - Protection levels established in NIJ 0101.06

Level	Ammunition	Velocity (m/s)	Projectile mass	Degree of restriction
II-A	9mm FMJ RN	355	8 g 124 gr	ALLOWED
	40 S&W FMJ	325	11.7 g 180 gr	
II	9mm FMJ RN	379	8 g 124 gr	
	.357 Magnum JSP	408	10.2 g 158 gr	
III-A	.357 SIG FMJ RN	448	8.1 g 125 gr	
	.44 Magnum SJHP	408	15.6 g 240 gr	
III	7.62x51mm – NATO FMJ	847	9.6 g 148 gr	RTO
IV	.30 Caliber M2 AP	878	10.8 g 166 gr	

Source: [38].

Regarding assessment tests, the number of samples tested in NIJ 0101.06 is much higher than that of NIJ 0101.04. While four samples are required for assessing NIJ 0101.04 level III [34], 14 samples are required in NIJ 0101.06 [38].

Another situation not provided for in NIJ 0101.04 [34] is the testing of material submitted to adverse conditions of humidity, temperature, and mechanical damage. NIJ 0101.06 [38] requires that samples be submitted to a 10-day cycle inside a rotating drum, at a temperature of 70°C and relative humidity of 90%. Such equipment –Tumbler – can be seen in **Figure 14**.

In October 2023, NIJ 0101.07 was published, which uses NIJ 0123.00, also published in October 2023, to establish the new ballistic protection levels adopted by the NIJ. The NIJ 0123.00 levels are divided into ballistic protection for soft armor (NIJ HG1 and NIJ HG2) and ballistic protection for hard armor (NIJ RF1, NIJ RF2 and NIJ RF3), as can be seen in Table 4 [39].

Fig. 14 - Tumbler used in the assessment of ballistic vests according to NIJ 0101.06.

Source: [46].

Tab. 4 - Protection levels established in NIJ 0123.00 [39].

Level	Ammunition	Velocity (m/s)	Projectile mass	Degree of restriction
NIJ HG1	9mm FMJ RN	398	8 g 124 gr	**ALLOWED**
	.357 Magnum JSP	436	10.2 g 158 gr	
NIJ HG2	9mm FMJ RN	448	8 g 124 gr	
	.44 Magnum JHP	436	15.6 g 240 gr	
NIJ RF1	7.62x51mm – M80 NATO FMJ	847	9.6 g 148 gr	**RTO**
	7.62x39mm Surrogate	725	7.9 g 122 gr	
	5.56mm M193 BT	990	3.6 g 56 gr	
NIJ RF2	7.62x51mm – M80 NATO FMJ	847	9.6 g 148 gr	
	7.62x39mm Surrogate	725	7.9 g 122 gr	
	5.56mm M193 BT	990	3.6 g 56 gr	
	5.56mm M855 BT	950	4 g 62 gr	
NIJ RF3	.30 Caliber M2 AP FMJ	878	10.8 g 166 gr	

Source: [39].

As occurred in NIJ 0101.06 [38], in NIJ 0101.7 [39] there was a considerable increase in the number of samples for vest assessment. For NIJ RF 1, which is equivalent to NIJ 0101.06 level III [38], at least 39 samples are required, instead of the 14 samples for NIJ 0101.06 [38].

The ballistic limit is a parameter evaluated since NIJ 0101.04 [34] and remains in the NIJ standards until the most recent update. To evaluate this parameter, MIL STD 662F [44] is used as a supporting standard, using the V50 concept.

The test is performed by means of successive shots, increasing and decreasing the projectile velocity, depending on whether the material is penetrated or not, until the velocity known as the "ballistic limit" is determined, at which the probability of penetration by the new shot is 50%. This concept is widely used to differentiate ballistic materials of the same protection level, because the higher the ballistic limit of a given material, the more security it will be able to provide at high velocity, even above standardized test velocity.

In **Figure 15**, it is possible to observe the simulation of a ballistic limit test [44].

Fig - Test performance simulation to evaluate the ballistic limit of a material.

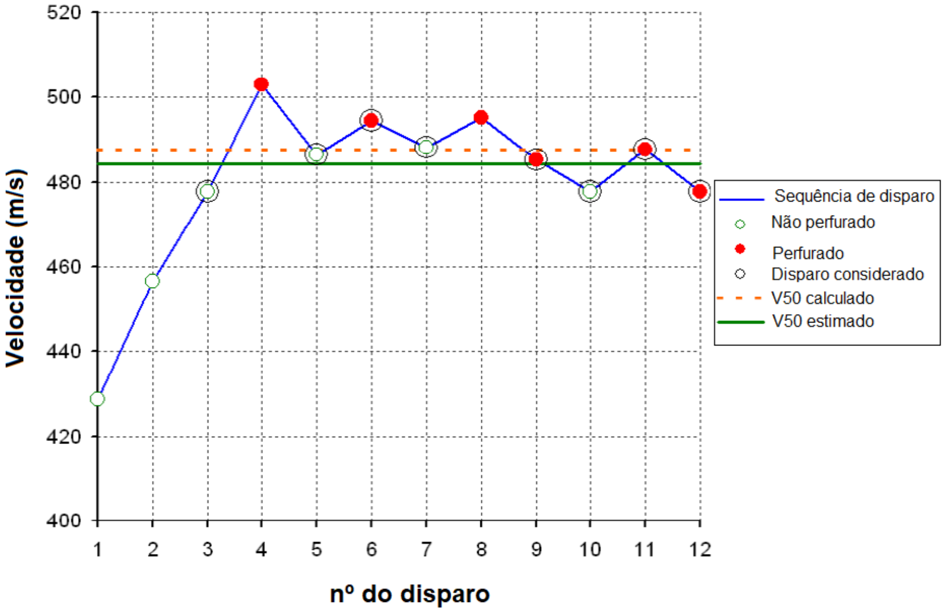

Source: [45].

4. High performance polymeric fibers for ballistic applications

Fibers and fabrics have been the main drivers of the most significant advances in personal armor over the past 20 years, largely due to improvements in the manufacturing processes of UHMWPE and aramid fibers [12].

High-performance ballistic fibers have specific properties that differentiate them from other man-made fibers used for industrial applications. The tensile strength and modulus of elasticity are higher and the elongation is lower than in traditional fibers [47].

Each high-performance ballistic fiber has properties related to the polymer and the spinning process used in its manufacture. The tensile strength of these fibers is determined by the structural characteristics, molecular orientation, cross-sectional area, and degree of linearity of the polymer chain. As with any high-technology product, such improvements result in increased production costs for the item, and the manufacturer must always achieve this balance to make the item competitive on the market [48]. **Figure 16** shows the correlation between the main mechanical properties of some fibers compared to steel.

Fig. 16 - Graph correlating the specific modulus of elasticity with the specific tensile strength limit of the main fibers on the market.

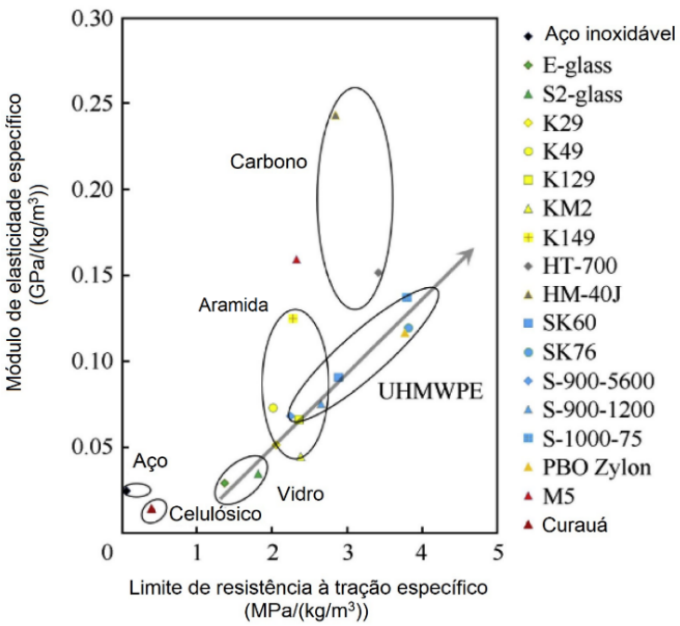

Source: [48].

Ballistic fibers can be used in three possible components of bulletproof vests: ballistic panels as fabrics, monolithic ballistic plates as polymers, and as components of an MAS. For these applications, both organic and inorganic fibers can be used.

DuPont® developed aramid fibers, whose chemical composition is polyparaphenylene terephthalamide (PPTA). These fibers were structured and transformed into threads and then woven, giving rise to the flexible fabric called Kevlar® [49]. Currently, there are several other companies that manufacture aramid-based fabrics; one of which is the Teijin Group® Company, which manufactures the aramid fabric registered as Twaron®.

Although the aramid does not have the highest tensile strength or the highest modulus of elasticity among high-performance fibers, it is characterized by a favorable relationship between its properties, such as low density, high tensile properties, high chemical resistance, high decomposition temperature (above 500°C), low flammability, and good thermal and dimensional stability [50].

Aramid fibers, in general, do not melt, since decomposition occurs at the same crystalline melting temperature (T_m). The major disadvantage of aramid fibers is their low resistance to moisture absorption. Therefore, when used, they must be packaged in such a way as to have the least possible contact with air [51].

UHMWPE was recently developed, and its main characteristics are low density and high tenacity. It is responsible for significantly reducing the weight of bulletproof vests, which can be used in both ballistic panels and monolithic ballistic plates or MAS. The best-known brands on the market are Dyneema®, from DSM, and Spectra®, from Honeywell [51].

UHMWPE is the least dense and most abrasion-resistant of all high-performance fibers. It is also more resistant to ultraviolet radiation and chemicals than aramid fibers. Studies indicate that UHMWPE fibers, after prolonged exposure to UV radiation, show tenacity loss and decreased elongation (due to the scission of the polymer chains), and at the same time increased modulus of elasticity (due to the cross-linking of the chains) [52].

Polybenzobisoxazole (PBO) was developed together with UHMWPE. PBO fibers are extremely strong, hard and rigid, and have a higher tensile strength and modulus of elasticity than polyaramid fibers or some UHMWPE fibers. They also have excellent chemical resistance to various organic solvents, acids and bases, but are easily degraded when exposed to UV radiation and to the combination of high temperature and humidity [53].

PBO fiber is commercially known as Zylon®. It is manufactured by Toyobo, the Japanese company [54]. Zylon® fabrics absorb almost twice the energy per unit of area density than Kevlar® and Spectra®, and almost 12 times more than aluminum. The ballistic impact performance of PBO systems is substantially superior to Kevlar® 29 systems, and marginally better than Kevlar® KM2 systems [54, 55].

However, the commercialization of vests containing Zylon® fiber suffered a serious impact after an event in 2003 in Forest Hills, Pennsylvania, USA, when a police officer wearing a bulletproof vest had his equipment perforated by a .40 caliber pistol shot, which, according to the material protection level, should not have been perforated, and he ended up seriously injured [56].

As a result, the NIJ carried out an extensive investigation of all bulletproof vests that used Zylon® in their composition, and in 2005 found that approximately 50% of these vests did not provide adequate protection for their users, concluding that Zylon® presented a systematic loss of tensile strength, tensile deformation and ballistic performance correlated with the breaking of specific bonds in the chemical structure of the material [56-57].

The company responsible for manufacturing the material and the companies that manufactured the vests were punished with significant fines, and the NIJ ended up banning the sale of vests with this composition [34, 48].

The M5®, which is a high-performance fiber based on polypyridobisimidazole (PIPD), was developed by Magellan Systems International (USA), which became part of DuPont® in 2005. This fiber demonstrates a very high specific energy absorption capacity at sonic velocity, and therefore has great potential for ballistic applications, as observed in **Figure 17**, when comparing its performance with other ballistic fibers [2, 58]. Although the literature shows a promising future for the M5®, there are no items on the market that contain this fiber in their composition.

The P 120 is a carbon fiber with a very high modulus of elasticity and has the highest deformation wave speed compared to other fibers. However, it is not a material that is suitable for ballistic applications due to its low energy absorption capacity [48].

Figure 17 shows the evolution of ballistic fibers over the years, considering the V50 ballistic performance of each.

Fig. 17 - Evolution of ballistic fibers according to V50 performance.

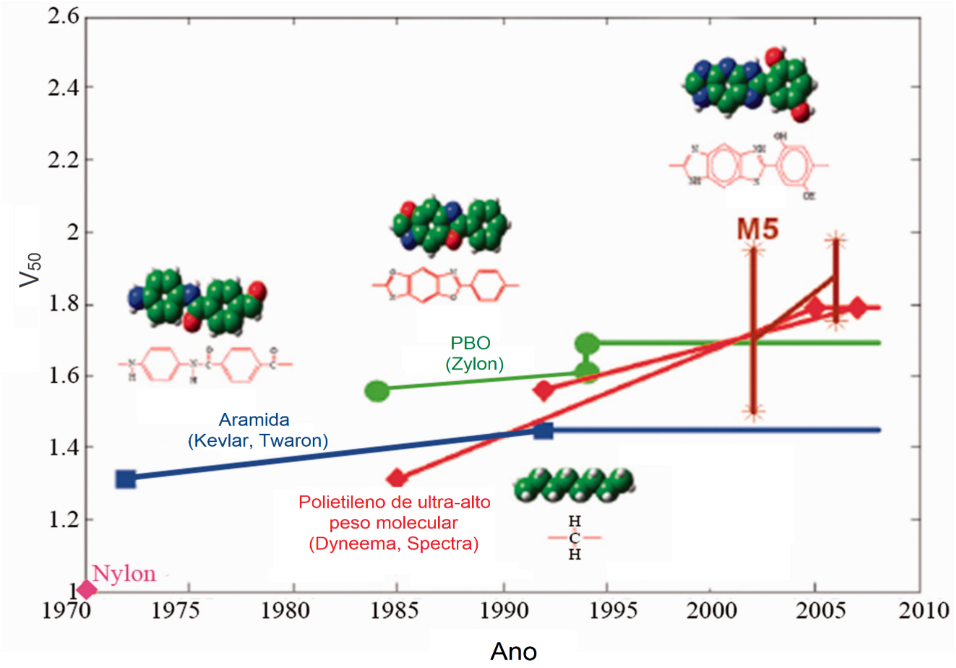

Source: [48].

In recent years, the search for environmentally sustainable products has led to research into natural fibers with ballistic applications gaining notoriety in the research of new ballistic materials. Several studies have been published on the application of natural fibers, mainly inserted as an MAS second layer, in which the natural fiber commonly makes up 30% of the volume of the epoxy or polyester matrix layer [59-61]. **Figure 18** shows the composition of the MAS with natural fibers.

Among the natural fibers under study, some of them can be listed, such as: bamboo, mallow, hemp, jute, sisal, ramie and *curauá*. Evidence of massive capture of larger fragments than when using Kevlar fibers was found in some cases, mainly in *Curauá* composites. Nucleation and propagation of cracks in the epoxy matrix were suggested to provide an additional mechanism of energy dissipation in favor of epoxy composites. In addition to being sustainable, these fibers have additional advantages of providing lighter and more cost-effective armor systems when compared to those made of aramid, which makes these fibers capable of competing with aramid in the MAS [48, 59].

Table 5 shows the main mechanical properties of some natural fibers compared to aramid fiber.

Fig. 18 - MAS composition with natural fibers

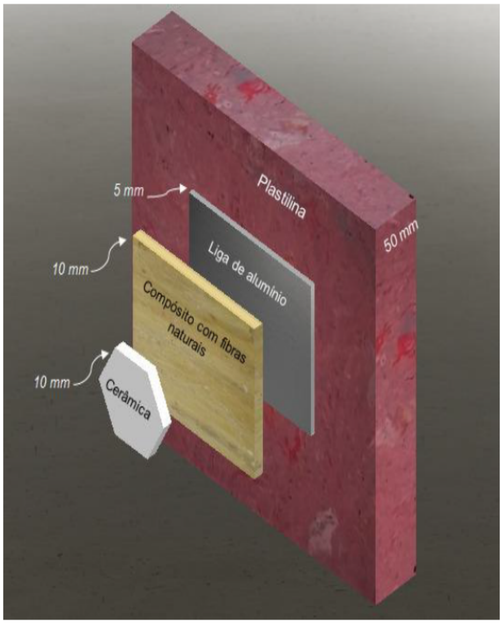

Source: [59].

Tab. 5 - Mechanical properties of some natural fibers compared to aramid fiber

Fiber	Specific Mass (ρ) (g/cm³)	Tensile strength limit (σ) (MPa)	Modulus of Elasticity (E) (GPa)	Max. (σ/ρ) (MPa.cm³/g)
Bamboo	1.03– 2.21	106- 204	-	198
Mallow	1.37– 1.41	160	17.4	117
Jute	1.30– 1.45	393- 800	13- 27	615
Hemp	1.07	389- 690	35	649
Sisal	1.26– 1.50	287- 913	9- 28	725
Ramie	1.5	400- 1620	61- 128	1,080
Curauá	0.57– 0.92	117- 3000	27- 80	2,193
Aramid	1.44	3000- 4100	63- 131	2,847

Source: [62- 63].

5. Ceramic materials for ballistic application

Ceramic materials are non-metallic inorganic materials that are characterized by being very hard and brittle. They are formed by predominantly covalent or ionic bonds between metallic and non-metallic elements. Their use as a final product is normally obtained through high-temperature heat treatment processes, called sintering [64].

Compared to metals, these materials have high moduli of elasticity and low densities, and are capable of withstanding extremely high temperatures, often above the melting point of most metals used in components. The main disadvantage of ceramic materials is their fragility. Even the smallest surface flaws (scratches or cuts) or internal flaws (inclusions, pores and microcracks) can have disastrous results [65].

Ceramic materials can be manufactured from natural or synthetic raw materials. The most commonly used natural materials in industry are: clay, kaolin, quartz, feldspar, phyllite, talc, graphite, and zirconite. Synthetic materials include, among others, Al_2O_3, SiC, Si_3N_4, ZrO_2 and B_4C [66-67]. **Table 6** presents the main mechanical properties of ceramic materials used in ballistic armor.

The action of ceramics in combined armor is effective because the projectile impact with the ceramic face creates compressive shock waves associated with high pressures, which pass through the projectile and the ceramic at the respective wave speeds. The waves interaction, after reflection, occurs inside the projectile and causes its fragmentation. In addition, when the projectile tip hits the target, a reduced region is submitted to high compression, with the appearance of a fracture cone [68-69].

The erosion of the projectile as it passes through the ceramic material, caused by the action of fragmented particles, is largely responsible for its energy loss. Therefore, it is essential that the ceramic face has a high hardness [68-69].

Excessive ceramic material porosity reduces the armor performance, due to the decrease in hardness and densification. Nonetheless, residual porosity can favor ballistic protection, since the pores constitute localized heating points [70], where part of the projectile kinetic energy is converted into thermal energy. The relationship between energy absorption and hardness, therefore, is important to determine the projectile tip breakage.

The main monolithic ceramic materials used in armor systems for personal and collective ballistic protection are: oxide ceramics, especially Al_2O_3; non-oxide ceramics based on nitrogen (nitrides); ceramics based on carbon (carbides), such as B_4C and SiC; or borides and their combinations, such as titanium diboride (TiB_2) [71-72].

Al_2O_3 shields are the ceramic materials most widely used for this purpose. They have adequate ballistic performance and low manufacturing costs. Al_2O_3-based ceramics are also widely used as transparent shields in the form of sapphire or polycrystalline aluminum oxynitrate (AlON), which are useful for vehicle windows and instrument viewing. This versatility and cost-effectiveness take place at the expense of high specific mass when compared to other ceramic shields [73].

Research and development of B_4C shields have shown that this material is very useful for the defense industry, presenting greater hardness and lower specific mass than Al_2O_3 [74].

B_4C armors are highly efficient for relatively low impact velocities. However, for armor-piercing projectiles with high kinetic energy, when the pressure generated by the interaction reaches the order of 20 GPa, the material ends up undergoing an amorphization process that causes a drop in ballistic performance [75]. The main disadvantage of B_4C armors is their high manufacturing cost [76].

On the other hand, SiC armors are less expensive to produce than B_4C, with slightly inferior mechanical properties [76]. Armors produced with this material are also indicated as substitutes for situations in which B_4C amorphization may occur [75].

Kaufmann et al. [77] evaluated the performance of SiC, B_4C and Al_2O_3 armors submitted to impacts from .50 armor-piercing ammunition by penetration depth. The work found that SiC presented the best performance and Al_2O_3 the worst. SiC, in many cases, presented behavior similar to that of B_4C.

The main disadvantage of ceramic armor is that, when impacted, they end up favoring the production of microcracks, which can extend to the impact region [78], causing material fragmentation and making such material vulnerable to resist new impacts.

The ballistic response of a ceramic material is associated with a series of factors, such as microstructure, chemical composition, phase formation, physical properties (density, hardness, Young's modulus, mechanical strength, fracture resistance, and sonic velocity), in addition to the efficiency in dissipating the energy of the ballistic impact. A single property does not define the material behavior, mainly because the fracture mechanism during the projectile impact is very complex, and the fractures are created by stress gradients that occur in a relatively short period. Only the combination of different properties enables satisfactory material performance. For a better analysis of the choice of armor, the association between these different conditions must be considered, together with the correct manufacturing process, which is essential for optimizing the properties of the finished ceramic material [8-9].

For example, hardness is vital for fracturing and eroding projectiles; fracture toughness and flexural strength help the ceramic resist multiple impacts; the modulus of elasticity is related to the propagation of the stress wave, and the fracture mode is related to the amount of energy absorbed by the ceramic. Thus, improvements in several properties are necessary so that their combination results in a more efficient ballistic ceramic [67].

The manufacturing process is very important in determining the final properties of the product. Generally, however, the processes that provide the best properties are the most expensive, as is the case of the hot pressing (HP) process for SiC ceramics, in which the properties often reach values close to the theoretically predicted limits for the materials, but are extremely expensive and limited in terms of part geometry [8-9].

Tab. 6 - Properties of the main advanced ceramics

	Specific Mass (g/cm^3)	Flexural Strength Limit (MPa)	Compressive Strength (MPa)	Modulus of Elasticity (GPa)	Fracture Toughness (MPa. m$^{1/2}$)
Al_2O_3	3.98	379	3,025	379	5.5
SiC	3.1	260- 612	3,860	414	4.4
Si_3N_4 (chemical reaction)	2.5	350	1,030	207	3.3
Si_3N_4 (hot pressed)	3.2	650	3,450	310	5.5
ZrO_2 (tenacification)	5.8	674	1,725	200	12.1
B_4C	2.5	235- 321	2,200	410- 425	4

Source: [76, 80].

6. MULTILAYERED ARMOR SYSTEM

Multilayered or mixed armor, previously known as MAS, consists of superimposing layers of different materials with the aim of taking advantage of the differences in their properties in order to ensure the best performance. The combination of these materials with distinct and complementary properties aims to prevent projectile penetration and reduce the trauma caused by the impact. **Figure 19** shows an illustration of an MAS under ballistic impact.

In the MAS, ceramic materials are used to resist the stresses arising from the initial events, serving as a first layer, in which the initial projectile impact occurs. Its function is to wear down the tip and dissipate part of the kinetic energy by fragmenting its mass, which ends up improving the distribution of the impact pressure on the second layer, as shown in section 6.

The second armor layer, in this multilayered system, is formed by ductile materials – metallic or polymeric – and has the function of absorbing the residual projectile kinetic energy, the shrapnel from both the ammunition and the ceramic itself through its plastic deformation. The materials most applied for this purpose are aramid, UHMWPE or natural fiber compounds in a polymer matrix, as shown in section 5.

Depending on the system, a third layer consisting of a ductile metal, usually an aluminum alloy, can be applied in order to absorb the residual energy through its plastic deformation [76].

Fig. 19 - Different stages associated with the impact between a projectile and a ceramic armor material: (a) shattering stage; (b) erosion stage; (c) catching stage.

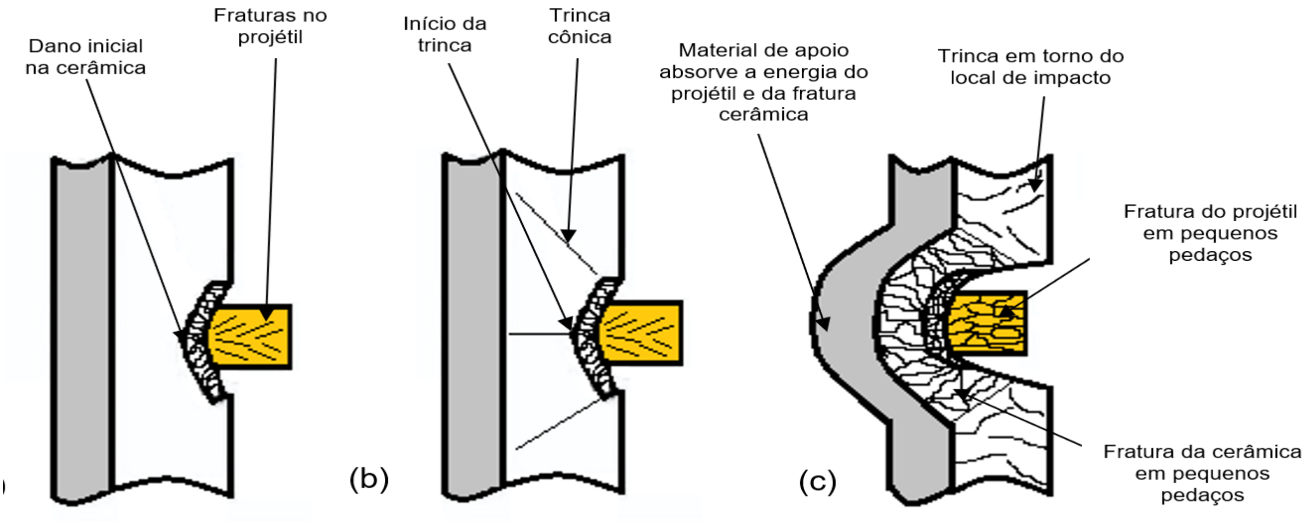

Source: [79].

7. Conclusion

Although some ballistic solutions for the calibers defined by the ROC are met in the foreign market, the national Defense Industrial Base (BID) currently has no approved materials that meet the demand presented by the Ministry of Defense. The Materials Engineering Section of the Military Institute of Engineering (IME) has numerous research projects in the area of personal armor, among other applications, with metallic, natural fiber composite, polymeric and, finally, ceramic materials.

The BID faces great difficulties in developing ballistic solutions to meet the Ministry of Defense's request. The main obstacle is that the majority of raw materials used in the national market are imported, which makes research within the scope of the IME extremely relevant; the Materials Science Program seeks solutions in materials that are abundant in the national territory, such as the case of natural fibers and SiC-based ceramic materials, given that Brazil is the world's fifth largest producer of this type of compound and also of Al_2O_3, and Al_2O_3 can be processed at lower temperatures, without atmospheric control.

The research conducted at the IME, therefore, aims to meet the criteria determined by the Ministry of Defense and promote the BID, or even the Army's own manufacturing units, as was done in previous years through the manufacture of ballistic vests by the Regional Maintenance Park of the 5th Military Region, which were distributed to the troops and are still in use in several Eb's organizations.

Acknowledgments

The authors would like to thank RIMA, FIVEN and DuPont for the provision of raw materials.

References

[1] HENDERSON, J. Ballistic Body Armor Protecting The Protectors. Strategic Standardization, v. 12, n. 4, p. 1-18, 2008.

[2] MAWKHLIENG, U.; MAJUMDAR, A.; LAHA, A. A review of fibrous materials for soft body armour applications. RSC Advances, v. 10, n. 2, p. 1066-1086, 2020.

[3] PRAT, N. et al. Contemporary body armor: technical data, injuries, and limits. European Journal of Trauma and Emergency Surgery, v. 38, n. 2, p. 95-105, 2012.

[4] BALOS, S. et al. Perforated Plate for Ballistic Protection – A Review. Metals, v. 11, n. 4, p. 526, 2021.

[5] CHENG, Y. H. et al. Mechanical characteristics and ballistic behaviors of high strength and hardness armor steels. Journal of Constructional Steel Research, v. 197, p. 107502, 2022.

[6] NAIK, S.; DANDAGWHAL, R. D.; LOHARKAR, P. K. A review on various aspects of Kevlar composites used in ballistic applications. Materials Today: Proceedings, v. 21, p. 1366-1374, 2020.

[7] DENOUAL, C. et al. Visualization of the damage evolution in impacted silicon carbide ceramics. International Journal of Impact Engineering, v. 21, n. 4, p. 225-235, 1998.

[8] MEDVEDOVSKI, E. Ballistic performance of armour ceramics: Influence of design and structure. Part 1. Ceramics International, v. 36, n. 7, p. 2103-2115, 2010.

[9] MEDVEDOVSKI, E. Ballistic performance of armour ceramics: Influence of design and structure. Part 2. Ceramics International, v. 36, n. 7, p. 2117-2127, 2010.

[10] FIGUEIREDO, A. B.H. S. et al. Response to ballistic impact of alumina-UHMWPE composites. Materials Research, v. 21, n. 5, 2018.

[11] BUFFON, S. J.; BORGES, P. C.; AZEVETO, E. C.; LIMA, E. S. Influência do Número de Camadas de Tecido no Desempenho Balístico de Alvos de Kevlar® XP S104. C&T. Revista Militar de Ciência e Tecnologia, v. 36, p. 51-62, 2019.

[12] CROUCH, I. G. Body armour - New materials, new systems. Defence Technology, v. 15, n. 3, p. 241-253, 2019.

[13] BRASIL. Portaria Normativa nº 14/MD, de 23 de março de 2018. Brasília, DF: Ministério da Defesa, 2018.

[14] GOMES FILHO, P. R. S. O projeto Sistema Combatente Brasileiro–COBRA. Doutrina Militar Terrestre em Revista, v. 7, n. 19, p. 6-9, 2019.

[15] LESKE, A. Uma revisão sobre a inovação em defesa: do spin-off ao spin-in. Brazilian Journal of Political Economy, v. 38, n. 2, p. 377-391, 2018.

[16] GUADAHUMI, C. História antiga 16 – Hegemonia de Roma. Babilonialabella.blogspot, [s. l.], 1 mar. 2017. Available from: http://babilonialabella.blogspot.com/2017/03/historia-antigua-16-hegemonia-de-roma-5.html. Access on: Dec. 5, 2022.

[17] ROMERO, F. A brief history of body armor. Time, New York, 2009. Available from: https://content.time.com/time/business/article/0,8599,1889795,00.html. Access on: May 29, 2024.

[18] LAMMLE, R. A Brief History of Bulletproof Vests. Mental Floss, [s. l.], 2010. Available from: https://www.mentalfloss.com/article/24039/brief-history-bulletproof-vests. Access on: May 29, 2024.

[19] ROWEL, D. M. A History of Bulletproof vest and Body Armor. Thought Co., [s. l.], 2011. Available from: https://www.thoughtco.com/history-of-body-armor-and-bullet-proof-vests-1991337. Access on May 29, 2024.

[20] HAZELL, P. J. Advances in Applied Ceramics: Structural, Functional and Bioceramics. Guest Editorial, v. 109, n. 8, p. 445, 2010. DOI: https://doi.org/10.1179/174367610X12804792635864

[21] MORRIS, R. Relembrando os aviadores da 2ª Guerra Mundial. untoldvalor.blogspot.com, [s. l.], 26 abr. 2008. Available from: http://untoldvalor.blogspot.com/2008/04/flight-clothing-for-high-altitudes.html. Access on: Dec. 5, 2022.

[22] DAVID, N. V.; GAO, X.-L.; ZHENG, J. Q. Ballistic resistant body armor: contemporary and prospective materials and related protection mechanisms. Applied Mechanics Reviews, v. 62, n. 5, 2009.

[23] KABIR, R. B.; FERDOUS, N. Kevlar-the super tough fiber. International Journal of Textile Science, v. 1, n. 6, p. 78-83, 2012.

[24] WANG, M. et al. Research on Bending and Ballistic Performance of Three-Dimensional Ply-to-Ply Angle Interlock Kevlar/EP Armor Material. Materials, v. 15, n. 19, p. 6994, 2022.

[25] Les gilets pare-eclats des membres d'equipage aviation aircrew body armor. US Army Collectors. Available from https://usarmy-collectors.pagesperso-orange.fr/fichiers%20listes%20et%20divers/body%20armor%203.htm. Access on: Dec. 5, 2022.

[26] FOUST, C.; JENSON, C. Industry analysis for body armor procurement. 2006.

[27] HOWARD, C. E. This Vest May Save Your Life!. Azimuth, p. 21.

[28] PASGT (Sistema de Armadura Pessoal para Tropas Terrestres). IWM Museum. Available from: https://www.iwm.org.uk/collections/item/object/30013077. Access on: Dec. 5, 2022.

[29] MITCHELL, K. B.; CHOI, H. J.; GARLIE, T. N. Anthropometry And Range Of Motion Of The Encumbered Soldier. Army Natick Soldier Research Development And Engineering Center Ma Natick United States, 2017.

[30] SecPro Advanced EOD Suit. Security Pro USA. Available from: https://www.securityprousa.com/products/sec-pro-advanced-eod-suit. Access on: Dec. 5, 2022.

[31] LOPEZ, C.T. New Soldier armor weighs less, offers more options. US Army, Washington, D.C., 20 mar. 2017. Available from: https://www.army.mil/article/184156/new_soldier_armor_weighs_less_offers_more_options. Access on: Dec. 5, 2022.

[32] SPC - Soldier Plate Carrier. Armor Express. [S. l.]: [20--]. Available from: https://www.armorexpress.com/kdh--defense-systems/. Access on: Dec. 5, 2022.

[33] PARKER III, C. An Approach for the Enhancement of Military Combat, Performance and Personal Protective Equipment for Ground Troops. 2010. Thesis (Master) – Faculty of Auburn University, Auburn, 2010.

[34] NATIONAL INSTITUTE OF JUSTICE. NIJ 0101.04: Ballistic resistance of body armor. Washington, D.C.: National Institute of Justice; 2000.

[35] KELLY, K. et al. Evaluation of the Low Intensity Threat Environment (LITE) Armor Plate and Third Generation Plate Carrier System for the United States Marine Corps. San Diego: Naval Health Research Center San Diego, 2019.

[36] PLACA BALÍSTICA STAND ALONE. Cop, [s. l.], [20--]. Available from: https://www.cop-shop.de/en/product/ballistic-plate-level-vpam9-stand-alone-250-x-300-mm-2610-g-5888. Access on: Dec. 5, 2022.

[37] BRASIL. Instruções Gerais para a Gestão do Ciclo de Vida dos Sistemas e Materiais de Emprego Militar (EB10--IG-01.018). Brasília, DF: Comando do Exército, 2016.

[38] NATIONAL INSTITUTE OF JUSTICE. NIJ 0101.06: Ballistic resistance of body armor. Washington, D.C.: National Institute of Justice, 2008.

[39] NATIONAL INSTITUTE OF JUSTICE. NIJ 0123.00: Ballistic resistance of body armor. Washington, D.C.: National Institute of Justice, 2023.

[40] BRASIL. Portaria nº 211-EME, de 23 de outubro de 2013. Brasília, DF: Estado Maior do Exército, 2013.

[41] BRASIL. Regulamento de Produtos Controlados, aprovado pelo Decreto nº 10.030, de 30 de setembro de 2019.

[42] BRASIL. Portaria nº 18 – D LOG, de 19 de dezembro de 2006.

[43] GREENE, M. Body armor: Protecting our nation's officers from ballistic threats. NIJ Journal, v. 280, p. 24-28, 2018.

[44] V50 Ballistic test for armor. MIL- STD-662F, 1997.

[45] DUPONT. O que é o V50 e como ele pode salvar a sua vida? Dupont, [s. l.], [20--]. Available from: https://www.dupont.com.br/content/dam/dupont/amer/us/en/safety/public/documents/en/Newsletter_car_armor.pdf. Access on: Dec.5, 2022.

[46] *MS Instruments*. Available from: https://msinstruments.co.uk/ballistic-instrumentation/. Access on: Dec. 5, 2022.

[47] BHATNAGAR, A. 4.19 Lightweight Fiber-Reinforced Composites for Ballistic Applications. In: Comprehensive Composite Materials II. Amsterdam: Elsevier, 2018. p. 527-544.

[48] BENZAIT, Z.; TRABZON, L. A review of recent research on materials used in polymer–matrix composites for body armor application. Journal of Composite Materials, v. 52, n. 23, p. 3241-3263, 2018.

[49] THOMAS, E. L. Opportunities in protection materials science and technology for future Army applications. Advances in Ceramic Armor VIII, p. 145-148, 2012.

[50] YADAV, R. et al. Body armour materials: from steel to contemporary biomimetic systems. RSC Advances, v. 6, n. 116, p. 115145-115174, 2016.

[51] DEWANGAN, M. K.; PANIGRAHI, S. K. Factors influencing the ballistic impact mechanisms of textile composite materials: a review. Polymers for Advanced Technologies, 2021.
[52] ZHANG, H.; SHI, M.; ZHANG, J.; WANG, S. Effects of Sunshine UV Irradiation on the Tensile Properties and Structure of Ultrahigh Molecular Weight Polyethylene Fiber. Journal of Applied Polymer Science, v. 89, p. 2757-2763, 2003.
[53] VIVAS, V.; SUAREZ, J. C. M.; WERBER, R. P. Influência da degradação ambiental no comportamento mecânico e balístico de compósitos produzidos com fibra de polietileno de ultra alto peso molecular. 2013, 216f. Thesis (Mater in Materials Science) – Instituto Militar de Engenharia, Rio de Janeiro, 2013.
[54] CUROSU, I. et al. Tensile behavior of high-strength strain-hardening cement-based composites (HS-SHCC) made with high-performance polyethylene, aramid and PBO fibers. Cement and Concrete Research, v. 98, p. 71-81, 2017.
[55] TABIEI, A.; NILAKANTAN, G. Ballistic impact of dry woven fabric composites: a review. Applied Mechanics Reviews, v. 61, n. 1, 2008.
[56] WILHELM, M.; BIR, C. Injuries to law enforcement officers: the backface signature injury. Forensic Science International, v. 174, n. 1, p. 6-11, 2008.
[57] NATIONAL INSTITUTE OF JUSTICE (NIJ) et al. Status Report to the Attorney General on Body Armor Safety Initiative Testing and Activities, 2004.
[58] LAMMERS, M. et al. Mechanical properties and structural transitions in the new rigid-rod polymer fibre PIPD (M5') during the manufacturing process. Polymer, v. 39, n. 24, p. 5999-6005, 1998.
[59] MONTEIRO, S. N. et al. Natural fibers reinforced polymer composites applied in ballistic multilayered armor for personal protection – an overview. Green Materials Engineering, p. 33-47, 2019.
[60] COSTA, U. O. et al. Effect of graphene oxide coating on natural fiber composite for multilayered ballistic armor. Polymers, v. 11, n. 8, p. 1356, 2019.
[61] NURAZZI, N. M. et al. A review on natural fiber reinforced polymer composite for bullet proof and ballistic applications. Polymers, v. 13, n. 4, p. 646, 2021.
[62] DE LIMA, T. E. S. et al. Potential of Using Amazon Natural Fibers to Reinforce Cementitious Composites: A Review. Polymers, v. 14, n. 3, p. 647, 2022.
[63] BRAGA, F. O.; LIMA JR., E. P.; LIMA, E. S.; MONTEIRO, S. The Effect of Thickness on Aramid Fabric Laminates Subjected to 7.62 mm Ammunition Ballistic Impact. Materials Research-Ibero-american. Journal of Materials, v. 1, p. 1, 2017.
[64] WACHTMAN, J. B. Jr, Structural ceramics, Academic Press Inc., San Diego, 1989.
[65] CHAWLA, K. K. Composite materials: Science and engineering. London: Springer, 1987.
[66] SALEIRO, G. T. et al. Mechanical behavior of SiC additivated with Al_2O_3 and Y_2O_3 produced by synthesis by auto combustion sustained at high temperature. Tecnologia em Metalurgia, Materiais e Mineração, v. 15, n. 2, p. 96, 2018.
[67] DRESCH, A. B. et al. Ballistic Ceramics and Analysis of their Mechanical Properties for Armour Applications: A Review. Ceramics International, v. 47, n. 7, Part A, p. 8743-8761, 2021.
[68] REED, J. S. Principles of ceramics processing. London: John Wiley & Sons, 1995.
[69] GOMES, A. V., Comportamento balístico da alumina com adição de nióbia e variação da geometria do alvo. 2004. Dissertation (PhD in Materials Science) - IME, 2004.
[70] MEYERS, M. A. Dynamic behavior of materials. London: John Wiley & Sons, 1994.
[71] POPA, I.-D.; DOBRIȚA, F. Considerations on Dop (Depth Of Penetration) Test for Evaluation of Ceramics Materials Used in Ballistic Protection. ACTA Universitatis Cibiniensis, v. 69, n. 1, p. 162-166, 2017.
[72] RAHBEK, D. B. et al. Effect of composite covering on ballistic fracture damage development in ceramic plates. International Journal of Impact Engineering, v. 99, p. 58-68, 2017.
[73] HEALEY, Adam. Understanding the ballistic event: methodology and observations relevant to ceramic armour. 2017. Dissertation (PhD) – University of Surrey, Surrey, 2017.
[74] CONSENTINO, P.A. S. L. Efeito de carbetos metálicos na sinterização do carbeto de boro por prensagem a quente. 2006. 150f. 2006. Tese de Doutorado. Tese (Doutorado em Engenharia Metalúrgica e de Materiais) – Universidade Federal do Rio de Janeiro, Rio de Janeiro.
[75] RAHBEK, D. B.; JOHNSEN, B. B. Dynamic behaviour of ceramic armour systems. Kjeller: Norwegian Defence Research Establishment, 2015.

[76] DA SILVA, M.V.; STAINER, D.; AL-QURESHI, H.A.; HOTZA, D. Blindagens Cerâmicas para Aplicações Balísticas: Uma Revisão. Cerâmica, v. 60, p. 323-331. 2014.
[77] KAUFMANN, C. et al. Influence of material properties on the ballistic performance of ceramics for personal body armour. Shock and Vibration, v. 10, n. 1, p. 51-58, 2003.
[78] PICKERING, E. G. et al. Effect of confinement on the static and dynamic indentation response of model ceramic and cermet materials. International Journal of Impact Engineering, v. 110, p. 123-137, 2017.
[79] FISHER, J.T., Validation of a simple go/no-go damage detection system for personal ceramic body armor using pressure sensitive film. Graduate Theses and Dissertations. Iowa State University, Iowa, 2011.
[80] KARANDIKAR, P. G. et al. A review of ceramics for armor applications. Advances in Ceramic Armor IV, v. 29, p. 163-175, 2009.

VOL.40 Nº2 2023
https://doi.org/10.22491/rmct.v40i2.11269.en

Evaluation of the mechanical properties of AA 5052 and AA 5050C aluminum alloy rolled sheets

Isabella Cristina da Silva Jorge[1], Natália Barros Barony[1], Ângelo Siqueira da Silva[1], Talita Gama de Sousa[1], Saulo Brinco Diniz[2], Andersan dos Santos Paula[1]
[1] Military Institute of Engineering, Rio de Janeiro, RJ, Brasil
[2]Federal Center of Technical Education Celso Suckow da Fonseca, Angra dos Reis, RJ, Brasil
isabellajorge@ime.eb.br

Abstract: *This study was conducted on AA 5052 sheets produced by direct casting and AA 5050C produced by twin roll casting, to microstructurally and mechanically characterize these alloys and evaluate dynamic aging occurrence as a function of the strain rate applied in uniaxial tensile tests. In general, AA 5052 alloy showed higher strength values and lower ductility. Analysis of the aspect of tensile curves showed serrations in both alloys, indicating rapid and successive stresses variations in the plastic deformation region for both alloys, suggesting dynamic aging occurrence and how this effect is more pronounced at lower displacement speed. The frequency and magnitude of the decrease stress can be associated with the distinct Mg content of the alloys, being smaller in the AA 5050C.*

KEYWORDS: *5xxx aluminum alloys, Direct chill process, Twin roll caster process, mechanical properties, aging dynamic.*

Resumo: *Este estudo foi conduzido em chapas das ligas AA 5052, produzida por processo de fundição direta (DC), e AA 5050C, produzida por processo de fundição contínua de chapas (TRC), com o intuito de caracterizar microestrutural e mecanicamente as referidas ligas, assim como avaliar a ocorrência de envelhecimento dinâmico em função da taxa de deformação aplicada em ensaios de tração uniaxial. De maneira geral, observou-se valores superiores de resistência e menor ductilidade para a liga AA 5052, e ao analisar o aspecto das curvas de tração, pôde-se verificar a presença de serrilhados em ambas as ligas, indicativos de variações rápidas e sucessivas de tensões, na região de deformação plástica, sugerindo a ocorrência do envelhecimento dinâmico, e como, em menor velocidade de deformação, esse efeito é mais pronunciado. A frequência e magnitude de quedas de tensão verificadas podem ser associadas principalmente aos diferentes teores de Mg das ligas, sendo menor para a liga AA 5050C que possuí menor teor de Mg.*

PALAVRAS-CHAVE: *Ligas de alumínio 5xxx, processo de fundição contínua, processo de fundição direta, propriedades mecânicas, envelhecimento dinâmico.*

1. Introduction

Aluminum alloys, due to their interesting combination between strength and weight, good conformability, and high corrosion resistance, among other characteristics, have stood out as a viable alternative for applications in the automotive industry in the production of components or structural parts, and have gained prominence mainly for applications in bus bodies due to the possibility of reducing the weight of automobiles, resulting in reduced fuel costs and gas emissions [1].

However, such applications are still restricted due to the complex technology and high cost of aluminum production when compared to steel. The most used method for the manufacture of aluminum alloys in the form of plates is based on the direct casting process (*Direct Chill – DC*).

The direct chill (DC) process consists of the casting of plates, followed by a machining and hot rolling process, in order to significantly reduce the thickness of the plate in a hot plastic forming process. Subsequently, the sheet goes to cold rolling, which increases its mechanical properties in terms of strength, combined with the decrease in ductility, and in some cases, subsequently goes to annealing heat treatment for stress relief/stabilization or partial/total recrystallization, according to the final application [2,3].

Another way of obtaining aluminum laminates and their alloys is through the Twin roll caster (TRC) process, in which the manufacture of hot rolled and coiled sheets occurs directly from the liquid metal.

The process consists in a combination of the material solidification and hot rolling steps, which allows the sheet, in the form of a coil, to proceed directly to the cold rolling process [4,5].

Aluminum sheets processing through twin roll casting (TRC) reduces not only the costs in the manufacturing process, but also processing time. Such characteristics, combined with the ease of changing the thickness and width of the casting without the need to change the dimensions of the mold, make production more agile and advantageous [5].

Aluminum alloys of different series are usually produced from the DC process and are later laminated (by hot and cold processes) and annealed, but the production of some of them on a laboratory and industrial scale by the TRC process is also observed, with some reservations. The literature highlights that alloys with a narrow solidification interval are largely produced in several dimensions by the TRC process. However, for alloys with a wide solidification range, the process is still limited, not allowing one to obtain a final product with the appropriate mechanical properties [6]. Another limiting factor is the chemical composition of the alloys, some of which can present major problems related to the formation of segregation centerlines and of an excessive oxide layer, such as the alloys of the 5xxx series. This factor was present in the Companhia Brasileira de Alumínio (CBA), in Alumínio/São Paulo (SP), when trying to produce the AA 5052 alloy in its original composition by TRC, being possible to circumvent the problem only with the compositional adjustment that resulted in the AA 5050C alloy [7], being both objects of this study.

Another aspect of the laminated products of the 5xxx series alloys is that they are likely to present dynamic aging as a function of the strain rate to which they are subjected, even at room temperature, which is revealed by serrations in the stress-strain curve [8,9]. The justification for this behavior – the serrated pattern – is attributed to the abrupt movement of dislocations, which results in the dynamic interaction of dislocations with substitutional solute atoms present in the solid solution [9]. In this perception, one assumes the movement of dislocations is prevented by solute atoms that isolate them; consequently, an increased tension is necessary for the dislocations to be unlocked, resulting in a negative tension/deformation, leading to flow instability, i.e., the Portevin-Le Chatelier (PLC) effect.

Therefore, this study aimed to perform a microstructural and mechanical characterization of laminated and annealed AA 5052 and AA 5050C aluminum alloy sheets, produced by CBA from DC and TRC processes, respectively, as well as to evaluate the occurrence of aging in the alloys when mechanically requested via uniaxial tensile test at two different speeds and at room temperature.

2. Material and Methods

The materials under study, provided by the company Companhia Brasileira de Alumínio (CBA) – located in Alumínio - SP, consist of two aluminum alloys of the 5xxx series, AA 5052 and AA 5050C – according to the chemical composition presented in Table 1 – which were produced by different processes, the first via direct chill (DC) and the second by twin roll casting (TRC). These alloys were subsequently subjected to the same processing route and parameters until obtaining thin sheets with approximately 1.20 mm thickness in the final cold rolled and annealed/stabilized condition, as shown in Figure 1, which will only be distinguished by the value of the total reduction in the first cold rolling step (68.3% for alloy 5052 and 72.8% for alloy 5050C) and soaking temperature in the intermediate annealing (360°C for alloy 5052 and 380°C for alloy 5050C).

Table 1 - Chemical composition of the alloys under study, with emphasis on the elements of alloys and residuals, % in weight.

Si	Fe	Cu	Mn	Mg	Ti	Cr
AA 5052						
0.06	0.26	0.06	0.06	2.41	0.20	0.01
AA 5050C						
0.07	0.47	0.36	0.10	1.39	0.00	0.04

Source: CBA.

Figure 1 - Processing steps in the CBA of the 5xxx series alloys under study.

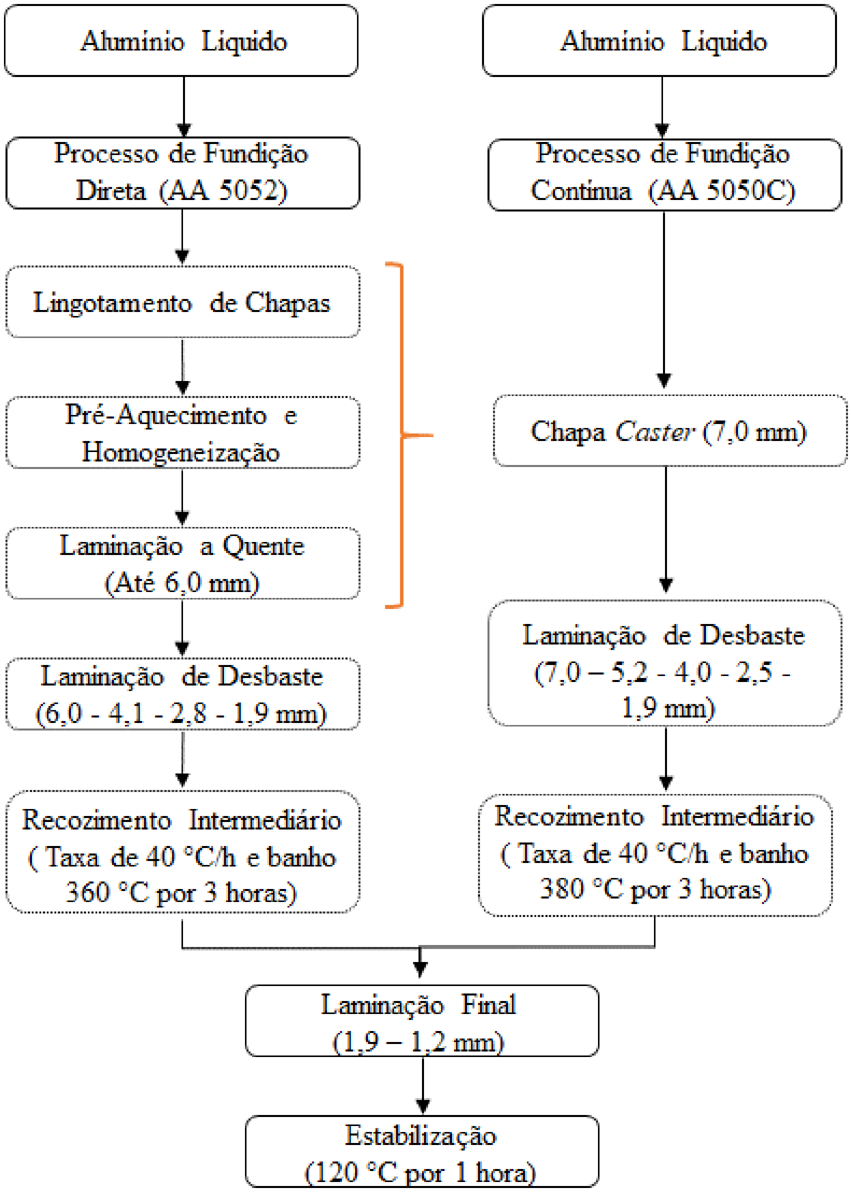

Source: CBA.

Microstructural characterization was conducted with the aid of a scanning electron microscope with a field emission cannon, FEI Quanta FEG, observing the samples in the thickness of the plate, in the plane containing the lamination direction (DL), after metallographic preparation: sanding from 220 to 4000 mesh, polishing in 3 and 1 μm diamond paste, and a final electrolytic polishing with perchloric acid solution (20% $HClO_4$ + 80% C_2H_5OH) for 5 seconds at 10 Volts, at room temperature.

For mechanical characterization, Vickers hardness and uniaxial tensile tests were performed. The hardness test was conducted with 10 measurements for each sample along the plate plane, with a load of 10 kgf. Whereas the uniaxial tensile test was conducted on specimens made according to ASTM E8/E8M

[10] under two conditions of crossbar displacement speed (2 and 7 mm/min), using different strain gauge technologies (contact for speed of 2 mm/min and optical for speed of 7 mm/min), in order to ascertain the occurrence of dynamic aging as a function of the deformation speed.

3. Results and Discussion

Figures 2 and 3 show results from the microstructural analysis via Scanning Electron Microscopy (SEM) using the backscattered electron detector (BSE) of AA 5052 and AA 5050C alloys, respectively.

Figure 2 - Micrograph of AA 5052 alloy (DL, with arrows indicating cavities (in black) that contained parts of the possible inclusion particles/precipitates still present (in white).

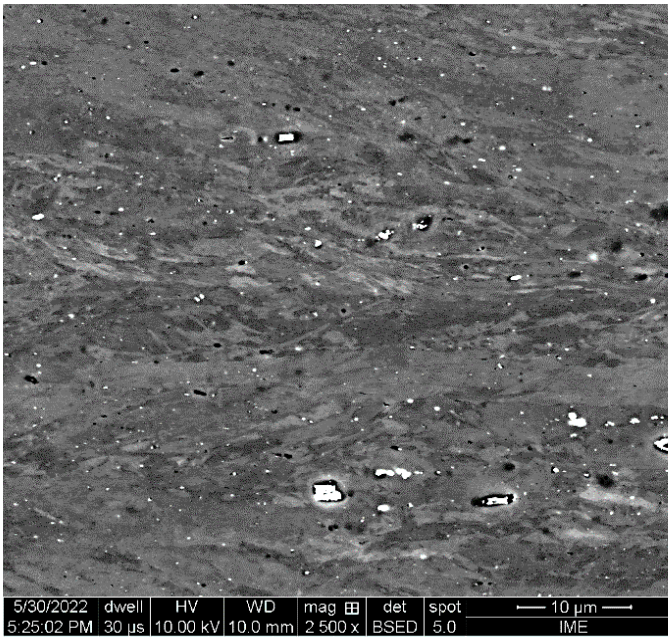

Source: Prepared by the authors.

One can see homogeneous and similar distribution of inclusions and/or precipitates along the samples aligned in the DL, and that the alloy produced by the twin roll casting process (AA 5050C) apparently presents inclusions/second phase particles in greater amount distributed along the matrix in relation to the alloy produced by the direct chill process (AA 5052). This can be explained in two possible ways. The first possibility may be associated with the higher solidification rates obtained in the twin roll casting process, which favors the formation of a greater number of sites for second phase nucleation [11]. The second possibility, if most of these particles are associated with inclusions, refers to the fact that the ingot produced by direct chill – DC, the AA 5052 alloy, is subjected to a surface scarfing process before being hot rolled, which guarantees the removal of much of the alumina (Al_2O_3) layer formed on the surface of the ingot, while the product of twin roll casting – TRC, the AA 5050C alloy, keeps in its volume all the alumina formed during the casting process combined with hot rolling. One also observed that electrolytic polishing promoted the removal of part of the inclusions and/or precipitates due to the anodic behavior in the formed electrolytic cell, giving rise to the cavities presented together with the metal matrix in these microstructures, as highlighted in Figures 2 and 3.

Figure 3 - Micrograph of AA 5050C alloy (DL→), with arrows indicating cavities (in black) that contained parts of the possible inclusion particles/precipitates still present (in white).

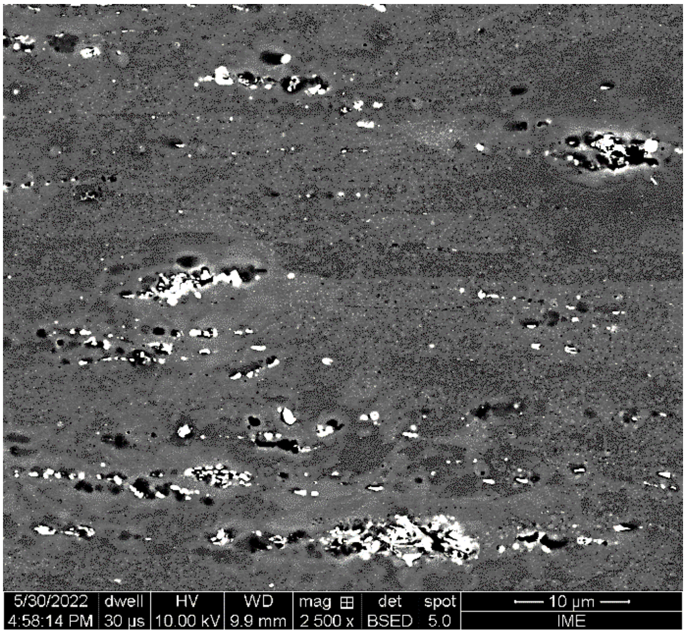

Source: Prepared by the authors.

Table 2 shows the results of the Vickers hardness test performed. The average hardness values presented in the alloys showed a significant difference, and it was possible to observe a reduction of 21.78% in the hardness value for alloy AA 5050C compared to AA 5052. Considering the variance calculated and reliability of the results obtained in the test, one should emphasize there was no significant dispersion between the values obtained for each alloy under study.

Table 2 - Results of the Vickers hardness test.

	AA 5052	AA 5050C
Mean	87.38	68.35
Standard Deviation	2.42	1.38
Variance	5.86	1.91
Minimum	83.59	65.64
Maximum	91.17	69.92
Number of measurements	10	10
Reliability index (95%)	1.50	1.18

Source: Prepared by the authors.

The AA 5050C alloy, due to its greater number of inclusions and/or second phase particles dispersed in the matrix by its production via twin roll casting process, was expected to be harder than AA 5052. This fact is not observed and can be explained by the compositional difference of the alloys (Table 1). The AA 5050C alloy is a compositional adaptation of AA 5052 alloy, aimed at reducing the oxide layer formed during TRC processing. Magnesium was one of the altered elements, having its amount reduced, and because it is an element that is preferably found in solid solution, this reduction in content directly affects the hardness and mechanical strength of the alloy. These indications highlight that these particles observed in SEM analyses are probably largely associated with alumina (Al_2O_3) inclusions, which have no role in alloy hardening, as it occurs with the second intermetallic phase particles formed in this type of alloys. Another point that supports the lower hardness behavior for the 5050C alloy are the conditions under which it was subjected to thermomechanical processing, i.e., the highest total reduction applied in the first cold rolling step and the highest soaking temperature to which it was exposed in the intermediate annealing (Figure 1). These factors may have provided reduced recrystallization temperature (by the reduction imposed on the thinning lamination) plus the possibility of grain growth (by the soaking temperature imposed on the annealing for recrystallization) in the condition that was subsequently subjected to final cold rolling and annealing for stabilization, thus also contributing to the decrease in hardness.

Figure 4 shows the engineering stress-strain curves of alloys AA 5052 and AA 5050C, with strain speeds in the uniaxial tensile test of 2 mm/min and 7 mm/min.

Regarding the aspect of the curve, serrations caused by the Portevin-Le Chatelier effect, or dynamic aging behavior, are observed in the plastic deformation region of both alloys tested at a speed of 2 mm/min. The AA 5052 alloy exhibits not only a higher magnitude of voltage dips (difference between peak and valley voltage in each dentition), but also a higher frequency (number of voltage dips) when compared to AA 5050C.

According to the dynamic stress aging model, when the movement of dislocations is temporarily interrupted in obstacles, such as forests of dislocations, the solute atoms that are already isolated in these obstacles migrate toward these fixed dislocations. They then form atmospheres around the dislocations and cause them to be blocked. When the applied force is high enough, the movable dislocations detach from the atmospheres and advance freely toward other obstacles. The repetition of this process constitutes the serrated production observed in the stress-strain curve [12].

Thus, one can infer that, as the AA 5052 alloy has a higher concentration of magnesium (Table 1), most of the Mg solute atoms move in the direction of the dislocations and, therefore, unlocking such dislocations is more difficult. Therefore, a greater force is required to move the dislocation, resulting in a greater stress drop in the stress-strain curve. On the other hand, when the magnesium concentration is high, the interaction of magnesium solute atoms with the dislocations is more frequent and, consequently, the process of voltage drops becomes more frequent. One can see that serration occurs at a higher frequency for AA 5052 than for the AA 5050C alloy.

Figure 4 - Engineering stress-strain curves of alloys AA 5052 and AA 5050C, with strain speeds in the uniaxial tensile test of 2 mm/min and 7 mm/min.

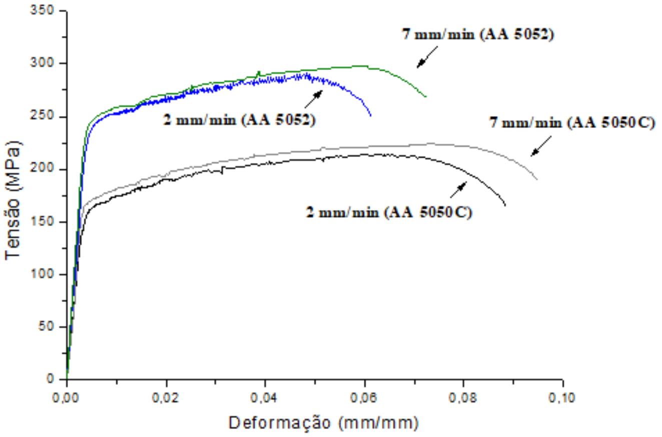

Source: Prepared by the authors.

For the curves tested with a deformation speed of 7 mm/min, there is, as expected, a decrease in the amount and intensity of serration. This fact occurs due to the increase in deformation rate, since there is no time for the movement of the solute atmosphere, which is responsible for dynamic aging. Thus, this test speed is not sufficient to eliminate serrations, however, the voltage drops become less frequent.

Table 2 shows the mechanical properties of alloys AA 5052 and AA 5050C obtained through uniaxial tensile tests performed with a deformation rate of 2 mm/min and 7 mm/min.

Table 2 - Mechanical properties of AA 5052 and AA 5050C alloys extracted from tensile tests.

Properties	Strain Speed (mm/min)			
	AA 5052		AA 5050C	
	(2)	(7)	(2)	(7)
Yield strength (σe) (MPa)	240.74 ± 8.06	254.26 ± 6.13	156.61 ± 6.96	169.88 ± 0.41
Elasticity Modulus (E) (GPa)	66.78 ± 5.83	71.84 ± 6.36	68.58 ± 11.68	73.52 ± 13.38
Tensile Strength Limit (LRT) (MPa)	286.76 ± 9.39	298.91 ± 20.47	211.13 ± 2.39	209.46 ± 0.48
Uniform Elongation (%)	4.24*	5.44*	5.91*	5.69*
Elongation at break (%)	4.82*	6.05*	6.60*	6.32*

***Data extracted from the stress-strain curves in Figure 4.**
Source: Prepared by the authors.

As for the mechanical properties observed in the tensile test, it is possible to verify that the AA 5052 alloy presented higher values of tensile and yield strength and lower values of elongation when compared to the AA 5050C alloy, as also observed in the hardness test. According to the literature, materials processed by twin roll casting (TRC) have superior mechanical properties in terms of strength when compared to those produced by direct chill casting (DC). This fact stems from the presence of a greater number of second phase precipitates during TRC, where the precipitates are possibly anchored, preferably, in the grain contours, acting as grain refiners [13]. Analyzing the Hall-Petch equation, it is observed that the relationship between grain size and stress are inversely proportional, i.e., the smaller the grain size, the greater the tensile strength of the material. It is inferred, through the mechanical properties obtained, that the alloys under study presented behavior contrary to that presented in the literature.

This behavior can be explained by the difference in composition between the alloys, since the AA 5050C alloy has a lower magnesium and chromium content and a higher copper content, added to the fact that it was subjected to a greater reduction in thickness and higher soaking temperature in the processes subsequent to hot rolling, that is, from cold rolling to roughing and intermediate annealing for recrystallization, which were adopted for the AA 5052 alloy, before being subjected to conditions similar to the alloy 5052 in the final lamination and annealing for stabilization (Figure 1). This compositional variation was necessary to reduce surface oxidation during solidification in TRC processing. Thus, despite having the propensity to present more refined grains by the TRC process, in relation to the AA 5052 alloy, the AA 5050C alloy has lower limits of tensile and yield strength, and higher ductility, probably justified by the lower hardening by solid solution and/or precipitation, due to the composition, added to the larger grain size due to the intermediate processing (as shown in Figure 1).

Regarding the use of different test speeds in uniaxial traction, comparing the results obtained, one observed that these presented differences for the values of yield strength, elasticity modulus, strength limit, and elongation. This effect in relation to the values of yield, strength, and elongation limits can be explained due to the increased number of stacked dislocations due to the increased deformation rate, which causes greater resistance in the beginning of deformation, greater hardening and extension in the plastic deformation capacity, in the uniform deformation regime, and located in the stricture [14]. However, in relation to the modulus of elasticity, the difference can be attributed to the fact that the test was conducted with different strain gauge technologies (contact for a speed of 2 mm/min and optical for a speed of 7 mm/min).

4. Final considerations

Mechanical strengths presented by the properties of the AA 5052 alloy, such as yield and tensile strength, were higher than those presented by the AA 5050C alloy, both in uniaxial traction and Vickers hardness testing, unlike the lower ductility. This result can be explained by variations in the chemical compositions of each alloy and in the production processes. It is possible that small decreases in temperatures and/or soaking time in the intermediate annealing and stabilization treatments provide adjustments that would result in close values of properties of both alloys subjected to distinct reductions in thinning cold rolling and the like in the final cold rolling, without further adjustments in the chemical composition of the alloy 5050C.

Thus, the AA 5050C alloy can be considered as a viable option to replace the AA 5052 alloy for applications that do not require high mechanical strength and exhibit greater ductility under the processing conditions adopted for this study.

As for the occurrence of dynamic aging, the presence of serrations in the region of plastic deformation in both alloys indicates the existence of the phenomenon. The frequency and magnitude of voltage drops verified can be associated with the different Mg contents of the alloys, depending on their presence in solid solution. It is also observed that the increase in the deformation speed from 2 mm/min to 7 mm/min during the tensile test promotes a decrease in the amount and intensity of serrations, as well as a greater extension in the uniform and total elongation, probably due to the reduction of the time for the movement of the solute atmosphere during the sliding of dislocations. That is, the forming processing of these alloys to obtain parts can be easily performed without the occurrence of dynamic aging when performed under higher strain rates.

Acknowledgments

The authors thank CBA for the donation of the alloys for this study, the Military Institute of Engineering (IME) for the laboratory infrastructure for conducting the characterizations and, particularly, the Research Center of Companhia Siderúrgica Nacional (CSN) for carrying out the tensile tests with optical strain gauge. In addition, we thank the CNPq and

CAPES/PROEX for the master's and doctoral scholarships, as well as for the resources for the preparation of the traction specimens subsidized by CAPES/PROEX of the Graduate Program in Materials Science (PPGCM) of IME.

Bibliographic References

[1] ABAL – ASSOCIAÇÃO BRASILEIRA DO ALUMÍNIO. Vantagens e desvantagens do alumínio. *Abal*, São Paulo, [20--?]. Disponível em: https://abal.org.br/aluminio/vantagens-do-aluminio/. Acesso em: 27, jul. 2018.

[2] OTOMAR, H. P.; PLAUT, R. L. Comparision of the microstructure and texture evolution in AA 1050 aluminum alloy sheets produced by the DC and CC methods. *In*: SUAREZ, C. E. *et al*. (org.). *Light Metals 2012*. New York: Springer, 2012. p. 223-238.

[3] DU, Q.; ESKIN, D. G.; KATGERMAN, L.; NADELLA, R. Macrosegregation in direct-chill casting of aluminium alloys. **Progress in Materials Science**, [*s. l.*], v. 53, n. 3, p. 421-480, 2008.

[4] BAREKAR, N. S.; BHAGURKAR, A. G.; DAS, S.; FAN, Z. FAKIR O. E.; HUANG, Y.; YANG, X.; ZHOU, L.; The impact of melt conditioning on microstructure, texture and ductility of twin roll cast aluminium alloy strips. **Materials Science & Engineering A**, [*s. l.*], v. 650, p. 365-373, 2016.

[5] KARLÍK, M.; ROUBAUT, F.; SLÁMA, P.; SLÁMOVÁ, M.; VÉRONA, M. Differences in microstructure and texture of Al–Mg sheets produced by twin-roll continuous casting and by direct-chill casting. **Materials Characterization**, [*s. l.*], v. 49, n. 3, p. 231-240, 2003.

[6] OGATA, C. T. **Correlações entre microestrutura, parâmetros térmicos e propriedades mecânicas de ligas de alumínio da série 5xxx solidificadas unidirecionalmente**. 2017. 106 p. Dissertação (Mestrado em Ciência e Engenharia dos Materiais) – Universidade Federal de São Carlos, São Carlos, 2017.

[7] BARONY, N. B. **Avaliação estrutural e mecânica de chapas das ligas de alumínio AA 5052 E AA 5050C**. 2019, 126 p. Dissertação (Mestrado em Ciência dos Materiais), Instituto Militar de Engenharia, 2019.

[8] CHEN, X.; FANG, Y.; MAO, J.; PAN, F.; WANG, B. Effects of cold rolling and heat treatment on microstructure and mechanical properties of AA 5052 aluminum alloy. **Transactions of Nonferrous Metals Society of China**, [*s. l.*], v. 25, n. 8, p. 2481-2489, 2015.

[9] ABOULFADL, H.; CHOI, P.; DEGES, J.; RAABE, D. Dynamic strain aging studied at the atomic scale. **Acta Materialia**, [*s. l.*], v. 86, p. 34-42, 2015.

[10] ASTM – AMERICAN SOCIETY FOR TESTING AND MATERIALS. **ASTM E8/E8M – 13a**: Standard Test Method for Tension Testing of Metallic Materials. West Conshohocken: ASTM, 2013. 28 p.

[11] HOSEINIFAR, A.; SALARI, S.; SOLTAN, M. A. N. Effect of twin-roll casting parameters on microstructure and mechanical properties of AA5083-H321 sheet. **Transactions of Nonferrous Metals Society of China**, [*s. l.*], v. 26, n. 10, p. 2552-2560, 2016.

[12] MORRIS, J. G.; WEN, W.; ZHAO, Y. The effect of Mg precipitation on the mechanical properties of 5xxx aluminum alloys. **Materials Science and Engineering A**, [*s. l.*], v. 392, n. 1-2, p.136-144, 2005.

[13] MARTINS, J. P.; PADILHA, A. F. Caracterização da liga comercial de alumínio 3003 produzida por fundição contínua de chapas (twin roll caster) – microestrutura. **Revista Escola de Minas**, Ouro Preto, v. 59, n. 4, p. 427-431, 2006.

[14] DONIČ, T.;.; KOČIŠKO, R.; KOVÁČOVÁ, A.; KVAČKAJ, M.; KVAČKAJ, T.; POKORNÝ, I. Influence of strain rate on ultimate tensile stress of coarse-grained and ultrafine-grained copper. **Materials Letters**, [*s. l.*], v. 64, n. 21, p. 2344-2346, 2010.

VOL.40 Nº2 2023
https://doi.org/10.22491/rmct.v40i2.11327.en

Ballistic resistance and microwave absorbing properties of a composite made of aramid fabric impregnated with polyethylene glycol and hematite nanoparticles

Danúbia Bordim de Carvalho[1*]
[1] Military Institute of Engineering --Praça General Tibúrcio, 80, Praia Vermelha, Rio de Janeiro, RJ, Brazil, ZIP code 29.270-030
*** dan.bordim@gmail.com**

ABSTRACT: *The ballistic resistance and microwave absorption of a composite of aramid fabric impregnated with polyethylene glycol and hematite nanoparticles was investigated for different hematite concentrations between 0 and 17 wt%. Different damage and energy absorbing mechanisms during ballistic impact were identified: cone formation on the back face of the target, tensile failure of primary yarns and deformation of secondary yarns. In terms of energy absorption, the best results were achieved with 7 wt% hematite, while the smallest depth of penetration (DOP) was observed for a composite with 9 wt% hematite. A scanning electron microscope (SEM) image of the composite with 7% hematite after the ballistic test showed that the main energy absorption mechanism was deformation of secondary yarns. Microwave absorption was measured using the waveguide technique in the frequency range from 8 to 12 GHz. Results showed that the dielectric loss* $\varepsilon''/\varepsilon'$ *is maximum for a concentration of 3% hematite, while the magnetic loss* μ''/μ' *is maximum for a concentration of 11 wt% hematite. A reasonable compromise between ballistic resistance and microwave absorption seems to be a composite with 7 wt% hematite.*

KEYWORDS: Radar absorption; Ballistic shielding; Ballistic impact; Shear thickening fluid.

RESUMO: *A resistência balística e a absorção de micro-ondas de um composto de tecido de aramida impregnado com polietilenoglicol e nanopartículas de hematita foram investigadas para diferentes concentrações de hematita entre 0 e 17% em peso. Foram identificados diferentes mecanismos de dano e de absorção de energia durante o impacto balístico: formação de cone na face posterior do alvo, falha de tração dos fios primários e deformação dos fios secundários. Em termos de absorção de energia, os melhores resultados foram obtidos com hematita a 7% em peso, enquanto a menor profundidade de penetração (DOP) foi observada em um composto com hematita a 9% em peso. Uma imagem de microscópio eletrônico de varredura (SEM) do compósito com 7% de hematita após o teste balístico mostrou que o principal mecanismo de absorção de energia foi a deformação dos fios secundários. A absorção de micro-ondas foi medida usando a técnica de guia de ondas na faixa de frequência de 8 a 12 GHz. Os resultados mostraram que a perda dielétrica* $\varepsilon''/\varepsilon'$ *é máxima para uma concentração de 3% de hematita, enquanto a perda magnética* μ''/μ' *é máxima para uma concentração de 11% em peso de hematita. Um compromisso razoável entre a resistência balística e a absorção de micro-ondas parece ser um composto com 7 wt% de hematita.*

PALAVRAS-CHAVE: Absorção de radar; blindagem balística; impacto balístico; fluido de espessamento por cisalhamento.

1. Introduction

Since ancient times, mankind has sought the development of body protection against hazards and injuries. Animal skins, natural fibers and metallic materials such as bronze, iron and steel were used for this purpose throughout history. During the 20th century, natural fibers gave way to synthetic ones.

Modern armor is designed to protect against projectiles as well as against puncturing and cutting caused by sharp objects. They generally consist of a combination of metal, ceramics and fabrics. Fabrics are composed of high strength polymer fibers that provide added protection without compromising the mobility of soldiers, police officers and security personnel[1,2]. Advanced reinforcements were developed to improve the flexibility and reduce the weight of these fabrics using fewer layers and maintaining the same efficiency. These reinforcements are created by impregnating the fabrics with non-Newtonian fluids whose apparent viscosity vary with increasing stress[3-11].

The choice of magnetic nanoparticles for the production of a non-Newtonian fluid may add the property of being a Radar Absorption Material (RAM) to the fabric. These materials are efficient attenuators of electromagnetic radiation at wavelengths used by radars, reducing the radar cross section of soldiers, automobiles, warships and military aircrafts. Teber et al.[12] used Ni-Co magnetic materials in polymeric composites as absorbers of X-band microwaves (8-12 GHz).

The purpose of this work was to study the armor reinforcement and radar absorption behavior[12-17] of a non-Newtonian fluid based on hematite. For this, mixtures of hematite nanoparticles with PEG-200 were produced with different concentrations of hematite. These blends were used to impregnate the aramid fabric; the ballistic resistance and the microwave absorption properties of the composite were evaluated for different hematite concentrations. In addition, damage and energy absorbing mechanisms during ballistic impact were investigated.

2. Materials and methods

2.1 Materials

The materials used in this work were ferric nitrate (Sigma-Aldrich, 98%), glycine (Sigma-Aldrich, 98.5%), 200 g/mol PEG (Honeywell Riedel-de Haën), absolute ethanol (Quimex, 93%), 0.28 mm thick aramid fabric with a 210 g/m² density [HY Networks (Shanhai)] and 1 inch thick MDF (Arauco do Brasil).

2.2 Sample Preparation

The hematite nanoparticles were synthesised using the combustion method with a 0.5 glycine/nitrate ratio[18,19]. Mixtures of PEG-200 with 0%, 3%, 5%, 7%, 9%, 11%, 13%, 15% and 17% hematite were sonicated for 30 min, diluted in 40 mL of ethanol, sonicated again for 30 minutes and used to impregnate two square pieces of aramid fabric with an area of 49 cm² in a 150 mm diameter watch glass. These pieces were pressed for 10 min at 3 ton/cm². Pressing the samples reduces the mass without decreasing ballistic resistance, because only non-impregnated fluid is removed. After this, the samples were oven dried at 79 °C for 24 h.

2.3 Experimental Methods

The hematite was characterized by X-ray diffraction using an Expert Pro Panalitical diffractometer with Cu Kα (1,5418 Å) radiation and TOPAS software based on the Rietveld method.

A Gunpower SSS air rifle with a noise suppressor Padrão Armas was used for the ballistic tests. The projectile was a 22-gauge lead shot with an estimated mass of 3.3g. The muzzle speed was measured using an Air Chrony MK3 ballistic chronograph with a precision of 0.15 m/s and the residual speed was measured using a ProChrono Pal ballistic chronograph with a precision of 0.31 m/s.

After the ballistic tests, images of samples with 7% hematite were obtained in a FEI Quanta FEG 250 SEM.

The electromagnetic characterization of the composites was performed by reflectivity/absorption measurements using the waveguide technique in the X-band of the electromagnetic spectrum (8 to 12 GHz). This device was coupled to an KEYSIGHT PNA-L Network Analyzer (model N5232A) with a frequency generator (300 kHz-20 GHz). The reference material used to evaluate the absorption efficiency of the composites was an aluminum plate, which reflects 100% of the incident radiation.

2.4 Relative mass M_c

The relative mass M_c was calculated using Eq. 1 to express the relative amount of impregnation of aramid by the fluid[11]:

$$M_c = (\text{Mass of composite} - \text{Mass of aramid}) / \text{Mass of aramid}. \quad (1)$$

2.5 Absorption energy (E_{abs})

In the energy absorption tests, the air rifle was positioned 5 m away from the target, which consisted of a square sample attached to an MDF circular frame secured by a bench vise and aligned perpendicularly to the rifle. A ballistic chronograph was placed 10 cm away from the exit of the noise suppressor and another ballistic chronograph was placed 10 cm behind the composite to determine the residual speed of the projectile. The absorption energy was estimated using the equation

$$E_{\mathrm{abs}} = M_{\mathrm{p}}\,(v^2 - v_{\mathrm{r}}^{\,2})/2 \qquad (2)$$

in which M_{p} is the projectile mass, v is the impact speed and v_{r} is the residual speed[20]. Pasquali et al.[21] showed that energy is absorbed by a target of thin woven fabric due to six absorption/dissipation mechanisms: cone formation on back face of the target ; tensile failure of primary yarns ; deformation of secondary yarns ; shear plugging ; delamination onset and growth; and matrix cracking[22,23].

2.6 Depth of penetration (*DOP*)

In the *DOP* tests, the air rifle was positioned 5 m away from the target, which consisted of a square sample attached with adhesive tape to an MDF plate and aligned perpendicularly to the rifle[24–29]. A noise suppressor was used to increase the stability of the projectile at the exit of the air rifle by reducing the swirling caused by the exhaust. MDF plates were used as bulkheads because MDF is a homogeneous material, flat and dense, without the grain of solid wood. The ballistic chronograph was placed 10 cm away from the exit of the noise suppressor. When the distance between the air gun and the target is small, as in this case, the impact speed may be replaced by the muzzle speed[30].

2.7 Merit factor

Since, in the ballistic test, the samples are thin and homogeneous, projectile deceleration a can be assumed to be constant. Applying Newton's second law

$$a = -\,F/M_{\mathrm{p}} \qquad (3)$$

where F is the force on the projectile, the Torricelli equation may be written in the form

$$v2 - v_{\mathrm{r}}2 = 2\,(F/M_{\mathrm{p}})\,d \qquad (4)$$

in which d is the distance traveled by the projectile. Replacing Eq. 2 in Eq. 4 and dividing by the relative mass M_c, *we have*

$$E_{\mathrm{abs}}/(M_{\mathrm{c}}\,d) = F/M_{\mathrm{c}} \qquad (5)$$

A merit factor *MF* was defined as the ratio shown in Eq. 5 with $DOP = d$:

$$MF = E_{\mathrm{abs}}/\,M_{\mathrm{c}}\,DOP \qquad (6)$$

3. Results and discussion

3.1 X-ray diffraction

Figure 1 shows the X-ray diffraction pattern of the nanoparticles. The diffractogram showed 100% hematite, with 20 nm crystallite size and a GOF (Goodness of Fit) of 1.29.

Figure 1 - X-ray diffractogram of the nanoparticles.

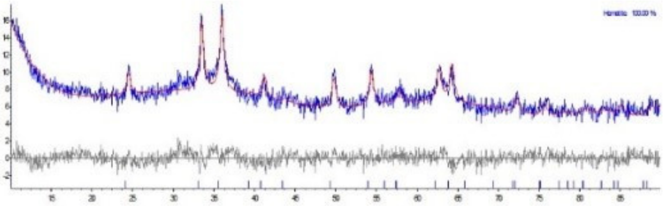

3.2 Ballistic tests

The ballistic tests consisted of measuring the energy absorbed by the composite and the depth of penetration (*DOP*) of a projectile on a medium density fiberboard (MDF) bulkhead.

All shots completely penetrated the sample. One shot was made in each experiment, and five experiments were performed for each composition.

Table 1 shows the composite relative mass (M_c), the absorption energy (E_{abs}), the depth of penetration (*DOP*) and the merit factor (*MF*) for all compositions. The energy absorbed is maximum for the samples with 7% hematite, while the *DOP* is minimum for samples with 9% hematite. This is attributed to the fact that the use of a bulkhead changes the mechanical behavior of the aramid fabric, favoring the breaking of primary fibers, which becomes an important energy absorption mechanism.

Table 1 - Average results of the ballistic tests.

COMPOSITE	M_c	E_{abs} (J)	DOP (mm)	MF (10-2) (J/mm)
A00	0.58 ± 0.07	5.70 ± 0.75	29.85 ± 0.35	32.72 ± 2.26
A03	0.62 ± 0.07	6.66 ± 0.91	27.75 ± 0.39	38.71 ± 3.00
A05	0.64 ± 0.06	6.69 ± 0.40	33.00 ± 0.43	31.68 ± 1.40
A07	0.57 ± 0.07	7.74 ± 0.58	28.58 ± 0.55	47.51 ± 2.78
A09	0.56 ± 0.06	6.01 ± 0.76	26.70 ± 0.40	40.20 ± 2.71
A11	0.53 ± 0.07	5.21 ± 0.37	29.92 ± 0.27	32.85 ± 1.67
A13	0.61 ± 0.06	6.51 ± 0.66	33.93 ± 0.55	31.45 ± 1.87
A15	0.58 ± 0.06	5.51 ± 0.54	27.97 ± 0.57	33.96 ± 2.12
A17	0.68 ± 0.09	6.14 ± 0.55	31.52 ± 0.50	28.65 ± 1.78

Figure 2 shows the dependence of the merit factor on hematite concentration. *MF* values were calculated using Eq. 2 with the values of $E_{abs,}$ *DOP* and M_c given in Table 1. The sample with the highest MF value was the one with 7% hematite (A07).

Figure 2 - Dependence of the merit factor on hematite concentration.

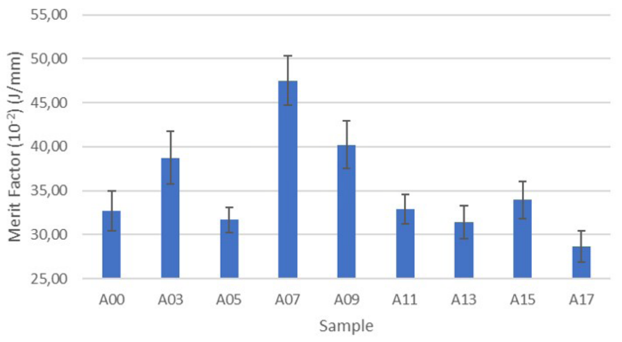

Figure 3 shows a sample with 7% hematite after the energy absorption test. One can see deformed primary and secondary yarns due to extended strain throughout the sample, suggesting a moderate pullout force.

Figure 3 - Sample with 7% hematite after the energy absorption test.

3.5 SEM images of an A07 sample

Figure 4 shows SEM images of a sample with 7% hematite (A07) before and after the ballistic test. Before the ballistic test (a), there is an excess of load that does not impregnate the aramid yarns and thus does not contribute significantly to ballistic resistance; and after the ballistic test (b), there is almost no excess of load, except in the bottom right of the image, where one can see clusters probably due to the impact[26]. The impact regions, which are not shown, are in the direction of the upper left corner of the images.

Figure 4 - SEM image of samples with 7% hematite (a) before and (b) after the impact.

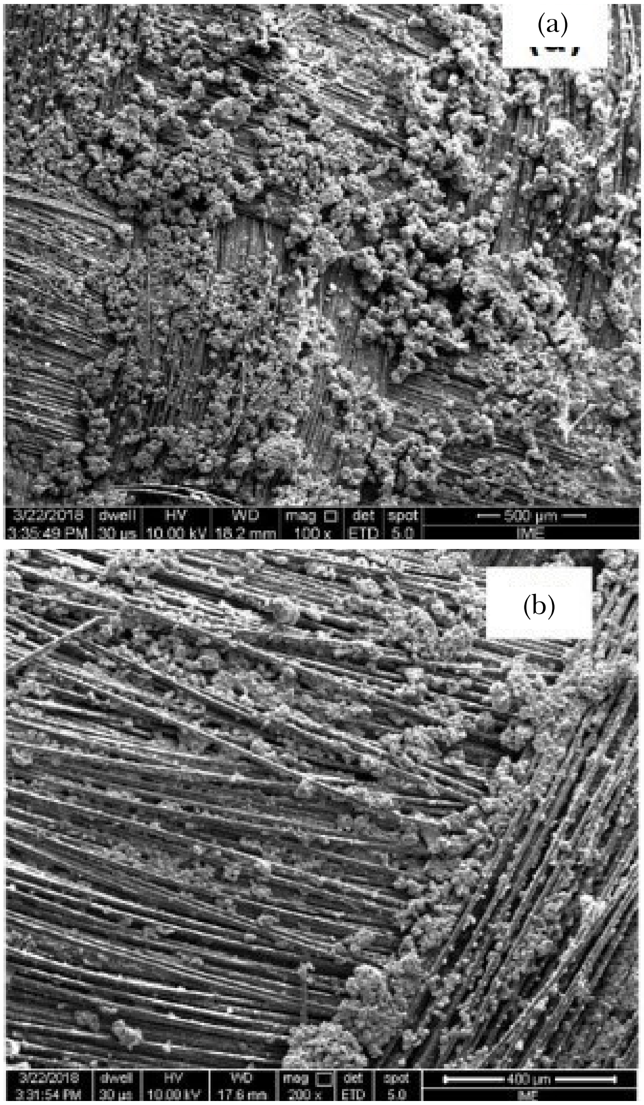

3.4 Reflectivity/absorption measurements

As shown in Figure 5, the dielectric loss ε”/ε’ is maximum and the reflectivity loss is minimum for a concentration of 3% hematite. According to Huo et al.[31], this is due to the fact that for hematite concentrations larger than 3%, the skin depth becomes very small due to increasing conductivity and most of the electromagnetic wave is reflected. As shown in Figure 6, the magnetic loss μ”/μ’ is maximum for 11 wt% hematite in the 8.2 to 11.6 GHz frequency range, but this effect is not enough to compensate the reflection loss caused by increasing conductivity, shown in Figure 5 (a). That is why, according to Figure 5 (b), it does not display the best performance in terms of reflectivity.

Figure 5 - (a) Dielectric and (b) reflectivity loss for pure aramid and aramid impregnated with an STF with 3%, 7%, 11% and 17% hematite.

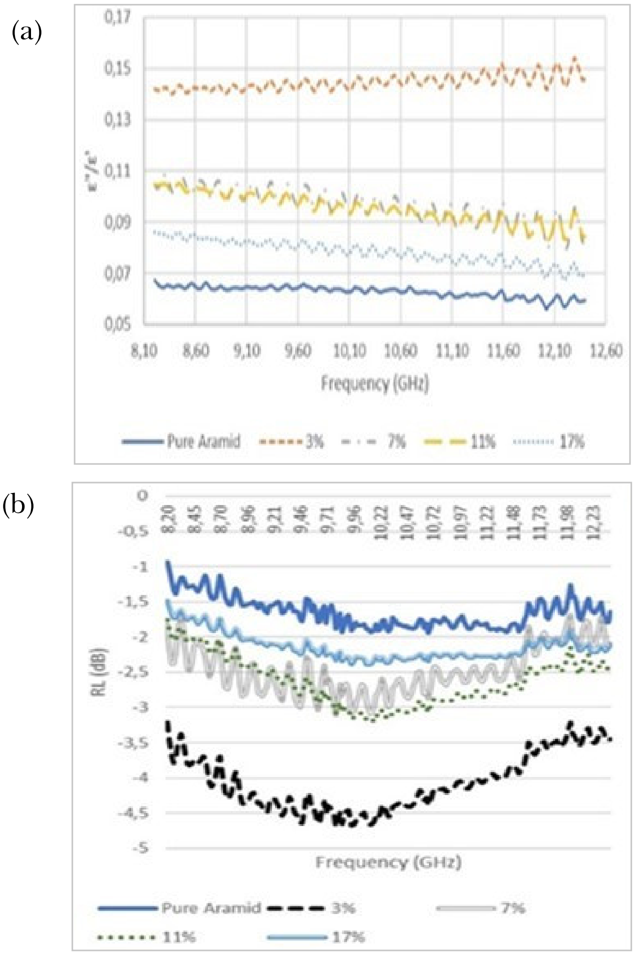

Figure 6 - Magnetic loss for pure aramid and aramid impregnated with an SFT with 3%, 7%, 11% and 17% hematite.

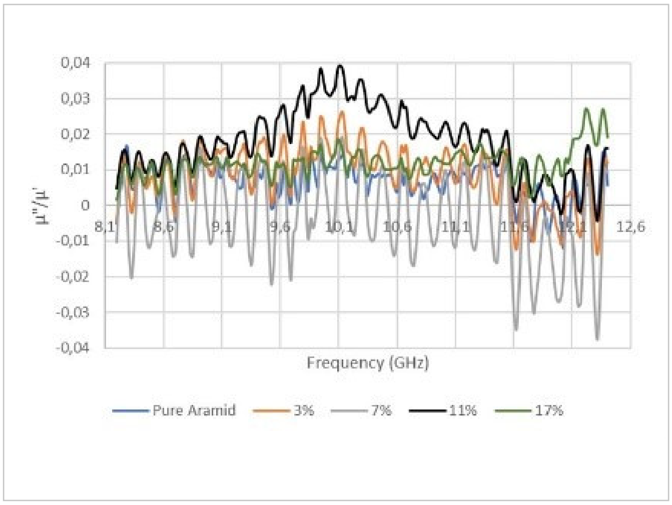

4. Conclusions

the composites with 7% hematite had the best ballistic behavior, while the composites with 3 wt% and 11% hematite had the best microwave absorption properties in terms of dielectric and magnetic loss, respectively. A reasonable compromise between ballistic resistance and microwave absorption seems to be using aramid fabric impregnated with 7 wt% hematite.

Acknowledgments

The authors thank CAPES (Coordination of Superior Level Staff Improvement) and CNPq (National Council for Scientific and Technological Development) for the financial support.

References

[1] CAVALLARO, P.V., Soft body armor: an overview of materials, manufacturing, testing, and ballistic impact dynamics, 1 August 2011, NUWC-NPT Technical Report 12,057

[2] EGRES, R. G. Jr., LEE, Y.S., KIRKWOOD, J. E., KIRKWOO, K. M., WETZEL E. D., WAGNER N.J. *Liquid armor: Protective fabrics utilizing shear thickening fluids*. In: IFAI INT. CONF. ON SAFETY AND PROTECTIVE FABRICS, 4. 2004, Pittsburgh. Conferência [...]. Pittsburgh, 2004.

[3] EGRES, R.G. Jr., HALBACH, C.J., DECKER, M.J., WETZEL E.D., WAGNER N.J., Stab performance of shear thickening fluid (STF)-fabric composites for body armor applications, Proceeding of SAMPE 2005: New Horizons for Materials and Processing Technologies. Long Beach, CA., 2005.

[4] BARNES, H. A., HUTTON, J.F., WALTERS, K., An introduction to rheology, Rheology Series 3, Elsevier, 1989.

[5] MARANZANO, B.J., WAGNER, N.J., The effects of interparticle interactions and particle size on reversible shear thickening: Hard-sphere colloidal dispersions, J. Chem. Phys., v. 114, p. 10514, 2001.

[6] BRADY, J.F., The rheological behavior of concentrated colloidal dispersions, J. Chem. Phys., v.99, p. 567, 1993.

[7] KRISHNAMURTHY, L., WAGNER, N.J., Shear thickening in polymer stabilized colloidal dispersions, J. Rheol., v. 49, p. 1347, 2005.

[8] MARANZANO, B.J., NORMAN, J.W., The effects of particles size on reversible shear thickening of concentrated colloidal dispersions: Hard-sphere colloidal dispersions, J. Rheol., v. 45, p. 1205, 2001.

[9] GALINDO-ROSALES, F.J., RUBIO-HERNÁNDEZ, F.J., SEVILLA, A., An apparent viscosity function for shear thickening fluids, J. Non-Newtonian Fluid Mech., v. 166, p. 321, 2011.

[10] SUN, L. -L., XIONG, D. -S., XU, C.-Y., Application of shear thickening fluid in ultra high molecular weight polyethylene fabric, J. Appl. Polym. Sci, v. 129, p. 1922, 2013.

[11] MAJUMDAR, A., BUTOLA, B. S., SRIVASTAVA, A., Development of soft composite materials with improved impact resistance using Kevlar fabric and nano silica based shear thickening, Mater. Des., v. 54, p. 295, 2014.

[12] TEBER, A., UNVER, I., KAVAS, H., AKTAS, B., BANSAL, R., Knitted radar absorbing materials (RAM) based on nickel-cobalt magnetic materials, J. Mag. Mag. Mat, v. 406, p. 228, 2016.

[13] WU, Q.-M., RUAN, J.-M., HUANG, B.-Y., ZHOU, Z.C., ZOU J.-P., Rheological behavior of fumed silica suspension in polyethylene glycol, J. Cent. South Univ. Technol., v. 13, p. 1, 2006.

[14] GÜRGEN, S., LI, W., KUSHAN, M.C., The rheology of shear thickening fluids with various ceramic particle additives, Mater. Des., v. 104, p. 312,2016.

[15] DECKER, M.J., HALBACH, C.J., NAM, C.H., WAGNER, N.J., WETZEL, E.D., Stab resistance of shear thickening fluid (STF)-treated fabrics, Comp. Sci. Tech., v. 67, p. 565, 2007.

[16] EGRES, R.G., DECKER, M.J., HALBACH, C.J., LEE, Y.S., KIRKWOOD, J.E., KIRKWOOD, K.M., WAGNER, N.J. Stab resistance of shear thickening fluid(STF) Kevlar composites for body armor applications, Proceeding of the 24th Army Science Conference, Orlando, FL, 2004.
[17] DING, J., TRACEY, P.J., LI, W., PENG, G., WHITTEN, P.G. Review on shear thickening fluids and applications, Textiles and Light Industrial Science and Technology, v. 2, p. 161, 2013.
[18] DE BIASI, R.S., FIGUEIREDO, A.B.S., FERNANDES, A.A.R., LARICA, C., Synthesis of cobalto ferrite nanoparticles using combustion waves, Solid State Commun., v. 144, p. 15, 2007.
[19] CAO, Z., QIN, M., JIA, B., GU, Y., CHEN, P., VOLINSKY, A.A., QU, X., One pot solution combustion synthesis of highly mesoporous hematite for photocatalysis, Ceram. Int., v. 41, p. 2806, 2015.
[20] LEE, Y.S., WETZEL, E.D., WAGNER, N.J., The ballistic impact characteristics of Kevlar woven fabrics impregnated with a colloidal shear thickening fluid, J. Mater. Sci., v. 38, p. 2825, 2003.
[21] PASQUALI, M., TERRA, C., GAUDENZI, P., Analytical modelling of high-velocity impacts on thin woven fabric composite targets, Compos. Struct., v. 131, p. 951, 2015.
[22] NAIK, N.K., SHRIRAO, P., Composite structures under ballistic impact, Compos. Struct., vol. 66, p. 579, 2004.
[23] NAIK, N.K., SHRIRAO, P., REDDY, B.C.K., Ballistic impact behaviour of woven fabric composites: Formulation, Int. J. Impact Eng., vol. 32, p. 1521, 2006.
[24] ALMUSALLAM, T.H., SIDDIQUI, N.A., IQBAL, R.A., ABBAS, H., Response of hybrid-fiber reinforced concrete slabs to hard projectile impact, Int. J. Impact Eng., v. 58, p. 17, 2013.
[25] WANG, J., CALLINAN, R., Residual strengths of composite structures subjected to ballistic impact, Compos. Struct., v. 117, p. 423, 2014.
[26] JORDAN, J.B., NAITO, C.J., Calculating fragment impact velocity from penetration data, Int. J. Impact Eng., v. 37, p. 530, 2010.
[27] BACKMAN, M.E., GOLDSMITH, W., The mechanics of penetration of projectiles into targets, Int. J. Eng. Sci., v. 16, p. 1, 1978.
[28] CARLUCCI, D.E.; JACOBSON, S.S. Ballistics: theory and design of guns and ammunition. Boca Raton [Florida]: CRC, 2008. 496 p. ISBN 1420066180.
[29] ANDERSON JR., C.E., Analytical models for penetration mechanics: A Review, Int. J. Impact Eng., v. 108, p. 3, 2017.
[30] VILLANUEVA, G.R.; CANTWELL, W.J. The high velocity impact response of composite and FML-reinforced sandwich structures, Comp. Sci. Tec., v. 64, p. 35-54, 2004.
[31] HUO J., WANG L., YU H., Polymeric nanocomposites for electromagnetic wave absorption, J. Mater. Sci., v. 44, p. 3917, 2009.

VOL.40 Nº2 2023
https://doi.org/10.22491/rmct.v40i2.11341.en

Influence of surface treatment on the primary stability of osseointegrated dental implants quantified with a strain gauge

Larissa Ramos Xavier Coutinho Nascimento, larissa.nascimento@ime.eb.br, Orcid 0000-0001-6533-5598
Carlos Nelson Elias, elias@ime.eb.br, Orcid 0000-0002-7560-6926
Guilherme Monteiro Torelly, gtorelly@gmail.com, Orcid 0000-0003-3019-2069

ABSTRACT: There are several hypotheses to explain the failures of osseointegrated titanium dental implants. Some possible explanations are the alterations in the mechanical properties of the maxillary bones, the surgical technique employed with excessive torques, the inadequate shape of the implants, and the deficient treatment of the surface of the implants. This work aims to measure the strain in the bone, quantify the insertion torque, and analyze the influence of surface treatment on the primary stability of dental implants. Extensometry tests were performed using strain gauges, and the insertion torque of the implants in synthetic polyurethane bone with a density of 30 PCF (0.48 g/cm³) was determined. The tests quantified the deformations in the synthetic bone and the maximum insertion torques of implants with the surface treated with double acid etching and without treatment (machined). The results showed that implants without surface treatment induce greater bone deformation, require lower insertion torque, have lower primary stability, and, in some essays, induce microcracks formation in the bone during insertion. Implants with an acid-treated surface perform better.

KEYWORDS: Dental Implant, Surface Treatment, Primary Stability.

RESUMO: São propostas várias hipóteses para explicar as falhas dos implantes dentários de titânio osseointegráveis. Entre as possíveis explicações destacam-se as alterações das propriedades mecânicas dos ossos maxilares, a técnica cirúrgica empregada com uso de torques excessivos, a forma inadequada dos implantes e o tratamento deficiente da superfície dos implantes. Os objetivos deste trabalho são medir a deformação no osso, quantificar o torque de inserção e analisar a influência do tratamento da superfície na estabilidade primária dos implantes dentários. Foram realizados ensaios de extensometria com o uso de strain gauges e determinado o torque de inserção dos implantes em osso sintético de poliuretano com densidade 30 PCF (0,48 g/cm³). Nos ensaios foram quantificadas as deformações no osso sintético e os torques máximo de inserção de implantes com a superfície tratada com duplo ataque ácido e sem tratamento (usinado). Os resultados mostraram que os implantes sem tratamento de superfície induzem maior deformação no osso, necessitam de menor torque de inserção, possuem menor estabilidade primária e em alguns ensaios induziram a formação de microtrincas no osso durante a inserção. Os implantes com superfície tratada com ácido apresentam melhor desempenho.

PALAVRAS-CHAVE: *Implante dentário, Tratamento de superfície, Estabilidade primária.*

1. Introduction

Dental implants' primary (mechanical) stability is quantified during or immediately after installation. Available studies do not provide data on the limit of compressive tension, which is transmitted to the bone during the insertion of dental implants. During implant installation, primary stability can be measured by insertion torque, with Periotest, or by resonant frequency analysis (RFA). Of these methods, measuring insertion torque is the simplest and provides the most accurate data to estimate the primary stability of implants. Compared to other methods, it is possible to more easily qualify bone density and primary stability at surgery by measuring the insertion torque. The primary stability of implants is affected by several factors, including body shape, diameter, length, and thread profile [1,2,3].

The surgical technique, the amount and density of bone available, and the morphology of the implant surface influence the success or failure of implants [2,3].

Nowadays, paradigm shifts have emerged in terms of how the surface characteristics of biomaterials influence biological response. Both microroughness and wettability increase surface energy, improve cell contact, and improve the osseointegration of titanium implants. Synergistic effects of nanoscale topography features, wettability, and quality of the implant-bone interface are relevant to the success of implant systems.

Surface treatments influence the osseointegration process, wettability, roughness, and morphology. The roughness of the implants' surface changes the adhesion and fixation of the osteogenic cells. Roughness can be quantified by several parameters, in which Ra is the most used, representing the arithmetic mean value of the size of the peaks and valleys on the surface regarding an imaginary mean line calculated. Regarding the roughness size of the implants, it can be divided into three levels: macroroughness, microroughness, and nanoroughness. Macroroughness with an order of magnitude of a millimeter does not influence osseointegration but affects the distribution of forces to the bone and the implant's stability [4]. Ideally, the roughness (Ra) of the implant body required for bone formation is between 1.0 and 2.0 µm [5]. Roughness around 1.0 µm (Ra) in the subepithelial segment region enables the subepithelial connective tissue adhesion. The endobone region's implant surface should induce bone regeneration and remodeling, promote optimal load distribution, increase the contact area, and lead to maximum cell deposition [4].

The surface wettability interferes with cell behavior and is evaluated by the contact angle. The chemical composition and surface energy are essential for osteoblast adhesion, the first phase of interaction between cells and the biomaterial, guiding cell proliferation in contact with the implant. Different surface treatments are used to change the morphology, topography, roughness, chemical composition, energy level, and decrease the contact angle to increase osseointegration with the best mechanical and biological anchorage [3].

Implant surfaces determine primary interfacial reactions with blood, bone cells, epithelial, and connective tissue components, such as macromolecule adsorption, cell adhesion, proliferation, and differentiation [5].

During surgery, the cavity prepared in the bone for the insertion of dental implants is filled with blood due to the rupture of damaged blood vessels and vascular trauma to the bone. Fibrin clot formation is associated with most wound healing processes and is linked to initial osseointegration reactions. The blood clot is used as a framework for migrating mesenchymal stem cells and the secretion of fibrinolytic enzymes. This migration process to a temporary connective tissue framework is called osteoconduction, being the first phase of osseointegration. After osteoconduction, the "new bone" formation occurs, which is initiated by the differentiation of osteoblasts [5].

Implant surface treatments aim to reduce the loading time of the prosthesis after surgery; accelerate bone growth and maturation to allow immediate loading; increase primary stability; ensure successful application in bone with lower density and quantity; obtain bone growth directly on the implant surface; obtain the largest possible area of osseointegration; obtain bone-implant contact without the interposition of amorphous protein layers; attract osteoblastic, pre-osteoblastic and mesenchymal cells; attract specific binding proteins to osteogenic cells (fibronectin); and obtain the highest possible concentration of cell-binding proteins [3].

Moderately rough oral implants are the most used, based on scientific evidence that such surfaces provide better bone response. A general trend in *in vivo* experiments is that the increase in the value of the As roughness parameter, which quantifies the arithmetic mean height of the peaks of the irregularities on the surface, increases the resistance to interfacial shear [6]. Halldin *et al.* (2015) [6] estimated the shear strength of the bone-implant interface for different surfaces. It was found that the surface with Sa of 1.51 µm increases the shear strength of the bone-implant interface by 45% relative to the surface with Sa of 0.91 µm after 12 weeks of healing [7].

Modifying the implant surface is recommended to increase the contact area of the implant with the bone, enable better shear strength of the bone-implant interface, and increase the friction coefficient [8]. It is essential to analyze the stress on the cortical bone and surface roughness in the region to avoid

VOL.40 Nº2 2023
https://doi.org/10.22491/rmct.v40i2.11341.en

bone loss around the dental implant. It was observed that as the stress on the cortical bone increases, bone loss increases.

Tabassum *et al*. (2009) [9] measured the roughness of the implant surface and observed, by topographic evaluation, that the machined surface has a significantly lower mean surface roughness (Ra = 0.45 μm) than the acid-conditioned surface (Ra = 1.47 μm).

This work shows the purpose of evaluating the primary stability of implants with treated surfaces and machined using a strain gauge. This device is used in extensometry testing to measure the strain suffered by an object. The deformation changes the length of the strain gauge, varying its electrical resistance. The strain gauge is connected to an analog-digital amplifier and to the software that quantifies the deformation suffered by the material [1].

2. Material and method

In this work, dental implants were inserted into specimens made of rigid polyurethane foam (NacionalOssos ®, Jaú, São Paulo) with a density of 30 PCF (0.48 g/cm^3) and a modulus of elasticity of 305.73 MPa, compatible with natural bone D2. Specimens in the form of a parallelepiped with a width of 50 mm and a height of 19 mm were used to insert the implants. The implants were 5 mm in diameter, and the specimen was 7 mm thick. The properties of the blocks are detailed in the ASTM F-1839-08 standard (Standard Specification for Rigid Polyurethane for use as a Standard Material for Testing Orthopaedic Devices and Instruments).

Strain gauges rectangular (Model PA-06-040 AB-120 - Excell Sensores, Taboão da Serra, São Paulo, Brazil) were glued to the upper edge of the specimens (Figure 1). The measuring axis was aligned perpendicular to the perforations. This configuration enabled the quantification of the deformations resulting from the compressive tension during implant insertion. In each polyurethane block, five implants were installed, with a spacing of 10 mm between them.

Figure 1 - Strain gauges glued to the specimen

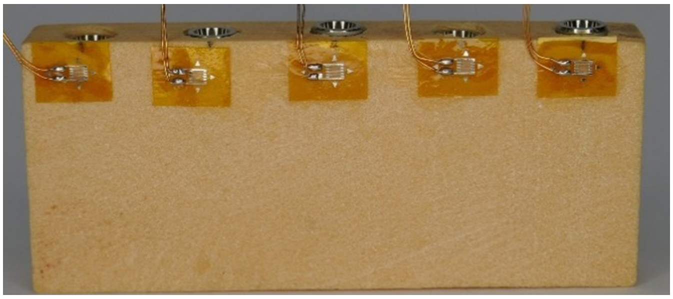

Two implant models (Figure 2) with two surface treatments were used. Easy-Grip implants with Porous surface® with double acid etching and the Master Screw machined implant from the company Conexão Sistema de Prótese (Arujá, São Paulo). The goal was to compare the influence of surface treatment on the insertion torque and synthetic bone strain.

Figures 2 - a) Easy Grip 5x15mm implant with the Porous surface; b) Easy Grip implant installed in the specimen; c) Machined implant (Master Screw)

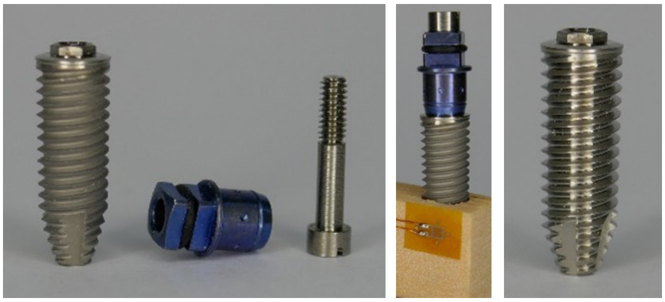

The implants with a diameter of 5.0 mm and a length of 15.0 mm were inserted into cavities prepared with the initial drilling performed with a pilot drill of 2.0 mm in diameter and rotation of 1,200 rpm. Next, 2.5, 3, 3.5, 4, and 4.5 mm diameter drills were used.

The block was attached to a TSS400 digital torque wrench (FUTEK, Irvine, CA, USA) with a capacity of 113 N.cm. The perforation for implant insertion was aligned with the rotation axis of the motor. The strain gauges were connected to the analog-digital-Spider 8 interface (HBM – Darmsladt- Germany). This system was configured for a data acquisition rate of 50 Hz, with a resolution of 16 bits. The implants were inserted by a stepper motor with a constant rotation of 25 rpm. Figure 3 shows the outline of the procedures.

Figure 3 - Experiment assembly scheme

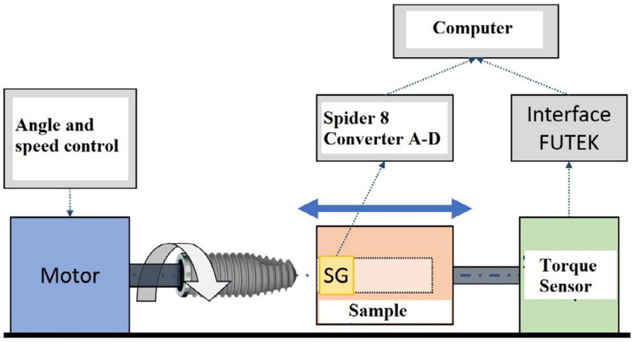

Results

Figures 4 and 5 and Table 1 show the results of the extensometry tests. It was possible to note that the surfaces of the implants with treated surfaces showed greater plastic deformation, induced less tension in the bone, and required higher insertion torque.

Figure 4 - Variation curves of plastic deformation and torque during the installation of implants without surface treatment (Master Screw)

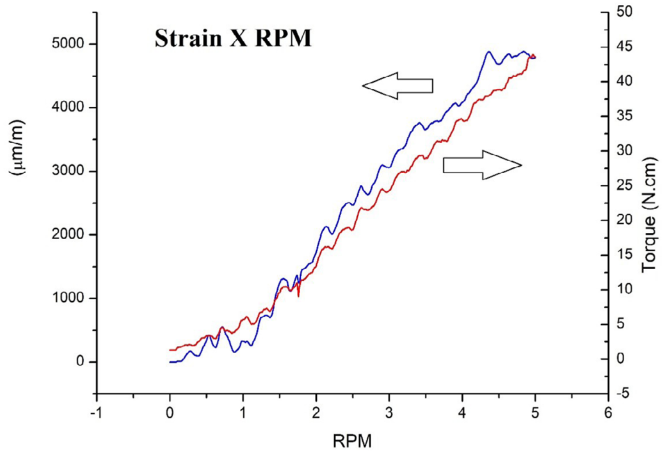

Figure 5 - Plastic Deformation and Torque Variation Curves During Implants Installation with Surface Treatment (Porous Surface)

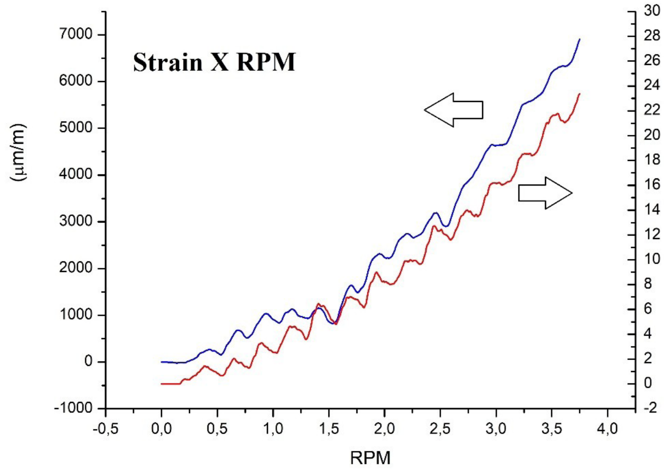

Table 1 - Deformation, insertion torque, and compressive tension during implant installation in synthetic bone

IMPLANTS	Mean Strain - ε (‰)	Mean Torque (N.cm)	σ (MPa)
Easy Grip	5.73 ± 2.86	53.9 ± 12.3	1.753
Master Screw	6.47 ± 2.48	43.6 ± 7.5	1.987

4. Discussion

The superficial roughness of the implants reduces bone healing time, provides greater mechanical locking, and increases primary stability [2].

The machined Master Screw implant has circular grooves from the manufacturing process. The surface of acid-etched implants (Porous surface) is more homogeneous than the machined surface. Surface treatment significantly alters the roughness parameters, which influence the interaction of the surface with proteins and cells, inducing osteogenesis, which can be evaluated by the implant removal torque [2].

Elias *et al*. (2012) [2] obtained an insertion torque of 45.86 N.cm for the installation of 3.75 x 13 mm Master Screw machined implants in polyurethane foam. The authors emphasize that machined implants surface have the lowest insertion torque compared to treated surfaces. The machined implant has lower surface roughness [1]. The insertion torque for the acid-conditioned implant is greater than that of the machined implant and less than that of the anodized implant. Implants with treated surfaces showed higher roughness, coefficient of friction, and insertion torque than machined implants. The surface roughness results and friction coefficients agree with the insertion torque results. Based on the results, the authors conclude that the anodized surface of the dental implant can be considered the best surface for osseointegration and primary stability [2].

Modifying the implants' surface is recommended to increase the bone-to-implant contact area, enabling greater resistance to shear forces and a higher coefficient of friction [9].

Santiago Junior *et al.* (2016) [10] observed that surface-treated implants induce greater tension and deformation in the cortical bone than machined implants. However, axial tension distribution is better in the peri-implant bone. The authors attribute this result to the increase in implants with treated surface areas.

Veis *et al.* (2017) [11] recommend using implants with a rough surface to improve primary stability. The authors add that the surface morphology of an implant influences the rate and extent of bone-implant fixation, which is expressed by the amount of bone-implant contact (BIC). In low bone density places, implants with an acid-treated surface are indicated.

Through finite element analysis, Bahrami et al. (2014) [12] analyzed the effect of surface treatments on tension distribution at the bone-implant interface in implants inserted in the mandible with immediate loading. The implant surfaces were divided based on the coefficient of friction: polished (CA = 0.4), plasma spray (CA = 1.0), sandblasted (CA = 0.68), implant with roughness in the polished coronal region (CA = 0.4), and treated with plasma spray (CA = 1). The increase in the roughness of the implant surfaces increases the maximum tension on the cortical bone, and the increase in the coefficient reduces the tension levels at the interface with the trabecular bone. Using a two-part surface treatment technique, with a low coefficient of friction at the interface with the cortical bone and a higher coefficient of friction at the interface with the trabecular bone, optimizes the tension levels at the bone-implant interface.

Figure 6 - Specimen showing cracks after machined implants insertion (Master Screw)

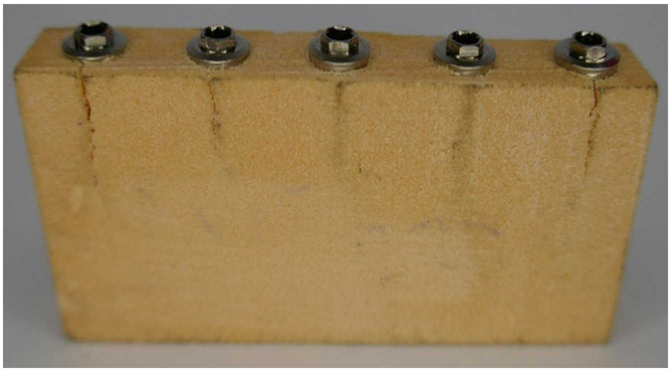

In this study, the machined implants induced greater bone deformation and were inserted with lower torque when compared to implants with an acid-etched surface (Porous). In addition, cracks were observed in the synthetic bone after the installation of machined implants.

The data in this study are different from those in the literature. One explanation for this contradiction is that, in the available studies, the tension on the bone is calculated by applying axial and oblique loading force to the implant abutment. However, the circumferential compression tension during implant insertion was determined. The tension is better distributed by increasing the surface area of the surface-treated implants, and the higher torque can be attributed to the coefficient of friction caused by the increase in roughness.

5. Conclusion

The results show that:

a. Machined implants induce greater deformation and compressive tension in the bone and require lower insertion torque. This result can be attributed to the smaller bone-implant contact area and the lower frictional force.

b. The machined implants induced the formation of cracks in the bone during insertion due to the lower distribution of tension in the synthetic bone.

c. Implants with a surface treated with double acid etching (Porous) induce less deformation and tension in the bone during insertion, minimizing the risks of excessive compression, bone necrosis, and microfractures, which would lead to implant loss.

Reference

[1] ATSUMI, M.; PARK, S.-H.; WANG, H.-L. Methods used to assess implant stability: current status. International Journal of Oral & Maxillofacial Implants, Lombard, v. 22, n. 5, 2007.

[2] ELIAS, C. N.; ROCHA, F. A.; NASCIMENTO, A. L.; COELHO, P. G. Influence of implant shape, surface morphology, surgical technique, and bone quality on the primary stability of dental implants. Journal of the Mechanical Behavior of Biomedical Materials, Amsterdam, v. 16, p. 169-180, 2012.

[3] [3] ELIAS, C. N.; OSHIDA, Y.; LIMA, J. H. C.; MULLER, C. A. Relationship between surface properties (roughness, wettability, and morphology) of titanium and dental implant removal torque. Journal of Mechanical Behavior of Biomedical Materials, Amsterdam, v. 23, n. 4, p. 234-242, 2008.

[4] ELIAS, C. N.; LIMA, J. H. C.; SANTOS, M. V. Modificações na superfície dos implantes dentários: da pesquisa básica à aplicação clínica. Implant News, [*s. l.*], p. 467-476, 2008.

[5] RUPP, F.; LIANG, L.; GEIS-GERSTORFER, J.; SCHEIDELER, L.; HÜTTIG, F. Surface characteristics of dental implants: A review. Dental Materials, Kidlington, v. 34, n. 1, p. 40-57, 2018.

[6] HALLDIN, A.; ANDER, M.; JACOBSSON, M.; HANSSON, S. Simulation of the mechanical interlocking capacity of a rough bone implant surface during healing. Biomedical Engineering Online, [*s. l.*], v. 14, p. 45, 2015.

[7] GOIATO, M. C.; SANTOS, D. M.; SANTIAGO, J. J.; MORENO, A.; PELLIZZER, E. P. Longevity of dental implants in type IV bone: a systematic review. International Journal of Oral and Maxillofacial Surgery, Copenhagen, v. 43, n. 9, p. 1108-1116, 2014.

[8] HUANG, H. L.; HSU, J. T.; FUH, L. J.; LIN, D. J.; CHEN, M. Y. Biomechanical simulation of various surface roughnesses and geometric designs on an immediately loaded dental implant. Computers in Biology and Medicine, New York, v. 40, n. 5, p. 525-532, 2010.

[9] TABASSUM, A.; MEIJER, G. J.; WOLKE, J. G.; JANSEN, J. A. Influence of the surgical technique and surface roughness on the primary stability of an implant in artificial bone with a density equivalent to maxillary bone: a laboratory study. Clinical Oral Implants Research, Copenhagen, v. 20, n. 4, p. 327-332, 2009.

[10] SANTIAGO JUNIOR, J. F. S.; VERRI, F. R.; FARIA ALMEIDA, D. A.; SOUZA BATISTA, V. E.; LEMOS, C. A. A.; PELLIZZER, E. P. Finite element analysis on influence of implant surface treatments, connection and bone types. Materials Science and Engineering: C, Amsterdam, v. 63, p. 292-300, 2016.

[11] VEIS, A. A.; PAPADIMITRIOU, S.; TRISI, P.; TSIRLIS, A. T.; PARISSIS, N. A.; KENEALY, J. N. Osseointegration of Osseotite and machined-surfaced titanium implants in membrane-covered critical sized defects: a histologic and histometric study in dogs. Clinical Oral Implants Research, Hoboken, v. 18, p. 153-160, 2007.

[12] BAHRAMI, B.; SHAHRBAF, S.; MIRZAKOUCHAKI, B.; GHALICHI, F.; ASHTIANI, M.; MARTIN, N. Effect of surface treatment on tension distribution in immediately loaded dental implants—A 3D finite element analysis. Dental Materials, Kidlington, v. 30, n. 4, p. e89-e97, 2014.

PÓS-GRADUAÇÃO NO IME

Bolsas: CAPES, CNPq e FAPERJ

Mestrado

- Sistemas e Computação
- Engenharia Mecânica

Mestrado e Doutorado

- Química
- Ciência dos Materiais
- Engenharia de Defesa
- Engenharia Nuclear
- Engenharia Elétrica
- Engenharia de Transportes

Matrículas: Semestral

Tel.: (21) 2546-7114 – Fax: (21) 2546-7089 – www.ime.eb.br – sd1@ime.eb.br